

Optical frequency division using high- Q integrated photonics

Thesis by
Qingxin Ji

In Partial Fulfillment of the Requirements for the
Degree of
Doctor of Philosophy

The logo for the California Institute of Technology (Caltech), consisting of the word "Caltech" in a bold, orange, sans-serif font.

CALIFORNIA INSTITUTE OF TECHNOLOGY
Pasadena, California

2025
Defended May 19th, 2025

© 2025

Qingxin Ji

ORCID: [0000-0002-6336-8350]

All rights reserved

ACKNOWLEDGEMENTS

This thesis was made possible through the guidance, insights, and resources generously shared by the academic community and collaborators. Sincere thanks to those who fostered critical thinking, provided essential facilities, and offered constructive feedback throughout this work. Gratitude is also extended to those whose unwavering support and encouragement sustained this endeavor.

ABSTRACT

Optical frequency division (OFD) coherently transfers the high spectral purity of optical transitions down to a microwave tone. This coherence transfer makes possible numerous modern technologies, including microwave synthesizing, optical atomic clocks, time and frequency transfer, optical frequency synthesizing, etc. In this thesis, I present advancements in using photonic-chip-based components to perform the OFD with high-performance. Along this pathway, chip-integrated, low-SWaP optical frequency combs are developed using coupled ring resonators. The key features include efficient dispersion tuning using the Moiré speedup effect and ultra-high Q factor up to 10^8 for an energy-efficient microcomb operation. To illustrate, recording low-noise microwave among those using integrated photonics are demonstrated. In moving towards a deliverable assembly, hybrid system packaging is demonstrated with characterized long-term stability. Ultrafast tuning control using integrated piezoelectric actuation simplifies the system architecture. In particular, an integrated, low-noise PDH locking system, and a full frequency-stabilized microcomb are demonstrated.

PUBLISHED CONTENT AND CONTRIBUTIONS

Ji, Qing-Xin, Wei Zhang, Anatoliy A. Savchenkov, Peng Liu, Shuman Sun, Warren Jin, Joel Guo, Jonathan Peters, Lue Wu, Avi Feshali, Mario Paniccia, Vladimir Ilchenko, et al. (2025). “Dispersive-wave-agile optical frequency division.” In: *Nature Photonics*. DOI: 10.1038/s41566-025-01667-4.

Q.-X. J. participated in the conception of the project, prepared the data, and participated in the writing of the manuscript.

Ji, Qing-Xin, Liu, Peng, Jin, Warren, Joel Guo, Lue Wu, Zhiquan Yuan, Jonathan Peters, Avi Feshali, Mario Paniccia, John E. Bowers, et al. (2024). “Multimodality integrated microresonators using the Moiré speedup effect.” In: *Science* 383.6687, pp. 1080–1083. DOI: 10.1126/science.adk9429.

Q.-X. J. participated in the conception of the project, performed the measurements, prepared the data, and participated in the writing of the manuscript (**contributed equally**).

Ji, Qing-Xin, Wei Zhang, Lue Wu, Warren Jin, Joel Guo, Avi Feshali, Mario Paniccia, John Bowers, Andrey Matsko, and Kerry Vahala (2024). “Coherent optical-to-microwave link using an integrated microcomb.” In: *IEEE Journal of Selected Topics in Quantum Electronics*. DOI: 10.1109/JSTQE.2024.3451301.

Q.-X. J. participated in the conception of the project, performed the measurements, prepared the data, and participated in the writing of the manuscript.

Kudelin, Igor, William Groman, Ji, Qing-Xin, Joel Guo, Megan L Kelleher, Dahyeon Lee, Takuma Nakamura, Charles A. McLemore, Pedram Shirmohammadi, Samin Hanifi, et al. (2024). “Photonic chip-based low-noise microwave oscillator.” In: *Nature* 627.8004, pp. 534–539. DOI: 10.1038/s41586-024-07058-z.

Q.-X. J. co-prepared the device, performed the measurements and participated in the writing of the manuscript.

Ji, Qing-Xin, Jin, Warren, Wu, Lue, Yu, Yan, Zhiquan Yuan, Wei Zhang, Maodong Gao, Bohan Li, Heming Wang, Chao Xiang, et al. (2023). “Engineered zero-dispersion microcombs using CMOS-ready photonics.” In: *Optica* 10.2, pp. 279–285. DOI: 10.1364/OPTICA.478710.

Q.-X. J. participated in the conception of the project, performed the measurements, prepared the data, and participated in the writing of the manuscript (**contributed equally**).

Yuan, Zhiquan, Maodong Gao, Yan Yu, Heming Wang, Warren Jin, Qing-Xin Ji, Avi Feshali, Mario Paniccia, John Bowers, and Kerry Vahala (2023). “Soliton pulse pairs at multiple colours in normal dispersion microresonators.” In: *Nature Photonics* 17.11, pp. 977–983. DOI: 10.1038/s41566-023-01257-2.

Q.-X. J. helped in the experiments.

Li, Jiang, Bao, Chengying, Ji, Qing-Xin, Heming Wang, Lue Wu, Stephanie Leifer, Charles Beichman, and Kerry Vahala (2022). “Efficiency of pulse pumped

soliton microcombs.” In: *Optica* 9.2, pp. 231–239. DOI: 10.1364/OPTICA.443060.

Q.-X. J. developed the theory and wrote the manuscript (**contributed equally**).

CONTENTS

Acknowledgements	iii
Abstract	iv
Published Content and Contributions	v
Contents	vi
List of Figures	ix
List of Tables	xxvii
Chapter I: Introduction: High- Q optical microresonators and their low-noise applications	1
1.1 Ultra-high- Q optical microresonator	1
1.2 CMOS-ready, ultra-low-loss Si_3N_4 platform	5
1.3 Applications of high- Q optical microresonators	6
1.4 Organization of the thesis	10
Chapter II: Photonic chip-based low-noise optical frequency division	16
2.1 Two-point optical frequency division	16
2.2 Miniaturized, low-noise optical references	18
2.3 Engineering of the microcomb for 2P-OFD	21
2.4 Dark pulse microcombs in two-coupled-ring resonator	25
2.5 Bright soliton microcomb with agile dispersive waves	27
2.6 Conclusion and summary	29
Chapter III: Dispersion engineering using coupled ring resonators	37
3.1 Theoretical dispersion of two-coupled-ring resonator	37
3.2 Device design and characterization	42
3.3 Integrated near-zero-GVD microcomb operation	44
3.4 Dispersion and SIL microcomb spectra	48
3.5 Imaging of mode-locked microcomb states	49
3.6 Discussion and summary	50
Chapter IV: Dispersion tuning of the coupled-ring resonator and multi-modality operation	57
4.1 Theory of Moiré-enhanced dispersion tuning	57
4.2 Differential temperature tuning control	59
4.3 Multi-modality operation	60
4.4 C-band operation of the same coupled ring device	67
4.5 Noise performance	67
4.6 Conclusion	68
Chapter V: Dispersion-agile three-coupled-ring resonator	72
5.1 Theory of dispersion tuning in the three-coupled-ring resonator	72
5.2 Dispersion centering and flattening	74
5.3 Dispersive wave emission and tuning	75
5.4 Microcomb-pumped mid-infrared light generation	76

Chapter VI: Avenues of system integration	80
6.1 Vision of full system integration in early 2023	80
6.2 Hybrid system packaging and Allan deviation results	82
6.3 Monolithic piezoelectric control: preliminary results	84
6.4 Conclusion of the thesis	94
Chapter A: Theory of Kerr microcombs	99
A.1 Introduction: The Lugiato-Lefever equation	99
A.2 Solving the LLE with the Split-Step Fourier Method	101
A.3 Excitation diagram analysis of the LLE	106
A.4 Lagrangian formula of pulse pumped soliton	111
Appendix B: Additional experimental results	120
B.1 Setup of the self-injection locked microcomb	120
B.2 Observation of interband multicolor solitons	123
B.3 Observation of broadband, self-injection locked noisy microcombs near zero-GVD	126
Standards and measurements of frequency stability	
B.4 Microwave phase noise	130
B.5 Laser short-term stability	131
B.6 Allan deviation	133

LIST OF FIGURES

<i>Number</i>	<i>Page</i>
1.1 Summary of microresonator platforms. Inset: Schematic showing optical loss channels for high- Q integrated optical microresonators. The intrinsic loss rate is characterized by the intrinsic Q factor (Q_0). Bus waveguide coupling also introduces loss that is characterized by the external coupling Q factor (Q_{ex}). Main panel: The references are: Silica micro-sphere (Braginsky, Gorodetsky, and V. S. Ilchenko, 1989; Vernooy et al., 1998); CaF_2 (Savchenkov et al., 2007); Silica wedge (Lee et al., 2012; L. Wu et al., 2020); Silica rod (Del’Haye, Diddams, and Papp, 2013; Yao et al., 2022); Silica ridge (2018) (K. Y. Yang et al., 2018); AlGaAs (2020) (Pu et al., 2016; Xie et al., 2020); High confinement Si_3N_4 (Xingchen Ji et al., 2017; Pfeiffer et al., 2018; J. Liu, Huang, et al., 2021); Low-confinement Si_3N_4 (Spencer et al., 2014; Puckett et al., 2021; W. Jin et al., 2021; Kaikai Liu et al., 2022); thin-film lithium tantalate (Chengli Wang et al., 2024); thin-film lithium niobate (Cheng Wang et al., 2019); AlN (Pernice, C. Xiong, and Tang, 2012; X. Liu et al., 2017; Kewei Liu et al., 2022); Tantala (Jung et al., 2021).	2
1.2 The CMOS-ready, ultra-low-loss Si_3N_4 platform. a, Photograph showing a fully fabricated, 8-inch (200 mm) wafer with ultra-low-loss Si_3N_4 circuit. b, Schematic of cross-section of the structure. Panels a-b are reproduced from (W. Jin et al., 2021). c, Photograph of a two-coupled-ring resonator device. d, Simulated TE mode of the resonator with Q factor measurement (two identical waveguide couplers are present). The ring resonator is with 16 GHz FSR and 20 μm waveguide width. e, Simulated TM mode of the resonator with Q factor measurement (credit to Jin-Yu Liu at Caltech). f, Group velocity dispersion (GVD) parameter D_2 of the ultra-low-loss Si_3N_4 platform. Strong GVD is present. Upper panel: from left to right, the waveguide width is 2.8 μm , 20 μm and 2.8 μm , respectively. Lower panel: the waveguide width is 20 μm (data credit to Jin-Yu Liu at Caltech).	5

2.1	Scheme of two-point optical frequency division, with selected publications during my PhD. Microcomb: A dark pulse microcomb (Q.-X. Ji, W. Jin, et al., 2023; Q.-X. Ji, P. Liu, et al., 2024) and a bright soliton microcomb with agile dispersive wave (Q.-X. Ji, W. Zhang, Savchenkov, et al., 2025). Reference cavity: A compact Fabry–Pérot cavity in high-vacuum (Q.-X. Ji, W. Zhang, L. Wu, et al., 2024) and a vacuum-free bulk Fabry–Pérot cavity (W. Zhang et al., 2024). System actuation and integration: a hybrid-packaged microcomb with a III-V laser pump (Q.-X. Ji, W. Zhang, Savchenkov, et al., 2025), and an integrated microcomb with piezoelectric tuner.	17
2.2	PDH locking setup. a , Experimental setup of the PDH locking subsystem for the two point optical frequency division system. ISO: isolator. ILP: in-line polarizer. EOM: electro-optic modulator. BPF: bandpass filter. PBS: polarization beam splitter. b , Ideal PDH error signal in the absence of experimental noise. c , Illustration of a realistic PDH error signal with typical experimental noise. d , Zoomed in view of the PDH error signal near the locking point. The laser frequency fluctuation Δf is plotted against the corresponding voltage error signal ΔV . The local slope (dashed line) determines the frequency to voltage conversion.	19
2.3	Comparison of laser noise under different PDH locking configurations. a , Comparison of laser relative phase noise when PDH locked to two FP cavities with different cavity linewidth $\delta\nu_C$. b , Comparison of laser relative phase noise when PDH locked to the same FP cavity, but using different photo detectors to generate the PDH error signal.	20
2.4	2P-OFD locking setup. EDFA: erbium-doped fiber amplifier. PD: photo detector. LPF: low-pass filter. BPF: band-pass filter. AMP: amplifiers. LO: local oscillator.	24
2.5	DFB current tuning response bandwidth characterization. a , Optical spectrum of the dark pulse microcomb. b , Tuning response of the f_{rep} when the DFB current is tuned. DC tuning efficiency is 69 kHz/mA.	25

- 2.6 **Discipline of the SIL microcomb repetition rate to an external microwave reference.** **a**, Experimental setup for external disciplining of the SIL microcomb repetition rate. PZT: Piezo-electric transducer. PD: photo detector. Servo: laser servo. Inset: schematic view of laser detuning $\delta\omega$ stabilization via repetition rate discipline. Fluctuation in $\delta\omega$ leads to fluctuation in repetition rate $\delta\omega_{\text{rep}}$, which is measured and compared to a microwave reference to generate the error signal for feedback to the laser driving current. Frequency noise of the free-running DFB laser (gray) is reduced by SIL (blue) and then reduced further by repetition rate locking (red). **b**, Repetition rate phase noise and microwave spectra of the free-running SIL microcomb (blue) and the externally disciplined microcomb (red). Measured phase noise of the microwave reference is plotted in gray. 25
- 2.7 **Microcomb phase noise characterization.** Single side-band (SSB) phase noise scaled to 10 GHz of free-running 20 GHz microcomb (blue), locked 20 GHz microwave (red), and locked 20 GHz microwave after regenerative frequency division by 2 (green). 27
- 2.8 **2P-OFD Details.** **a**, Optical spectral of bright soliton microcomb showing tuning of the dispersive waves. 2P-OFD across 3 THz is possible. **b**, Experimental setup for bright bright soliton microcomb generation. A c.w. laser (Orbits lightwave) near 1565 nm is isolated (ISO), frequency-shifted by a quadrature phase shift key modulator (QPSK), and amplified by an Erbium-doped fiber amplifier (EDFA). The light is then bandpass filtered to reduce the amplified spontaneous emission noise and coupled to the resonator chip using a lensed fiber. The coupled on-chip power is ~ 150 mW. Most of the soliton power is routed to the 2P-OFD system (see text). A small portion is monitored by an optical spectrum analyzer. **c**, Phase noise spectra summary of the generated microwave signal in the 2P-OFD experiment. All noise levels are scaled to a 10 GHz carrier. 28

- 2.9 **Measured beatnotes f_1 and f_2 in Figure 2.1 with and without dispersive-wave enhancement.** **a**, Measured beatnote between the stabilized c.w. laser (ν_1) and comb line (ν_m), where f_1 is 507.4 MHz. An SNR of 65 dB is measured with resolution bandwidth of 100 kHz. **b**, Measured beatnote between the stabilized c.w. laser (ν_2) and the dispersive wave (ν_n). An SNR of 60 dB is measured with resolution bandwidth of 100 kHz. f_2 is 743.6 MHz for the case with dispersive wave, and $f_2 = 979.9$ MHz for the case without the dispersive wave. A 30 dB improvement in SNR is demonstrated with the dispersive wave. 29
- 2.10 **Phase noise spectrum measurement of optical and microwave tones confirming the coherent optical-to-microwave link.** (a), Gray line: measured SSB phase noise of the relative phase noise of the two lasers. The other lines are measured phase noise of the generated 20 GHz microwave tone using the 2P-OFD. From top to bottom, the division ratio ($n - m$) is 4, 8, 12, 33, 49, respectively. (b), Measured phase noise versus the division ratio at different offset frequencies. From top to bottom, the frequency offset (whose color corresponds to the vertical dashed lines in panel (b)) is 100 Hz, 300 Hz, 1 kHz, 2 kHz, 5 kHz and 10 kHz. The dashed line denotes the theoretical predictions from Equation 2.1. 30

- 2.11 **Phase noise comparison of microwave generations based on microcomb, scaled to 10 GHz.** **a**, Single-sideband phase noise spectrum measurement with carrier frequency near 20 GHz (red). The instrumental measurement floor is the gray shaded area. For comparison, the phase noise is scaled by $\mathcal{L}_{\phi,10\text{GHz}} = \mathcal{L}_{\phi,f_{\text{rep}}} - 20 \times \log_{10}(f_{\text{rep}}/10 \text{ GHz})$, and plotted in black. **b**, The platforms are categorized based on the integration capability of microcomb generator and the reference laser source, excluding the inter-connecting optical/electrical parts. Filled (blank) squares are based on the OFD (stand-alone microcomb) approach. (i) 22 GHz silica microcomb (Yi et al., 2015), (ii) 5 GHz Si₃N₄ microcomb (W. Jin et al., 2021), (iii) 10.8 GHz Si₃N₄ microcomb (J. Liu, Lucas, et al., 2020), (iv) 22 GHz microcomb (J. Li et al., 2012), (v) MgF₂ microcomb (Liang et al., 2015), (vi) 100 GHz Si₃N₄ microcomb (S. Sun et al., 2024), (vii) 22 GHz fibre-stabilised SiO₂ microcomb (Kwon et al., 2022), (viii) MgF₂ microcomb (Matsko et al., 2016), (ix) 14 GHz MgF₂ microcomb pumped by an ultrastable laser (Weng et al., 2019), (x) 14 GHz microcomb-based transfer oscillator (Lucas et al., 2020). . . . 31
- 3.1 **Schematic of the two-ring coupled resonator.** Left panel: Top view of the coupled resonator with key points marked. Right panel: Schematic of the resonator with straightened waveguides (not to scale). Segment lengths and field amplitudes have been marked. . . . 38
- 3.2 **Eigenfrequency plots for the two-ring coupled resonator.** **a-c** Relative frequency (normalized to $D_{1,m}$), relative FSR (normalized to $\epsilon D_{1,m}$) and relative D_2 (normalized to $\epsilon^2 D_{1,m}$) plots for $g_{\text{co}}L_{\text{co}} = 0.3$. **d-f** Similar plots but with $g_{\text{co}}L_{\text{co}} = 1.0$. The horizontal axis is defined as $\phi_m = 2\pi\epsilon m$. Relative mode frequency, FSR and D_2 for individual rings before coupling have been superimposed (black dashed lines). The relative FSR is found by differentiating the relative frequency, and the relative D_2 is found by differentiating the relative FSR. . . . 39

- 3.3 **Illustration of mode hybridization in the coupling region.** **a**, Fitted optical resonance frequency dispersion of the coupled resonator (solid curves) and fitted mode frequency dispersion of the single rings (red and blue lines) plotted versus relative mode number μ . **b**, Cross-sectional view of simulated electric field amplitudes in the coupled region at mode numbers indicated in panel **a** by the black points. The right (left) waveguide belongs to ring A (B). At the crossing center (I, II, V and VI), two waveguides have the same field intensity and the opposite (same) phase for the anti-symmetric (symmetric) mode. When hybrid mode frequencies meet the single-ring resonances (III and IV), the electrical field at the coupled region is contributed by a single ring. 41
- 3.4 **Loss characterization of the 2CR resonator.** 44
- 3.5 **Self-injection-locked zero-dispersion microcomb using a coupled-ring resonator.** **a**, Photograph of the coupled ring resonators showing DFB pump laser. The two rings are nearly degenerate (FSR difference is ~ 100 MHz). **b**, Lower panel shows the coupled rings pumped by a DFB laser which is self-injection locked to a resonator mode. Periodic pulse trains (light red arrow) are generated. Upper panel shows the cross-sectional waveguide geometry of the ring coupling region ($2.8 \mu\text{m}$ waveguide width and $2.4 \mu\text{m}$ waveguide gap). **c**, Measured group velocity dispersion (GVD) parameter D_2 of the mode resonances versus wavelength. Zero dispersion is achieved near 1542 nm and 1559 nm. **d**, Optical spectra of the generated frequency comb when pumped near the two zero dispersion points. For the comb pumped at 1541 nm (gray), the span is 9.2 nm (as marked by the arrows). For the comb pumped at 1559 nm (orange), the span is 9.9 nm. The dashed line indicates the estimated on-chip line power of $1 \mu\text{W}$. **e,f**, Measured microwave frequency spectrum of the detected microcomb output when pumped at 1542nm (e) and 1560 nm (f). The resolution bandwidth is 10 kHz. 45

3.6 **Microcomb optical spectra and temporal waveforms measured at specific pumping wavelengths near the zero GVD wavelength.**
a, Solid lines give the integrated dispersion, defined as $D_{\text{int}} = \omega_{\mu} - \omega_0 - D_1\mu$ (right-hand side of Equation 3.16), measured at pumping wavelengths shown in the legend. The colored dashed lines denote the comb line frequencies (left-hand side of Equation 3.16) when pumped at the specified pumping wavelengths. The intersection of the mode resonances (solid line) and comb lines (dashed line) generates a dispersive wave. **b**, Measured GVD parameter D_2 versus wavelength near the zero GVD point. Arrows correspond to the pump wavelengths shown in panel a. Errorbar denotes standard deviation from the third-order polynomial fitting. **c-f**, Left panels: optical spectra of the microcomb when pumped near the zero-dispersion wavelength (specific pumping wavelength indicated and correspond to values in panel a). Simulated optical spectrum is plotted as the dashed black curve. The dispersive wave position from panel a is marked by arrows. Right panel: measured microcomb temporal waveform during one round trip for the pumping wavelength given in left panel. 46

3.7 **Dispersion and microcomb generation of the 2CR device with optimized ϵ .** **a**, The measured integrated dispersion is plotted versus mode number. **b**, Experimentally measured microcomb spectrum under laser SIL. 52

4.1 **Differential temperature tuning using integrated heaters.** **(A)**, Details of the heater routing. The electrodes (gray rectangles) are wire bonded to an external circuit board to apply the heating current. Heaters (red) are located at the arcs of the racetrack and are electrically connected with a wider electrical trace (yellow). The wider trace has less electrical resistance and thus reduces the heating effect at the coupling section of the two rings. This design improves the differential thermal tuning efficiency. All three parts (red, yellow and gray) are deposited with the same Pt layer thickness. **(B)**, Principle of integrated heater frequency response characterization. **(C)**, Heater frequency response characterization setup. **(D)**, Measured frequency response of the heater transfer function. The dashed line is a Lorentzian fitting where the 6 dB bandwidth is 2.67 ± 0.05 kHz. 59

- 4.2 **A hybridly integrated microresonator and optical pump can be operated as a Brillouin laser, bright microcomb, or dark pulse microcomb source with on-demand electrical control and at a user-defined wavelength across C-band.** (A), Illustration of the reconfigurable hybridly integrated device. Si_3N_4 coupled rings (CRs) are directly pumped by an integrated III-V laser. Dispersion of the CRs is tuned by differential tuning of the rings using integrated resistive heaters. The III-V laser and the heaters are wire-bonded to printed circuit boards for electrical control. (B), Photograph of the integrated device depicted in panel A. (C), Zoom-in image of the coupled racetrack ring resonator. Resistive heaters are deposited atop the chip and offset from the Si_3N_4 waveguide by $8\ \mu\text{m}$ to avoid metal-induced optical absorption. (D-F), Optical spectra for on-demand operation of the Brillouin laser (panel D), bright microcomb (panel E) and dark pulse microcomb (panel F), all operated at the same III-V laser pumping wavelength $\lambda_0=1548.4\ \text{nm}$ per the system layout in panel B. In each case, dispersion is reconfigured via simple electrical tuning. In panel E the black curve denotes the sech^2 envelope and gives an optical pulse width of 800 fs. **Left insets:** schematic drawings of Brillouin emission between symmetric and antisymmetric hybrid modes (panel D) and pulse shape temporal waveforms inside the coupled rings (panels E and F). **Right insets:** RF beatnote (panel D) between the pump laser and Brillouin laser (resolution bandwidth is 100 kHz). Repetition rate tone (panels E, F) confirming mode locking (resolution bandwidth is 10 kHz). 61

- 4.3 **Measurement of Moiré speedup of the dispersion spectrum.** **(A)**, Illustration of the Moiré pattern formed by mode frequencies in ring A and ring B resonators. A large shift Δf_0 of Moiré pattern is caused by a small uniform shift Δf_{diff} of the ring B frequencies. Brighter regions in the pattern correspond to degeneracy of the local ring modes and lead to strong modal hybridization. Here ring A is assumed stationary (stat.), while ring B is tuned and illustrated before and after the differential tuning. **(B)**, Each color shows the measured (bold) and fitted (fine solid line) dispersion spectra for the two frequency bands of the system. Mode number $m_0 = 0$ corresponds to 1550 nm. The red spectra result from differential heating. **(C)**, Dispersion tuning for non-differential heating (i.e., common mode tuning) by 10 K (blue and red). No dispersion change is observed and the curves have been intentionally offset by 2 GHz for comparison. **(D)**, Measurement of the Moiré speedup effect wherein dispersion tuning of the circled dots in panel (A) are measured versus differential heating. Solid lines give a linear fit with Vernier ratio $R = 0.2$ THz/GHz. The three colors correspond to different reference points when evaluating the dispersion tuning, as illustrated in panel (A): S band (light purple), C band (light blue) and L band (light red). Inset: calibration of mode resonant frequency shift versus chip temperature: $\delta f_m / \delta T_{\text{common}} = 1.561 \pm 0.003$ GHz/K (upper band) and 1.558 ± 0.001 GHz/K (lower band). 62

- 4.4 **Broadband operation of the Brillouin laser, bright soliton microcomb and dark pulse microcomb.** (A), Broadband tuning of the Brillouin phase matching condition across the optical C band and partial S, L bands. Frequency spacing between the upper and lower bands in Figure 2 is plotted versus relative mode number (upper scale: wavelength) for two different T_{diff} . Red and blue curves are data (bold curve) and model (fine curve). The orange region gives the accessible mode frequency spacing. The gray area denotes the approximate frequencies where Brillouin gain is possible. (B), Experimental demonstration of reconfigured Brillouin lasing across the optical C band. (C), Reconfiguration of group velocity dispersion (GVD) for bright soliton and dark pulse generation. The fitted GVD parameter D_{2c} at two different T_{diff} is plotted versus mode number (upper scale: wavelength). Red and blue curves are data fit (dots) and model (fine curve). The orange region gives the theoretically accessible D_{2c} values. The discontinuity of the red dots at large mode numbers is due to the insufficient bus-ring coupling at shorter wavelengths, making it challenging to capture and analyze these mode resonances. (D-E), Experimental demonstration of reconfigured bright soliton microcomb (D) and dark pulse microcomb (E) under DFB laser self-injection-locked operation at four different wavelengths. Mode locking is confirmed by the high signal-to-noise ratio photodetected repetition rate tone. 63
- 4.5 **Real time switching between a bright pulse microcomb and a dark pulse microcomb.** (A), Experimental setup. (B), Measured repetition rate when the microcomb is switched from a bright pulse microcomb to a dark pulse microcomb. 65
- 4.6 **Optical frequency noise spectrum of pump (self-injection-locked) and the Brillouin laser.** 68

- 5.1 **Dispersion and bright soliton microcomb with electrically tunable dispersive wave.** **a**, Measured dispersion spectrum showing the 3 dispersion bands of the 3CR device (blue dots). The theoretical fitting is plotted as the solid curves, and the inferred dispersion of the uncoupled rings are the shaded lines (red, blue and gray for ring A, B, and C, respectively). The relative mode number $m - m_0$ is plotted in the upper axis, where m_0 corresponds to the intersection of the uncoupled ring B and ring C dispersion curves. The corresponding wavelength is $\lambda_0 = 1568$ nm (lower axis). **b**, Isolated dispersion spectrum for the upper band in panel a. Dashed horizontal line gives location of the dispersive wave phase matching wavelengths. **c**, Optical spectral of bright soliton microcomb showing tuning of the dispersive waves. Inset: illustration of the dispersion changing when the heaters are differentially fine-tuned. The arrows indicate the change of the dispersion curves when ring A is heated. 73
- 5.2 **Dispersion tuning and dispersive wave tuning in the bright soliton microcomb using electrical heaters.** **a**, Upper panel: measured dispersion spectrum of the 3-coupled-ring (3CR) resonator with random heater tuning. Middle panel: measured dispersion spectrum of the 3CR after tuning λ_0 closer to the pump wavelength (1565 nm) by heating ring B. Lower panel: measured dispersion spectrum of the 3CR after the local GVD parameter is tuned by heating ring A. **b,c**, Measurement of dispersive wave tuning when ring A (B) is fine-tuned. The 1542 nm dispersive wave is plotted in blue, while the 1590 nm dispersive wave is plotted in red. The corresponding data points in Figure 5.1c and panel d are indicated by the arrows (matched by the colours). **d**, Measured optical spectra of the bright soliton microcomb with three different dispersive wave tunings. Inset: theoretical dispersion spectra when ring B is tuned. The arrow indicates the change of the dispersion curves when ring B is heated. 74

- 5.3 **Temporal characterization of the bright soliton microcomb.** **a**, Optical spectrum of the bright soliton microcomb. **b**, Autocorrelation trace showing repetitive pulses with a 50 ps period (20 GHz repetition rate). **c**, Autocorrelation data (red dots) with Lorentzian fitting (solid line). The full-width at half-maximum (FWHM) of the autocorrelation signal is 843 fs, corresponding to a single-pulse intensity FWHM of approximately 500 fs. 76
- 5.4 **Mid-infrared light generation results.** **a**, Experimental setup. EDFA: erbium-doped fiber amplifier. ND HNLF: normal-dispersion highly nonlinear fiber. AD HNLF: anomalous-dispersion highly nonlinear fiber. PPLN: periodically poled lithium niobate. (Materials courtesy of Pooja Sekhar, CU Boulder.) 77
- 6.1 **Schematic design of a photonic microwave oscillator on a single chip.** The integrated system employs the same key photonic elements used in this work. Two spiral-resonator SIL lasers are PDH-locked to the same micro FP cavity with two EOMs in series for each SIL laser—the first for fast phase correction and the second for PDH sidebands. The right side of the schematic shows the FP cavity interface, where the two SIL laser paths are fed through an interferometer with an embedded polarization splitting grating. This serves as a reflection cancellation circuit while also shaping the planar waveguide mode to match the FP mode (Cheng et al., 2023). The reflection from the FP cavity is then detected by the right-most detector. Inset: Photo of the miniature FP cavity, consisted of micro-fabricated mirrors (N. Jin et al., 2022), with overall volume of $\sim 1 \text{ cm}^3$ 81

- 6.2 Hybrid packaging of the dispersive-wave-tunable microcomb, and Allan deviation results.** **a**, Photograph of the hybridly packaged 3CR chip with III-V pump. **b**, Illustration of the packaging scheme. Output of the DFB laser is collected by a microlens, and passes through an anti-reflection coated silicon slab for feedback phase tuning (via electrical heating). The light is laterally focused by another microlens to be coupled into the Si₃N₄ waveguide. Heaters are deposited on the 3CR chip and wire-bonded, and dispersion is tuned to support bright soliton mode locking. The output beam of the Si₃N₄ waveguide is shaped by another pair of microlenses and collected by an optical fiber ferrule. **c**, Measured optical spectra from the hybrid-integrated microcomb module showing tuning of the dispersive wave. **d**, Allan deviation results. Fractional Allan deviation of 3.6×10^{-13} is measured at the averaging time of 250 ms. For averaging time > 1 s, a linear drift of 0.013 Hz/s is removed. 83
- 6.3 Tuning of Si₃N₄ circuits via AlN piezoelectric actuation.** **a**, Schematic cross section of the chip. Piezoelectric strain induced by an electric field changes the refractive index of optical waveguides, resulting in resonance frequency shifts. **b**, AlN actuator induced stress tensor σ_{xx} is plotted in color, and the arrows denote the stress-induced mechanical force. **c**, Amplitude and phase of frequency response of the piezoelectric actuator on a single ring. The measurement used the method similar to Figure 4.1. 85

- 6.4 **Detailed AlN piezoelectric tuner fabrication process.** **a**, Photograph of the fabricated 4-inch wafer. **b**, Illustration of the fabrication process. (i) The process starts with the foundry-based Si_3N_4 ultra-low-loss circuit on an 8-inch wafer, followed by chemical-mechanical polishing (CMP) to planarize the top silica cladding. After the wafer is cored to 4-inch wafers, alignment markers are then etched on the silica cladding using dry etch with Al hard masking. (ii) 100 nm of Mo (which later serves as the bottom electrode) and 1 μm of AlN are deposited at an external foundry (AMSystems). (iii) 100 nm of Al is deposited via e-beam evaporation and lift-off is performed to define the top electrode. (iv) The AlN layer is plasma etched using a combination of Cl_2 and Ar. (v) The AlN layer is plasma etched using a combination of Cl_2 and O_2 . (vi) Additional Al pads connected with the bottom Mo electrodes are fabricated with same process in (iii) to enable wire bonding (since the Mo electrode is usually not able to be ultrasonic wire-bonded). (vii) The wafer is baked at 250 °C for ~50 hours to mitigate the induced additional optical propagation loss during the lithography processes (Guo et al., 2024; Xinru Ji et al., 2024). 86
- 6.5 **Piezoelectric DC tuning and AC modulation of the self-injection locked laser.** **a**, Schematic of a III-V DFB laser self-injection locked (SIL) to a high- Q Si_3N_4 resonator with AlN piezoelectric tuner atop. A portion of incident laser light (red arrow) is back-scattered (orange arrow) inside the ring resonator to the laser. **b**, SIL operation stabilizes the laser to the Si_3N_4 ring resonance which is frequency tunable via piezoelectric tuning. Simultaneous AC piezoelectric modulation at f_m creates two frequency modulated sidebands. **c**, Cross section of the chip showing how near-DC piezoelectric tuning modifies the Si_3N_4 ring resonance via mechanical strain. **d**, AC piezoelectric modulation at f_m excites a high-overtone bulk acoustic resonance (HBAR) for optical phase modulation. **e**, Frequency tuning of the SIL laser achieves > 1 MHz response bandwidth. **f**, An HBAR resonance is observed near 5.6 MHz. 87

- 6.6 **PDH locking the SIL laser to an optical reference via integrated piezoelectric tuning and modulation.** **a**, Experimental setup. **b**, Photograph showing the SIL laser with AlN piezoelectric control. **c**, Tuning the frequency-modulated SIL laser across a the Fabry–Pérot cavity resonance (illustrated in upper panel) to observe the PDH signal (lower panel). **d**, Allan deviation results. Fractional frequency stability reaches 1.9×10^{-13} at an averaging time of 200 ms. A linear drift of 800 Hz/s has been removed (error bar denotes standard deviation). **e**, Phase noise characterization. 88
- 6.7 **Integrated separable tuning of microcomb offset and repetition rate.** **a**, Illustration of the two degrees of frequency control required for comb operation: offset frequency on left and repetition rate on right. **b**, Common mode and differential mode tuning control in a vernier-coupled-ring resonator. Illustration of integrated dispersion plotted versus relative mode number ($m - m_0$). The mode number m_0 corresponds to a degeneracy frequency of the rings. Left: common-mode tuning induces a vertical frequency shift of the dispersion curve by $\delta\nu_{\text{comm}}$ so that the optical resonance $\nu_0 \rightarrow \nu_0 + \delta\nu_{\text{comm}}$. Right: differential-mode tuning shifts the dispersion curve laterally causing the FSR to tune, but having no affect on ν_0 . This dispersion shift is magnified by the Vernier factor R , enhancing the rate of tuning of the FSR. Integrated dispersion is given by: $\nu_m - FSR_0(m - m_0) = \nu_0 + (D_{2c}/2\pi)(m - m_0)^2/2 + ..$ where ν_0 , FSR_0 , D_{2c} are mode frequency, FSR, and second-order dispersion (only the resonator coupling contribution) at mode m_0 . **d**, Photograph of the resonator with piezoelectric actuators and self-injection-locked DFB laser pump. 89

- 6.8 Differential and common mode piezoelectric tuning of the coupled ring resonator.** **a**, Circuit for generation of control signals from servo voltages δV_1 and δV_2 for common mode and differential mode tuning ν_0 and f_{rep} . **b**, Optical spectrum of the normal dispersion microcomb (blue). Two reference lasers are depicted at frequencies $\nu_{\text{ref},1}$ and $\nu_{\text{ref},2}$. **c**, Measured tuning response for ν_0 when δV_1 (red) and δV_2 (gray) are modulated. The tuning crosstalk is suppressed by > 40 dB. **d**, Measured tuning response for f_{rep} when δV_1 (gray) and δV_2 (blue) are modulated. The tuning crosstalk is suppressed by > 40 dB. 90
- 6.9 Microcomb frequency stabilization.** **a**, Illustration of stabilization of f_{rep} and ν_0 . Two lasers (frequencies: $\nu_{\text{ref},1}$ and $\nu_{\text{ref},2}$) are stabilized to two modes of the same Fabry–Pérot cavity (gray spectrum). Comb lines at ν_0 and ν_N are locked to these lasers by first generating photodetector beatnotes ($f_1 = \nu_{\text{ref},1} - \nu_0$, $f_2 = \nu_{\text{ref},2} - \nu_N$). ν_0 is then locked by locking f_1 to the local oscillator at $f_{\text{LO}2}$ by servo control of the common-mode tuning actuator. To lock ν_N , intermediate frequency $f_1 - f_2 = (\nu_{\text{ref},1} - \nu_{\text{ref},2}) - Nf_{\text{rep}}$ is produced and locked to $f_{\text{LO}1}$ by servo control of the differential actuator. This also stabilizes the comb repetition rate (f_{rep}) by 2-point optical frequency division of the laser spacing ($\nu_{\text{ref},1} - \nu_{\text{ref},2}$). **b**, The electrical spectrum (RBW 10 Hz) of the stabilized beat note between reference laser 1 and the comb ($f_1 = \nu_{\text{ref},1} - \nu_0$). **c**, The electrical spectrum (RBW 10 Hz) of the stabilized comb repetition rate f_{rep} . **d**, Phase noise spectra of the stabilized beat note between reference laser 1 and the comb when the microcomb is free-running (gray) and frequency-stabilized (red). **e**, Phase noise spectra of the f_{rep} when the microcomb is free-running (gray) and frequency-stabilized (blue). 93
- A.1 Excitation spectrum calculation of a single soliton ($h = 5$).** **a-c**, A stable soliton state ($\Delta = 25$). **d-f**, A ‘pre-breather’ state ($\Delta = 11$). **g-i**, A breather soliton state ($\Delta = 10$). 110

- A.2 **Pulse pumped microcavity soliton.** Pulse pumping of a microcavity soliton in the presence of the Raman effect. Main panel: illustration of soliton position relative to the pump pulse under different pump rates and detunings. Inset: A relatively broad pumping pulse (width τ_p) is coupled into a microcavity. A narrower soliton pulse (width τ_s) is generated and trapped by the pump field. 111
- A.3 **Representative locking term $K_L(t_0, \delta\omega)$.** **a**, Nonlinear locking term for $Q_{\text{ex}} = 34$ million. Detuning $\delta\omega/2\pi = 27$ MHz and $\delta\omega_{\text{max}}/2\pi = 59.8$ MHz. Area with positive K_L is shaded in red, while that with negative K_L is shaded with blue. Positive (negative) K_L pushes the soliton forward (backward) in the fast time frame. Phase chirp term (K_p) and amplitude slope term (K_a) contributions of K_L are plotted with green and red, respectively. **b**, K_L is plotted under conditions of stronger over-coupling. The coupling Q_{ex} factor is reduced to 11 million, $\delta\omega/2\pi = 27$ MHz, $\delta\omega_{\text{max}}/2\pi = 28.4$ MHz, while other parameters are the same as in panel a. 116
- A.4 **Drift speed of the soliton based on the Lagrangian analysis and numerically simulated steady states.** **a**, The pump offset rate is set as $\delta\omega_{\text{rep}} = -50$ kHz. **b**, The pump offset rate is set as $\delta\omega_{\text{rep}} = -50$ kHz. Zero drift speed positions are marked by solid red lines. It is noted that branch II and III are stable trapping positions, while branch I is unstable. The intersections of branch I and II are marked by a circle. Gray shading indicates that no soliton solution exists. The simulated steady-state trapping positions are plotted with blue dots. Tuning direction of the pump laser frequency in the simulation is illustrated with blue arrows. 116
- B.1 **Packaging of DFB lasers for self-injection locking.** **a**, Schematic of the DFB laser mounted on a submount with an integrated thermistor. **b**, Photograph of the laser on the submount, attached to a thermoelectric cooler (TEC) and wire-bonded to a butterfly case for electrical interfacing. **c**, Final package: butterfly case mounted to an aluminum heat sink. **d**, Close-up showing the wire bonding within the butterfly case. **e**, Pin diagram of the butterfly package. Materials credit to Leo Wu. 121
- B.2 **Assembly of the Si_3N_4 chip with temperature control.** 122

- B.3 Generation of the interband multicolor solitons.** **a**, Conceptual illustration of interband multicolor solitons generation. **b**, Photograph of the three-coupled-ring device used in this study. **c**, RF spectrum of detected pulse train (10 Hz resolution bandwidth). **d,e**, Measured autocorrelation traces (blue) and their Lorentzian fitting curves (red) for the primary and secondary solitons. **f**, Optical spectrum of interband multicolor solitons. The lower panel is a zoom-in view of the gray shaded area in the upper graph. **g**, Corresponding cavity dispersion spectrum. 123
- B.4 Optical spectrum of a broadband, noisy microcomb under laser self-injection locking.** The microcomb state is generated from the same 2CR device in Chapter 3. The optical spectrum spans >2.5 THz, with a noisy RF tone near 20 GHz. 126
- B.5 Microwave phase noise measurement techniques.** 130
- B.6 Laser noise measurement setups.** 131
- B.7 Optical frequency noise of the pump laser (comb offset frequency).** Single sideband optical frequency noise of the comb pump frequency. Grey curve gives the free-running (non SIL) measurement, blue curve is for self injection locked (SIL) operation, and the red curve is for repetition rate discipline using an external microwave reference. The thermorefractive noise floor is denoted by the dashed gray line. 133
- B.8 Allan deviation measurement.** **a**, Experimental setup. **b**, Summary of the Allan deviation measurement results. Data are presented as mean values, and the error bar denotes standard deviation where the sample number is 6096, 6096 and 1200 for the blue, orange and red traces, respectively. 134

LIST OF TABLES

<i>Number</i>		<i>Page</i>
1.1	Comparison between different miniaturized reference cavities.	8
1.2	Comparison between different laser stabilization techniques.	8
A.1	Conversion between different forms of LLEs.	100
A.2	Summary of simulation parameters, for self-injection locked, near-zero GVD microcomb.	105

Chapter 1

INTRODUCTION: HIGH- Q OPTICAL MICRORESONATORS AND THEIR LOW-NOISE APPLICATIONS

The true nobility is in being
superior to your previous self.

Ernest Hemingway

1.1 Ultra-high- Q optical microresonator

Optical resonators are the tuning forks of light. Practically, they confine light in the optical modes, resulting in narrow resonances in the frequency domain (Vahala, 2003). These features help in both the territory of linear and nonlinear optics. In linear optical systems, resonators enable applications such as laser frequency stabilization and enhanced cavity–atom interactions. In nonlinear optics, they reduce the power threshold required to access various nonlinear phenomena by increasing the intracavity field intensity. Depending on the order of the nonlinear process ($\chi^{(2)}$ or $\chi^{(3)}$), the enhancement is either proportional to the square or cube of the Q factor, respectively.

To date, three major classes of ultra-high- Q microresonators (those with $Q > 10^8$) have been demonstrated. Fabry–Pérot cavities are among the most mature, achieving Q factors up to ~ 10 billion. However, their bulk nature limits integration and miniaturization, making them unsuitable for large-scale photonic integration. Whispering-gallery-mode (WGM) microresonators offer comparable performance, with demonstrated Q factors exceeding 10^9 . However, they typically require more specialized materials and fabrication processes. For instance, crystalline WGM microresonators have achieved intrinsic Q factors as high as 10^{11} (Savchenkov et al., 2007), but rely on time-intensive mechanical polishing and lack scalability for wafer-level production. Silica wedge microresonators simplifies the fabrication process by using chemical etching, with beyond-billion Q factor (H. Lee, Chen, et al., 2012; L. Wu et al., 2020). More recently, waveguide-based integrated microresonators have emerged as a promising platform. These devices can be fabricated in a planar geometry compatible with photonic integration. Notably, a Q factor of 700 million was recently demonstrated in a silicon nitride (Si_3N_4) waveguide resonator

(Kaikai Liu, N. Jin, et al., 2022), marking a significant advancement in scalable, ultra-low-loss integrated photonics.

Q factor of a microresonator

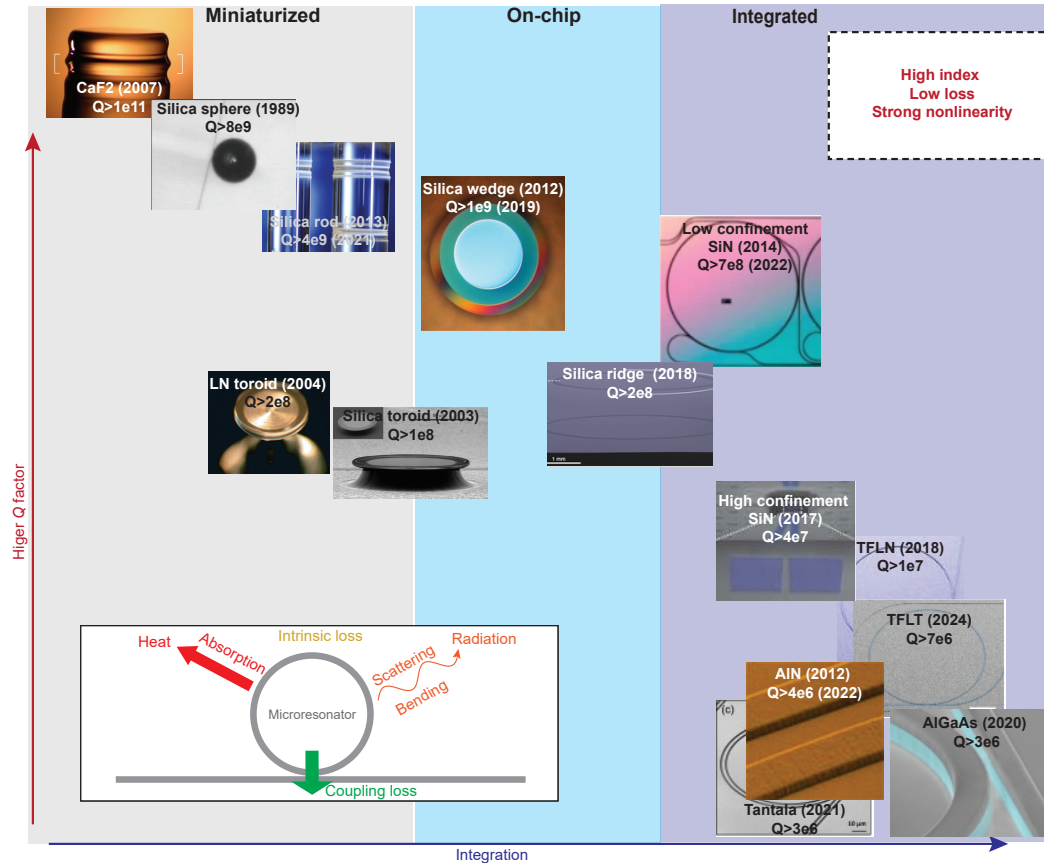


Figure 1.1: **Summary of microresonator platforms.** **Inset:** Schematic showing optical loss channels for high- Q integrated optical microresonators. The intrinsic loss rate is characterized by the intrinsic Q factor (Q_0). Bus waveguide coupling also introduces loss that is characterized by the external coupling Q factor (Q_{ex}). **Main panel:** The references are: Silica micro-sphere (Braginsky, Gorodetsky, and V. S. Ilchenko, 1989; Vernooy et al., 1998); CaF_2 (Savchenkov et al., 2007); Silica wedge (H. Lee, Chen, et al., 2012; L. Wu et al., 2020); Silica rod (Del’Haye, Scott A Diddams, and Papp, 2013; L. Yao et al., 2022); Silica ridge (2018) (K. Y. Yang et al., 2018); AlGaAs (2020) (Pu et al., 2016; W. Xie et al., 2020); High confinement Si_3N_4 (Xingchen Ji et al., 2017; Pfeiffer, J. Liu, Raja, et al., 2018; J. Liu, Huang, et al., 2021); Low-confinement Si_3N_4 (Spencer et al., 2014; Puckett et al., 2021; W. Jin et al., 2021; Kaikai Liu, N. Jin, et al., 2022); thin-film lithium tantalate (Chengli Wang et al., 2024); thin-film lithium niobate (Cheng Wang et al., 2019); AlN (Pernice, C. Xiong, and Tang, 2012; X. Liu et al., 2017; Kewei Liu et al., 2022); Tantalum (Jung et al., 2021).

The quality factor (Q) of a ring resonator is defined as $Q = \omega_0/\kappa$, where ω_0 is the resonant angular frequency, and κ is the full-width-half maximum linewidth of the resonance in angular frequency. The Q factor can also be interpreted in two equivalent ways: (1) In terms of energy, it represents the ratio of the energy stored in the resonator to the energy lost per optical cycle. (2) It is also proportional to the decay time constant of optical energy within the cavity. Another common metric of the resonator is its finesse $\mathcal{F} \equiv 2\pi FSR/\kappa \equiv Q(2\pi FSR)/\omega_0$, where FSR is the free-spectral-range of the resonator.

The common loss mechanisms of a microresonator are summarized in the inset of Figure 1.1. The Q factor is governed by material absorption, radiation losses (due to scattering and bending), and coupling to external waveguides (cavity loading).

Intrinsic material absorption ultimately limits the achievable Q factor. Impurities such as water, hydrogen, and trace metal ions have been identified as significant absorption sources (Gorodetsky, Savchenkov, and V. S. Ilchenko, 1996; Rokhsari, Spillane, and Vahala, 2004; J. Liu, Raja, et al., 2018; Puckett et al., 2021; Pfeiffer, J. Liu, Raja, et al., 2018). Other mechanisms, including surface and interfacial states, can also contribute to excess loss (Parrain et al., 2015; Guha et al., 2017).

To increase the Q factor, significant effort has gone into developing fabrication techniques and design strategies that reduce scattering losses caused by sidewall and interface roughness (Vernooy et al., 1998; Armani et al., 2003; H. Lee, Chen, et al., 2012; Xingchen Ji et al., 2017; Pfeiffer, J. Liu, Raja, et al., 2018). Coupling non-idealities can also degrade the Q factor, but can be mitigated through optimized coupling structures, such as pulley couplers (Pfeiffer, J. Liu, Geiselmann, et al., 2017; Spencer et al., 2014). Bending loss is another important factor, particularly in low-confinement platforms where tight bends lead to radiation losses (W. Jin et al., 2021; Kaikai Liu, N. Jin, et al., 2022).

Chromatic dispersion of a microresonator

The propagation of light inside a waveguide resonator can be described by the Helmholtz equation,

$$(\nabla^2 - \frac{n^2}{c^2} \frac{\partial^2}{\partial t^2})E(x, y, z, t) = 0. \quad (1.1)$$

For transverse modes in a photonic waveguide, we assume light propagates along the z -direction and the longitudinal electric field component is negligible ($E_z = 0$). We consider a field of the form $E(x, y, z, t) = E(x, y)e^{i(\omega t - \beta z)}$.

Dispersion describes how the effective refractive index of an optical structure, composed of specific materials and geometry, varies with optical frequency. The propagation constant $\beta(\omega)$ can be expanded in a Taylor series around a central frequency ω_0 :

$$\beta(\omega) = \beta(\omega_0) + \beta_1(\omega - \omega_0) + \frac{\beta_2}{2}(\omega - \omega_0)^2 + \dots, \quad (1.2)$$

where β_1 is the inverse of the group velocity, β_2 is the group velocity dispersion, typically expressed in units of ps^2/km . Equivalently, the resonance frequencies of a set of modes within a single mode family (e.g., TE_0) can be expressed as:

$$\omega_m = \omega_0 + D_1(m - m_0) + \frac{D_2}{2}(m - m_0)^2 + \dots, \quad (1.3)$$

where $m - m_0$ is the mode number relative to the mode at $\omega_0 = m_0\beta_0c$, $D_1/2\pi$ is the free-spectral-range (*FSR*), and D_2 is the group velocity dispersion parameter. The propagation and dispersion constants are related by:

$$\omega_m = \frac{2\pi mc}{n_{\text{eff}}L}, \quad \beta_1 = \frac{d\beta}{d\omega} = \frac{d(2\pi m/L)}{d\omega_m} = \frac{2\pi}{LD_1}, \quad (1.4)$$

$$\beta_2 = \frac{d^2\beta}{d\omega_m^2} = -\frac{2\pi}{LD_1^2} \frac{dD_1}{d\omega_m} = -\frac{n_{\text{eff}}D_2}{cD_1^2}. \quad (1.5)$$

Current material platforms of microresonators

Over the past three decades, advances in micro- and nano-fabrication technologies have enabled the realization of integrated optical resonators (microresonators), as summarized in Figure 1.1. In particular, efforts have focused on achieving low optical propagation loss (i.e., high Q factors), while also allowing for precise control of device properties, either defined during fabrication or through post-fabrication tuning. The first generations of high- Q microresonators were demonstrated by Braginsky, Gorodetsky and Ilchenko (Braginsky, Gorodetsky, and V. S. Ilchenko, 1989). Subsequently, high- Q factors (hundreds of millions to a billion) were achieved on silicon substrates using surface-tension-assisted reflow (Spillane, Kippenberg, and Vahala, 2002), and later simplified via chemical etching techniques (H. Lee, Chen, et al., 2012; K. Y. Yang et al., 2018; L. Wu et al., 2020). More recently, high- Q resonators have been integrated into photonic circuits, offering improved control over geometry and dispersion. However, these integrated devices typically exhibited Q factors at least an order of magnitude lower (i.e., in the range of a few million to tens of millions) compared to discrete counterparts, particularly prior to the time of this thesis. Significant breakthroughs occurred around the beginning of this PhD work, when foundry-based fabrication processes enabled dramatic improvements in

Q factors—reaching values close to or exceeding 100 million... (W. Jin et al., 2021; Puckett et al., 2021; J. Liu, Huang, et al., 2021). The platform developed in these works, referred to in this thesis as the low-confinement Si_3N_4 platform, has since become central to the research and will be detailed in the following section.

1.2 CMOS-ready, ultra-low-loss Si_3N_4 platform

Very recently, a new kind of ultra-low-loss integrated photonic platform has emerged, named the low-confinement Si_3N_4 platform (Spencer et al., 2014). The system supports Q factors as high as 700 million (corresponding to propagation loss below 0.03 dB/m) (Kaikai Liu, N. Jin, et al., 2022). Moreover, it can be fabricated on 8-inch wafers in a CMOS foundry with high yield (W. Jin et al., 2021).

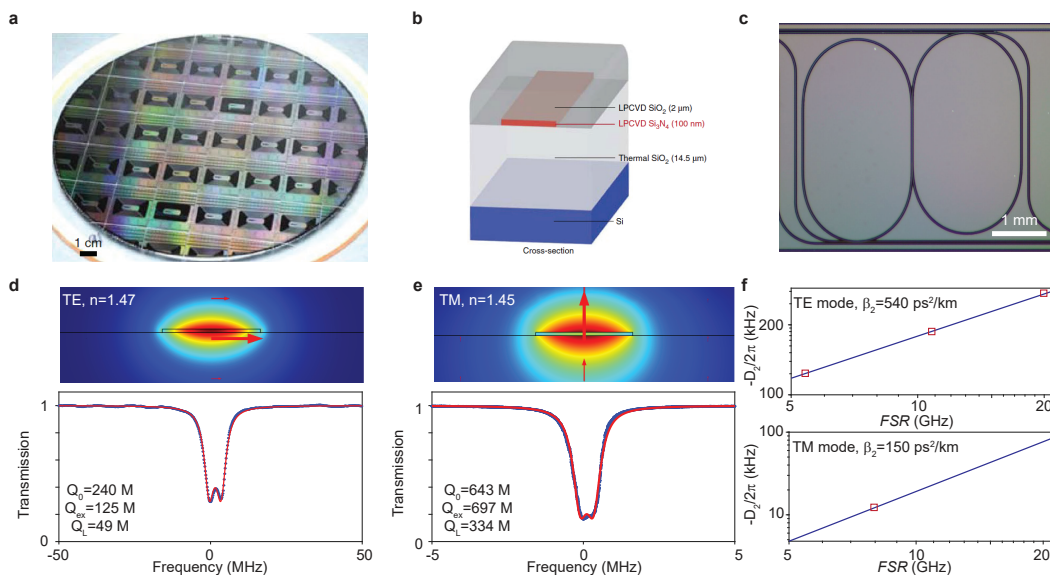


Figure 1.2: The CMOS-ready, ultra-low-loss Si_3N_4 platform. **a**, Photograph showing a fully fabricated, 8-inch (200 mm) wafer with ultra-low-loss Si_3N_4 circuit. **b**, Schematic of cross-section of the structure. Panels a-b are reproduced from (W. Jin et al., 2021). **c**, Photograph of a two-coupled-ring resonator device. **d**, Simulated TE mode of the resonator with Q factor measurement (two identical waveguide couplers are present). The ring resonator is with 16 GHz FSR and 20 μm waveguide width. **e**, Simulated TM mode of the resonator with Q factor measurement (credit to Jin-Yu Liu at Caltech). **f**, Group velocity dispersion (GVD) parameter D_2 of the ultra-low-loss Si_3N_4 platform. Strong GVD is present. Upper panel: from left to right, the waveguide width is 2.8 μm , 20 μm and 2.8 μm , respectively. Lower panel: the waveguide width is 20 μm (data credit to Jin-Yu Liu at Caltech).

An optical photograph of the low-confinement Si_3N_4 platform is shown in Fig-

ure 1.2a. A schematic of the cross-sectional structure is shown in Figure 1.2b. The cross-section features a high-aspect-ratio rectangular waveguide, where the height is 100 nm versus the width (several μm). The waveguide core is fully buried in SiO_2 cladding, providing environmental protection. The high aspect ratio minimizes the overlap between the sidewalls and the electric field, thereby reducing scattering loss caused by lithographically defined sidewall roughness—a major contributor to propagation loss in integrated photonic circuits. In addition, a large fraction of the optical energy resides in the SiO_2 cladding, which further reduces propagation loss, as the material absorption in SiO_2 is typically lower than in Si_3N_4 (Gao et al., 2022). The simulated electric field profile of the fundamental TE (TM) mode is shown in Figure 1.2d (e). For the TE (TM) mode, the typical highest intrinsic Q is beyond 200 (600) million. It is also noted that the effective index of the modes is low (compared with the silica index of 1.44). This makes it difficult to make tight bends using the platform, especially for the TM mode.

The major drawback of the low-confinement Si_3N_4 platform is its high and inflexible group velocity dispersion (GVD). The dispersion cannot be efficiently tuned through waveguide width variation, a common strategy in integrated photonics. As shown in Figure 1.2f, for the fundamental TE mode, the dispersion parameter D_2 of various devices—despite differences in free spectral range (FSR) and waveguide width—lies along a trend corresponding to a fixed waveguide GVD of $\beta_2 = 540 \text{ ps}^2/\text{km}$. This value is approximately 20 times larger than the GVD of fused silica ($\beta_2 = 26 \text{ ps}^2/\text{km}$). A similar trend is observed for the TM mode. The elevated and rigid dispersion profile significantly limits applications that rely on engineered dispersion, such as Kerr microcomb generation.

1.3 Applications of high- Q optical microresonators

The common applications of high- Q optical microresonators are high-coherence lasers, optical frequency comb generation and low-noise microwave source. The three applications are usually coupled with each other.

Application in high-coherence lasers

The invention of lasers has revolutionized modern science and technology. Currently, electromagnetic waves at optical frequencies exhibit high spectral purity (100 THz to 800 THz), and can propagate through optical fibers with remarkably low loss. These features enable applications in precise sensing, optical communications, spectroscopy, medical technologies, etc. The spectral purity of a laser can be

boosted by stabilizing the laser to an optical transition (either an atomic transition or an optical cavity), achieving fractional frequency stability as good as 10^{-19} (Aeppli et al., 2024). This has enabled the study of quantum atomic systems to become a ubiquitous tool. However, these highly stable laser systems are usually bulky with high power consumption, thus confined to laboratory environments.

Integrated photonics can potentially reduce the SWaP (Size, Weight and Power) of such systems, and eventually address the demands of field-deployable applications. The idea of generating low-noise optical fields is to stabilize a laser to the resonance of the microresonator. The frequency stability of the microresonator ultimately determines the laser stability. The performance of the locking technique governs how closely the laser inherits this stability.

To create a low-noise optical oscillator, a high-performance reference cavity is crucial. In recent years, the miniaturization of such references has advanced significantly. Fabry–Pérot cavities offer exceptional stability, though they are difficult to integrate. Vacuum-gap Fabry–Pérot cavities significantly reduce thermorefractive noise (N. Jin et al., 2022) and can be miniaturized to millimeter scales. Dielectric materials can also be used to construct FP cavities, but this typically involves trade-offs in either volume or frequency stability (W. Zhang et al., 2020). Whispering-gallery-mode (WGM) cavities offer a compromise between miniaturization and performance, but pose significant challenges for photonic integration and mass production (Liang, V. S. Ilchenko, Savchenkov, et al., 2010; Liang, V. S. Ilchenko, Eliyahu, et al., 2015; H. Lee, Suh, et al., 2013). Waveguide-based integrated resonators (e.g., spiral resonators) are monolithically fabricated on silicon chips, but tend to exhibit broader linewidths and lower frequency stability (B. Li et al., 2021; Kaikai Liu, Chauhan, et al., 2022). Table 1.1 summarizes these comparisons.

There are several methods to stabilize a laser to an optical resonance. Pound–Drever–Hall (PDH) locking (Drever et al., 1983) remains the most robust, employing an electro-optic modulator and active feedback to precisely control the laser frequency. An alternative is Hänsch–Couillaud locking (Hänsch and Couillaud, 1980). Self-injection locking (SIL) (Hemmerich et al., 1990) uses optical feedback within the cavity to stabilize the laser passively, reducing complexity by eliminating active electronics. However, SIL provides limited control at low offset frequencies and offers fewer monitoring capabilities. Nonlinear processes can also contribute to passive noise suppression, including Brillouin lasers (J. Li, H. Lee, Chen, et al., 2012; Lai et al., 2020; Gundavarapu et al., 2019; Loh et al., 2020), Kerr parametric

oscillators (Black et al., 2022; Y. Zhao et al., 2024), and Raman lasers (P.-J. Zhang et al., 2021; Kewei Liu et al., 2022). Such nonlinear mechanisms require resonant pumping and are often combined with auxiliary locking techniques to stabilize the pump laser. Table 1.2 compares these stabilization methods.

Reference cavity type	Fabry–Pérot cavity	WGM cavity	waveguide resonator
Stability	best	good	okay
Cavity linewidth	good	good	okay
Integration	very difficult	difficult	chip integrated

Table 1.1: **Comparison between different miniaturized reference cavities.**

Locking technique	PDH locking	self-injection locking	frequency conversion
Stability	good	okay	okay
Operation	locking feedback	feedback phase sensitive	built-in noise reduction
Hardware	EOM and servo	phase tuner	case-dependent

Table 1.2: **Comparison between different laser stabilization techniques.**

Application in optical frequency comb generation

Optical frequency combs are spectra composed of equidistant laser lines, characterized by a uniform frequency spacing—known as the repetition rate—with spacing uniformity at the level of 10^{-19} (Predehl et al., 2012). Traditionally, these combs are generated using mode-locked lasers, such as solid-state Ti:sapphire or erbium-doped fiber lasers, and are now commercially available.

Recently, frequency combs have been demonstrated using photonic integrated circuits, giving rise to the concept of microcombs. In particular, microcombs based on Kerr nonlinearity have garnered significant attention due to their low threshold power, high coherence, and potential for complete on-chip integration.

Kerr microcombs have been thoroughly reviewed in the literature (Kippenberg, Holzwarth, and S. Diddams, 2011; Kippenberg, Gaeta, et al., 2018), so only the most relevant concepts are summarized here. In essence, a Kerr microcomb is generated by pumping a high- Q resonance with a continuous-wave laser. The Kerr nonlinearity facilitates frequency conversion via parametric four-wave mixing, which generates new comb lines. When properly engineered, the Kerr nonlinearity can compensate for group velocity dispersion, enabling soliton formation and phase coherence across the comb. In this regime, the intracavity field adopts a stable pulse-like waveform, and its periodic extraction via a bus waveguide produces a

frequency comb. The repetition rate is approximately equal to the resonator's free spectral range (FSR), though slight shifts can occur due to nonlinear and dispersive effects.

This elegant generation mechanism is well-suited for integration, especially when combined with high- Q resonators that allow operation at ultra-low pump powers. As such, Kerr microcombs are regarded as one of the most promising pathways toward fully integrated optical frequency comb systems (Stern et al., 2018; Shen et al., 2020; Xiang et al., 2021; Q.-X. Ji, P. Liu, et al., 2024).

Application in low-noise microwave generation

Photonic techniques offer a compelling pathway for generating microwave and millimeter-wave signals with exceptional spectral purity and compact form factors. One foundational approach relies on photo-detection of optical frequency differences—typically between two narrow-linewidth lasers or between comb lines in an optical frequency comb. This method enables access to microwave frequencies that are otherwise difficult to reach electronically, while maintaining low phase noise and excellent frequency stability (Marpaung, J. Yao, and Capmany, 2019).

Several photonic-chip-based implementations have demonstrated this concept. These include opto-electronic oscillators (OEOs) (Maleki, 2011), direct heterodyne detection between two cavity-stabilized lasers (J. Li, H. Lee, and Vahala, 2013; Gundavarapu et al., 2019), and detection of the repetition rate from a stabilized microcomb (Liang, V. S. Ilchenko, Eliyahu, et al., 2015; Yi, Q.-F. Yang, K. Y. Yang, et al., 2015; Yi, Q.-F. Yang, X. Zhang, et al., 2017; Lucas et al., 2020; Q.-F. Yang et al., 2021; L. Yao et al., 2022).

In fact, the world's lowest phase noise microwave signals have been generated via optical frequency division (OFD), a process in which the stability of an optical oscillator is transferred to the microwave domain using an optical frequency comb (Swann et al., 2011; Fortier et al., 2011; X. Xie et al., 2017). The OFD approach achieves orders-of-magnitude improvement in phase noise compared to even the best electronic oscillators, leveraging the high carrier frequency of optical light to suppress thermal noise sources upon division.

Importantly, OFD combines three core photonic technologies: (1) a highly stable optical reference (typically a laser locked to a high-finesse cavity), (2) a coherent optical frequency comb that acts as the phase-preserving divider, and (3) a low-noise photo-detection system to convert the optical pulse train into an electrical signal. Integrated

photonics now makes it possible to shrink all three components onto chip-scale components, opening the door to compact, ultra-low-noise microwave generators with applications in radar, communications, and timing systems. In this thesis, I demonstrate microwave generation via OFD using chip-based microcombs and resonators. The microcomb and the reference laser are jointly engineered as a coupled system to achieve optimal phase coherence and thermal-noise suppression. Furthermore, significant improvements to the individual components—such as linewidth reduction in chip-scale lasers and enhanced comb coherence—provide benefits beyond microwave generation, including optical metrology and time-frequency transfer.

1.4 Organization of the thesis

The thesis is organized as follows. In Chapter 2, I present results on low-noise microwave generation via optical frequency division (Kudelin et al., 2024; Q.-X. Ji, W. Zhang, L. Wu, et al., 2024; Q.-X. Ji, W. Zhang, Savchenkov, et al., 2025). The key outcome is the record-low phase noise achieved among photonic-chip-based platforms: -152 dBc/Hz at 10 kHz offset from a 10 GHz carrier. The design and demonstration of the optical frequency divider (the microcomb) are detailed in Chapters 3 through 5. These chapters include: A near-zero group velocity dispersion (GVD) microcomb realized using a two-coupled-ring resonator (Q.-X. Ji, W. Jin, et al., 2023); Techniques for mode and dispersion control via tuning and multi-modality operation (Q.-X. Ji, P. Liu, et al., 2024); A dispersive-wave-agile microcomb in a three-coupled-ring resonator platform for extended spectral reach (Q.-X. Ji, W. Zhang, Savchenkov, et al., 2025). The pathway toward full system integration is presented in Chapter 6. Preliminary results include: A hybrid-packaged microcomb with improved long-term frequency stability; Integrated piezoelectric tuning for dynamic control and demonstration of stable PDH locking and chip-scale optical frequency division. Supplementary theoretical modeling is included in Appendix A, and additional technical details and measurement data are provided in Appendix B.

References

- Aeppli, Alexander et al. (2024). “Clock with 8×10^{-19} systematic uncertainty.” In: *Physical Review Letters* 133.2, p. 023401.
- Armani, Daniel K. et al. (2003). “Ultra-high-Q toroid microcavity on a chip.” In: *Nature* 421.6926, pp. 925–928.

- Black, Jennifer A et al. (2022). “Optical-parametric oscillation in photonic-crystal ring resonators.” In: *Optica* 9.10, pp. 1183–1189.
- Braginsky, Vladimir B., Mikhail L. Gorodetsky, and Vladimir S. Ilchenko (1989). “Quality-factor and nonlinear properties of optical whispering-gallery modes.” In: *Physics letters A* 137.7-8, pp. 393–397.
- Del’Haye, Pascal, Scott A Diddams, and Scott B Papp (2013). “Laser-machined ultra-high-Q microrod resonators for nonlinear optics.” In: *Applied Physics Letters* 102.22.
- Drever, Ronald WP et al. (1983). “Laser phase and frequency stabilization using an optical resonator.” In: *Applied Physics B* 31.2, pp. 97–105.
- Fortier, Tara M. et al. (2011). “Generation of ultrastable microwaves via optical frequency division.” In: *Nature Photonics* 5.7, pp. 425–429.
- Gao, Maodong et al. (2022). “Probing material absorption and optical nonlinearity of integrated photonic materials.” In: *Nature Communications* 13.1, p. 3323.
- Gorodetsky, Mikhail L., Anatoliy A. Savchenkov, and Vladimir S. Ilchenko (1996). “Ultimate Q of optical microsphere resonators.” In: *Optics Letters* 21.7, pp. 453–455.
- Guha, Biswarup et al. (2017). “Surface-enhanced gallium arsenide photonic resonator with quality factor of 6×10^6 .” In: *Optica* 4.2, pp. 218–221.
- Gundavarapu, Sarat et al. (2019). “Sub-hertz fundamental linewidth photonic integrated Brillouin laser.” In: *Nature Photonics* 13.1, pp. 60–67.
- Hänsch, Theodor W. and Bruno Couillaud (1980). “Laser frequency stabilization by polarization spectroscopy of a reflecting reference cavity.” In: *Optics Communications* 35.3, pp. 441–444.
- Hemmerich, Andreas et al. (1990). “Optically stabilized narrow linewidth semiconductor laser for high resolution spectroscopy.” In: *Optics Communications* 75.2, pp. 118–122.
- Ji, Qing-Xin, Warren Jin, et al. (2023). “Engineered zero-dispersion microcombs using CMOS-ready photonics.” In: *Optica* 10.2, pp. 279–285.
- Ji, Qing-Xin, Peng Liu, et al. (2024). “Multimodality integrated microresonators using the Moiré speedup effect.” In: *Science* 383.6687, pp. 1080–1083.
- Ji, Qing-Xin, Wei Zhang, Anatoliy A. Savchenkov, et al. (2025). “Dispersive-wave-agile optical frequency division.” In: *Nature Photonics*.
- Ji, Qing-Xin, Wei Zhang, Lue Wu, et al. (2024). “Coherent optical-to-microwave link using an integrated microcomb.” In: *IEEE Journal of Selected Topics in Quantum Electronics*.
- Ji, Xingchen et al. (2017). “Ultra-low-loss on-chip resonators with sub-milliwatt parametric oscillation threshold.” In: *Optica* 4.6, pp. 619–624.

- Jin, Naijun et al. (2022). “Micro-fabricated mirrors with finesse exceeding one million.” In: *Optica* 9.9, pp. 965–970.
- Jin, Warren et al. (2021). “Hertz-linewidth semiconductor lasers using CMOS-ready ultra-high-Q microresonators.” In: *Nature Photonics* 15.5, pp. 346–353.
- Jung, Hojoong et al. (2021). “Tantala Kerr nonlinear integrated photonics.” In: *Optica* 8.6, pp. 811–817.
- Kippenberg, Tobias J., Alexander L. Gaeta, et al. (2018). “Dissipative Kerr solitons in optical microresonators.” In: *Science* 361.6402, eaan8083.
- Kippenberg, Tobias J., Ronald Holzwarth, and SA Diddams (2011). “Microresonator-based optical frequency combs.” In: *Science* 332.6029, pp. 555–559.
- Kudelin, Igor et al. (2024). “Photonic chip-based low-noise microwave oscillator.” In: *Nature* 627.8004, pp. 534–539.
- Lai, Yu-Hung et al. (2020). “Earth rotation measured by a chip-scale ring laser gyroscope.” In: *Nature Photonics* 14, pp. 345–349.
- Lee, Hansuek, Tong Chen, et al. (2012). “Chemically etched ultrahigh-Q wedge-resonator on a silicon chip.” In: *Nature Photonics* 6.6, pp. 369–373.
- Lee, Hansuek, Myoung-Gyun Suh, et al. (2013). “Spiral resonators for on-chip laser frequency stabilization.” In: *Nature Communications* 4, p. 2468.
- Li, Bohan et al. (2021). “Reaching fiber-laser coherence in integrated photonics.” In: *Optics Letters* 46.20, pp. 5201–5204.
- Li, Jiang, Hansuek Lee, Tong Chen, et al. (2012). “Characterization of a high coherence, Brillouin microcavity laser on silicon.” In: *Optics Express* 20.18, pp. 20170–20180.
- Li, Jiang, Hansuek Lee, and Kerry J. Vahala (2013). “Microwave synthesizer using an on-chip Brillouin oscillator.” In: *Nature Communications* 4.1, pp. 1–7.
- Liang, Wei, Vladimir S. Ilchenko, D Eliyahu, et al. (2015). “Ultralow noise miniature external cavity semiconductor laser.” In: *Nature Communications* 6.1, pp. 1–6.
- Liang, Wei, Vladimir S. Ilchenko, Anatoliy A. Savchenkov, et al. (2010). “Whispering-gallery-mode-resonator-based ultranarrow linewidth external-cavity semiconductor laser.” In: *Optics Letters* 35.16, pp. 2822–2824.
- Liu, Junqiu, Guan hao Huang, et al. (2021). “High-yield, wafer-scale fabrication of ultralow-loss, dispersion-engineered silicon nitride photonic circuits.” In: *Nature Communications* 12.1, p. 2236.
- Liu, Junqiu, Arslan S Raja, et al. (2018). “Ultralow-power chip-based soliton microcombs for photonic integration.” In: *Optica* 5.10, pp. 1347–1353.
- Liu, Kaikai, Nitesh Chauhan, et al. (2022). “36 Hz integral linewidth laser based on a photonic integrated 4.0 m coil resonator.” In: *Optica* 9.7, pp. 770–775.

- Liu, Kaikai, Naijun Jin, et al. (2022). “Ultralow 0.034 dB/m loss wafer-scale integrated photonics realizing 720 million Q and 380 μ W threshold Brillouin lasing.” In: *Optics Letters* 47.7, pp. 1855–1858.
- Liu, Kewei et al. (2022). “Fundamental linewidth of an AlN microcavity Raman laser.” In: *Optics Letters* 47.17, pp. 4295–4298.
- Liu, Xianwen et al. (2017). “Aluminum nitride-on-sapphire platform for integrated high-Q microresonators.” In: *Optics Express* 25.2, pp. 587–594.
- Loh, William et al. (2020). “Operation of an optical atomic clock with a Brillouin laser subsystem.” In: *Nature* 588.7837, pp. 244–249.
- Lucas, Erwan et al. (2020). “Ultralow-noise photonic microwave synthesis using a soliton microcomb-based transfer oscillator.” In: *Nature Communications* 11.1, pp. 1–8.
- Maleki, Lute (2011). “The optoelectronic oscillator.” In: *Nature Photonics* 5.12, pp. 728–730.
- Marpaung, David, Jianping Yao, and José Capmany (2019). “Integrated microwave photonics.” In: *Nature Photonics* 13.2, pp. 80–90.
- Parrain, David et al. (2015). “Origin of optical losses in gallium arsenide disk whispering gallery resonators.” In: *Opt. Express* 23.15, pp. 19656–19672.
- Pernice, Wolfram, Chi Xiong, and Hong X. Tang (2012). “High Q micro-ring resonators fabricated from polycrystalline aluminum nitride films for near infrared and visible photonics.” In: *Optics Express* 20.11, pp. 12261–12269.
- Pfeiffer, Martin, Junqiu Liu, Michael Geiselmann, et al. (2017). “Coupling ideality of integrated planar high-Q microresonators.” In: *Physical Review Applied* 7.2, p. 024026.
- Pfeiffer, Martin, Junqiu Liu, Arslan S Raja, et al. (2018). “Ultra-smooth silicon nitride waveguides based on the Damascene reflow process: fabrication and loss origins.” In: *Optica* 5.7, pp. 884–892.
- Predehl, Katharina et al. (2012). “A 920-kilometer optical fiber link for frequency metrology at the 19th decimal place.” In: *Science* 336.6080, pp. 441–444.
- Pu, Minhao et al. (2016). “Efficient frequency comb generation in AlGaAs-on-insulator.” In: *Optica* 3.8, pp. 823–826.
- Puckett, Matthew W. et al. (2021). “422 Million intrinsic quality factor planar integrated all-waveguide resonator with sub-MHz linewidth.” In: *Nature Communications* 12.1, pp. 1–8.
- Rokhsari, Hossein, Sean M. Spillane, and Kerry J. Vahala (2004). “Loss characterization in microcavities using the thermal bistability effect.” In: *Applied Physics Letters* 85.15, pp. 3029–3031.

- Savchenkov, Anatoliy A. et al. (2007). “Optical resonators with ten million finesse.” In: *Optics Express* 15.11, pp. 6768–6773.
- Shen, Boqiang et al. (2020). “Integrated turnkey soliton microcombs.” In: *Nature* 582.7812, pp. 365–369.
- Spencer, Daryl T. et al. (2014). “Integrated waveguide coupled Si₃N₄ resonators in the ultrahigh-Q regime.” In: *Optica* 1.3, pp. 153–157.
- Spillane, Sean M., Tobias J. Kippenberg, and Kerry J. Vahala (2002). “Ultralow-threshold Raman laser using a spherical dielectric microcavity.” In: *Nature* 415, pp. 621–623.
- Stern, Brian et al. (2018). “Battery-operated integrated frequency comb generator.” In: *Nature* 562.7727, p. 401.
- Swann, William C. et al. (2011). “Microwave generation with low residual phase noise from a femtosecond fiber laser with an intracavity electro-optic modulator.” In: *Optics Express* 19.24, pp. 24387–24395.
- Vahala, Kerry J. (2003). “Optical microcavities.” In: *Nature* 424.6950, p. 839.
- Vernooy, David W. et al. (1998). “High-Q measurements of fused-silica microspheres in the near infrared.” In: *Optics Letters* 23.4, pp. 247–249.
- Wang, Cheng et al. (2019). “Monolithic lithium niobate photonic circuits for Kerr frequency comb generation and modulation.” In: *Nature Communications* 10.1, p. 978.
- Wang, Chengli et al. (2024). “Lithium tantalate photonic integrated circuits for volume manufacturing.” In: *Nature* 629.8013, pp. 784–790.
- Wu, Lue et al. (2020). “Greater than one billion Q factor for on-chip microresonators.” In: *Optics Letters* 45.18, pp. 5129–5131.
- Xiang, Chao et al. (2021). “Laser soliton microcombs heterogeneously integrated on silicon.” In: *Science* 373.6550, pp. 99–103.
- Xie, Weiqiang et al. (2020). “Ultrahigh-Q AlGaAs-on-insulator microresonators for integrated nonlinear photonics.” In: *Optics Express* 28.22, pp. 32894–32906.
- Xie, Xiaopeng et al. (2017). “Photonic microwave signals with zeptosecond-level absolute timing noise.” In: *Nature Photonics* 11.1, pp. 44–47.
- Yang, Qi-Fan et al. (2021). “Dispersive-wave induced noise limits in miniature soliton microwave sources.” In: *Nature Communications* 12.1, p. 1442.
- Yang, Ki Youl et al. (2018). “Bridging ultrahigh-Q devices and photonic circuits.” In: *Nature Photonics* 12.5, p. 297.
- Yao, Lu et al. (2022). “Soliton microwave oscillators using oversized billion Q optical microresonators.” In: *Optica* 9.5, pp. 561–564.

- Yi, Xu, Qi-Fan Yang, Ki Youl Yang, et al. (2015). “Soliton frequency comb at microwave rates in a high-Q silica microresonator.” In: *Optica* 2.12, pp. 1078–1085.
- Yi, Xu, Qi-Fan Yang, Xueyue Zhang, et al. (2017). “Single-mode dispersive waves and soliton microcomb dynamics.” In: *Nature Communications* 8.1, pp. 1–9.
- Zhang, Pei-Ji et al. (2021). “Single-mode characteristic of a supermode microcavity Raman laser.” In: *Proceedings of the National Academy of Sciences* 118.22, e2101605118.
- Zhang, Wei et al. (2020). “Ultrarrow Linewidth Photonic-Atomic Laser.” In: *Laser & Photonics Review* 14.4, p. 1900293.
- Zhao, Yun et al. (2024). “All-optical frequency division on-chip using a single laser.” In: *Nature* 627.8004, pp. 546–552.

*Chapter 2*PHOTONIC CHIP-BASED LOW-NOISE OPTICAL FREQUENCY
DIVISION

Never measure anything but
frequency!

Arthur Schawlow

In this chapter, I discuss the development of a photonic-chip-based low-noise microwave source using optical frequency division. The primary focus is on identifying and mitigating key noise sources in the system, including those originating from both the optical reference lasers and the microcomb. For the microcomb subsystem, the discussion is centered on two experimentally demonstrated platforms. The first is a self-injection-locked dark-pulse microcomb, reported in (Kudelin et al., 2024; Ji, W. Zhang, Wu, et al., 2024). The second is a bright soliton microcomb featuring an agile dispersive wave, published in (Ji, W. Zhang, Savchenkov, et al., 2025).

2.1 Two-point optical frequency division

Frequencies of electromagnetic waves represent the most precisely measurable physical quantities known to science. Today, the highest-precision measurements rely on frequency spectroscopy—echoing Arthur Schawlow’s maxim: “Never measure anything but frequency” (Hänsch, 2006). State-of-the-art oscillators based on cooled atomic transitions now routinely achieve precision exceeding 19 significant digits (Aeppli et al., 2024). And the precision can be harnessed with electronics via the process called the optical frequency division (OFD), using an octave-spanning, self-referenced optical frequency comb (Diddams et al., 2000; Jones et al., 2000). The self-referenced optical frequency combs have enabled several unprecedented applications, including time and frequency transfer (Giorgetta et al., 2013; Deschênes et al., 2016; Q. Shen et al., 2022; Caldwell et al., 2023), frequency ratio measurement between optical atomic transitions (Rosenband et al., 2008), and the potential re-definition of a second (Le Targat et al., 2013).

Two-point optical frequency division (2P-OFD) trades a portion of this ultimate precision for reduced system complexity, by using a non-self-referenced (i.e., narrower

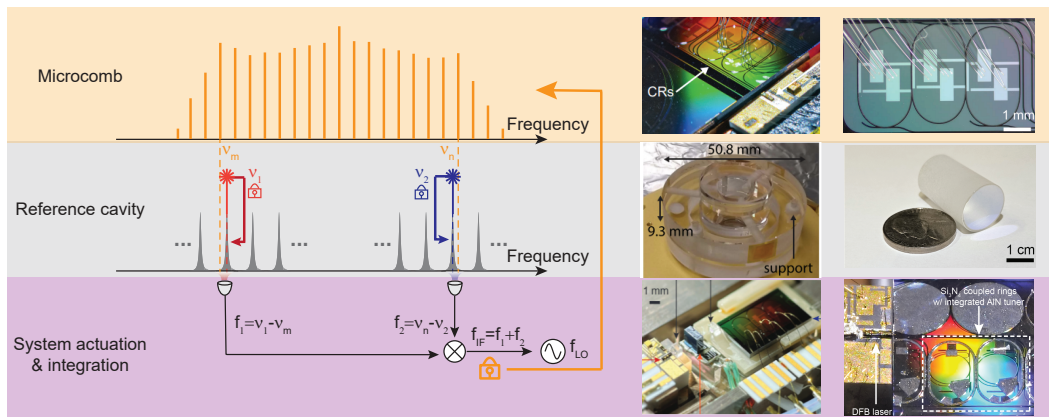


Figure 2.1: Scheme of two-point optical frequency division, with selected publications during my PhD. Microcomb: A dark pulse microcomb (Ji, W. Jin, et al., 2023; Ji, P. Liu, et al., 2024) and a bright soliton microcomb with agile dispersive wave (Ji, W. Zhang, Savchenkov, et al., 2025). Reference cavity: A compact Fabry–Pérot cavity in high-vacuum (Ji, W. Zhang, Wu, et al., 2024) and a vacuum-free bulk Fabry–Pérot cavity (W. Zhang, Kittlaus, et al., 2024). System actuation and integration: a hybrid-packaged microcomb with a III-V laser pump (Ji, W. Zhang, Savchenkov, et al., 2025), and an integrated microcomb with piezoelectric tuner.

spectral span) frequency comb (Swann et al., 2011). This tradeoff enables more compact and practical microwave sources, including commercial systems based on electro-optic combs (J. Li and K. J. Vahala, 2023). Prior to the start of my PhD, several demonstrations of chip-based 2P-OFD had been reported (J. Li, Yi, et al., 2014; Kwon et al., 2022). During my PhD, I contributed to two systems that significantly extended performance into the ultralow phase-noise regime while advancing photonic integration (Kudelin et al., 2024; Ji, W. Zhang, Savchenkov, et al., 2025). In parallel, other research groups have also reported photonic 2P-OFD implementations (Zhao et al., 2024; Sun, B. Wang, et al., 2024; X. Jin et al., 2024; Sun, Mark W. Harrington, et al., 2024; Y. He et al., 2024).

In a microcomb-based 2P-OFD system (illustrated in Fig. 2.1), spectral endpoints of the comb (orange box) are interfaced to two lasers stabilized to optical references (gray box), such as FP cavity resonances. Electrical mixing eliminates the optical carrier frequency of the microcomb, and generates error signal f_{IF} related to $(n - m)$ times the repetition rate. Locking actuation of the microcomb stabilizes f_{IF} to a local oscillator f_{LO} with negligible additive phase noise (orange arrow in Figure 2.1). The repetition rate is accordingly stabilized, where $f_{rep} = (\nu_2 - \nu_1 + f_{IF}) / (n - m)$. This effectively transfers the optical reference stability to the comb repetition rate, which

can be photodetected to generate a spectrally pure microwave signal. The single-sideband (SSB) phase noise spectrum of the resulting microwave tone is given by:

$$S_{\text{rep}}(f) = \frac{S_{\nu_2-\nu_1}(f) + S_{\text{IF}}(f)}{(n-m)^2} + S_{\text{SNR}}(f) + S_{\text{PD}}(f), \quad (2.1)$$

where $S_{\nu_2-\nu_1}(f)$ is the relative frequency noise of the two optical reference lasers, $S_{\text{IF}}(f)$ is the locking residual noise of the microcomb locking system, $S_{\text{SNR}}(f)$ is the contribution from signal-to-noise ratio limitations in the locking electronics, and $S_{\text{PD}}(f)$ is the noise floor set by photo-detection. In the remainder of this chapter, each of these contributions is examined in detail through real system implementations.

2.2 Miniaturized, low-noise optical references

In this section, the approach used to reduce $S_{\nu_2-\nu_1}(f)$, which represents the differential noise between the two optical references, is discussed.

The principle of the Pound Drever Hall (PDH) technique can be summarized as: “We will quickly measure what the laser actually is doing, compared with our desired behavior, and then use feedback onto suitable actuators to control the laser’s frequency. If we can make the corrections quickly enough and accurately enough, then the controlled laser will very closely approximate the ideal frequency stable laser we need” (John L. Hall, 2006).

Figure 2.2a shows the full experimental setup for PDH locking of two continuous wave (CW) lasers used in the two point optical frequency division system. It comprises two individual PDH subsystems along with additional optical and electronic components for laser multiplexing and de-multiplexing. In addition, residual amplitude modulation (RAM) control loops are implemented for both lasers (Wong and John L. Hall, 1985; W. Zhang, Martin, et al., 2014), although these may be omitted depending on system requirements.

Optimization of the PDH locking system

The PDH locking technique operates by phase-modulating the laser light to generate frequency sidebands, which, unlike the carrier, do not couple into the cavity and are predominantly reflected. The interference between the reflected sidebands and the carrier encodes phase information about the laser’s detuning from the cavity resonance. This reflected signal is detected and demodulated to produce an error signal that is highly sensitive to frequency deviations. Because the PDH method uses phase-sensitive detection and is largely immune to amplitude noise, it enables

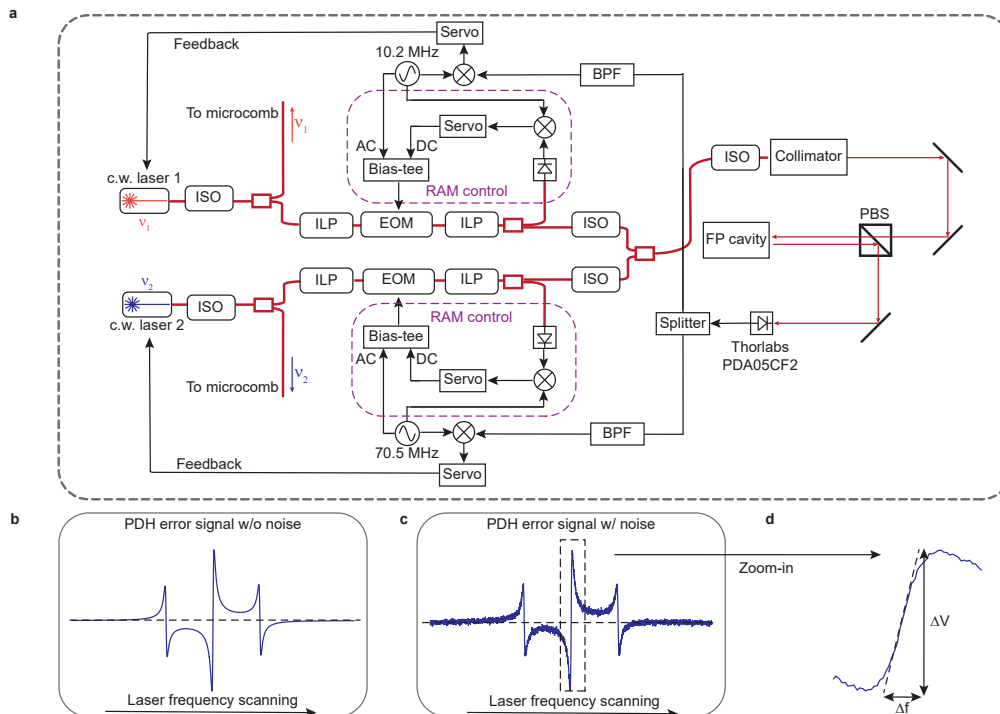


Figure 2.2: PDH locking setup. **a**, Experimental setup of the PDH locking subsystem for the two point optical frequency division system. ISO: isolator. ILP: in-line polarizer. EOM: electro-optic modulator. BPF: bandpass filter. PBS: polarization beam splitter. **b**, Ideal PDH error signal in the absence of experimental noise. **c**, Illustration of a realistic PDH error signal with typical experimental noise. **d**, Zoomed in view of the PDH error signal near the locking point. The laser frequency fluctuation Δf is plotted against the corresponding voltage error signal ΔV . The local slope (dashed line) determines the frequency to voltage conversion.

ultra-low-noise frequency stabilization.

Figure 2.2b gives an (ideal) example of the error signal, when the laser's frequency is scanned across the resonance of the reference cavity. The three zero crossings (intersection of the dashed line and the error signal) correspond to the position where the blue sideband, the carrier and the red sideband matches the resonance, respectively. Typically, the zero-crossing corresponding to the carrier is used as the locking point, for maximum signal-to-noise ratio (SNR).

When a laser is PDH stabilized to an optical transition, its noise spectrum is calculated as

$$S_V(f) = S_{\text{cavity}}(f) + S_{\text{in-loop}}(f) + S_{\text{add}}(f), \quad (2.2)$$

where $S_{\text{cavity}}(f)$ is the cavity noise (mostly thermal noise), $S_{\text{in-loop}}$ is the PDH lock-

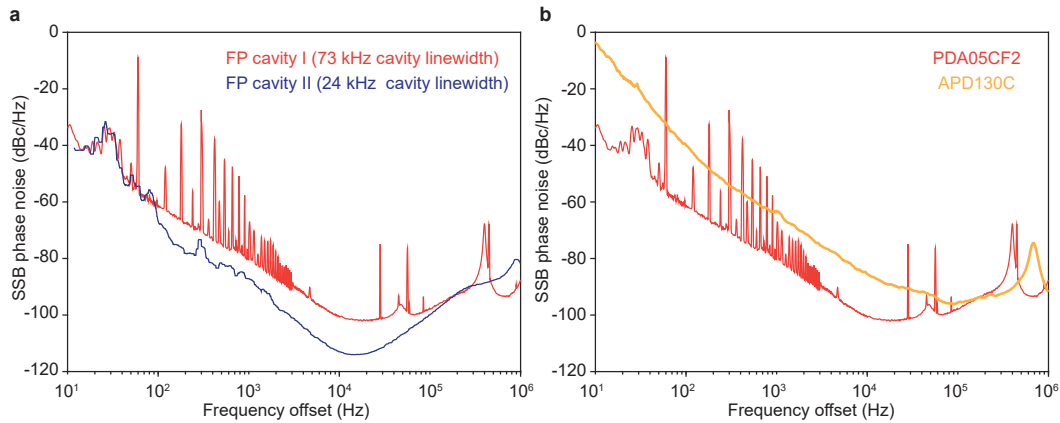


Figure 2.3: **Comparison of laser noise under different PDH locking configurations.** **a**, Comparison of laser relative phase noise when PDH locked to two FP cavities with different cavity linewidth $\delta\nu_C$. **b**, Comparison of laser relative phase noise when PDH locked to the same FP cavity, but using different photo detectors to generate the PDH error signal.

ing residual (in-loop noise), and $S_{\text{add}}(f)$ is additional noise contribution (residual amplitude modulation, PDH error signal-to-noise, etc.). An example of a non-ideal error signal that includes these effects is shown in Figure 2.2c.

With known $S_{\text{cavity}}(f)$ contributed from the cavity, we aim at reducing the noise in $S_{\text{in-loop}}(f)$ and $S_{\text{add}}(f)$. The cavity linewidth $\delta\nu_C$ is critically important, since all the noises are initially electrical error and later converted to the optical frequency error via the slope $\Delta V/\Delta f = -\alpha_{\text{PD}}8\sqrt{P_{\text{carrier}}P_{\text{sideband}}}/\delta\nu_C \equiv \alpha_{\text{PD}}D_{\text{PDH}}$, where $D_{\text{PDH}} \equiv -8\sqrt{P_{\text{carrier}}P_{\text{sideband}}}/\delta\nu_C$ is called the frequency discriminant (Black, 2001), with α_{PD} the photo detector responsivity in volt per Watt, P_{carrier} the carrier optical power, P_{sideband} the sideband optical power. **A smaller cavity linewidth leads to a larger D_{PDH} and is thus preferred for higher sensitivity.** Figure 2.3a shows a comparison using two different cavities (I and II) with different cavity linewidths.

$S_{\text{in-loop}}(f)$ is also greatly affected by the free-running frequency noise of the laser, as well as how fast the laser can be tuned (which determines the achievable locking gain). For better free-running frequency noise of the laser, fiber lasers, self-injection locked semiconductor lasers (W. Jin et al., 2021; B. Li, W. Jin, et al., 2021), or high-end semiconductor lasers (e.g., RIO PLANEX lasers) are possible solutions. For faster tuning control, laser current modulation and frequency tuning using external AOMs are possible. Integrated piezoelectric tuning control is also explored in this thesis (Chapter 6).

The SNR of the PDH error signal is also a limiting factor in noise reduction. Proper selection and use of the photodetector is essential. The incident power to the detector should be right below the saturation power. Additionally, it is important to consider the noise figure and its frequency dependence for the chosen detector. For example, a Thorlabs PDA05CF2 detector offers better performance than a Thorlabs avalanche detector (Thorlabs APD130C), as plotted in Figure 2.3b. In this measurement, FP cavity I is used.

Locking two lasers to the same FP cavity

When locking two lasers to the same cavity, the signals reflecting different lasers should be properly separated. The method used in this case is modulation and demodulation at different frequencies (Figure 2.2a). The choices of the frequencies are not unique, but care must be taken to ensure the harmonics do not interfere with each other.

When locking two lasers to the same cavity separated by a certain amount of optical frequency, the resonant frequencies of the two modes share a certain amount of extra coherence, especially if they belong to the same mode family. This may bring the relative frequency jitter of the two modes lower than the thermal fluctuation of a single optical resonance, where the suppression is referred to as common mode suppression. A more detailed measurement is in (Groman et al., 2024).

2.3 Engineering of the microcomb for 2P-OFD

Larger division factor ($n - m$)

Targeting low-noise microwave/mm-wave generation, photonic chip-based optical frequency combs (microcombs) are another key component in the optical frequency division system. There are several different kinds of microcombs demonstrated to be able to serve as the divider. These include (bright) soliton microcombs (Zhao et al., 2024; Sun, B. Wang, et al., 2024; Sun, Mark W. Harrington, et al., 2024), dark pulse microcombs (part of this work) (Kudelin et al., 2024), and electro-optic microcombs (Y. He et al., 2024). Before these recent demonstrations of optical frequency division, photonic chip-based frequency combs have also been demonstrated in the territory of a clockwork for the miniaturization of optical clocks (Papp et al., 2014; Del’Haye et al., 2014; Newman et al., 2019; Drake et al., 2019).

To build a portable or integrated OFD system, one needs to involve as few “bulky” components and as little power consumption as possible. Electro-optic microcombs have the simplest generating mechanism, but simultaneously require a consider-

ably high-power and stable microwave drive. The fabrication of Lithium Niobate waveguides, which is currently the prominent platform in generating electro-optic combs, is also much more difficult to fabricate yet. The generation of bright soliton microcombs traditionally requires a specific tuning scheme to overcome the thermal problem and access the mode-locked state (Yi, Q.-F. Yang, K. Y. Yang, and K. Vahala, 2016; Stone et al., 2018), which involves an acoustic-optic modulator (AOM), a quadrature phase-shift keying (QPSK), or a secondary powerful laser. Although it is recently simplified under the self-injection lock scheme (Pavlov et al., 2018; B. Shen et al., 2020), it still experimentally suffers from stabilizing a single bright soliton unless other specific designs are added (Ulanov et al., 2024). Besides, the line power drops exponentially when getting away from the pump center, which corrupts the SNR when used in the OFD. Dark pulse microcombs have complicated generation mechanism (H. Wang et al., 2022) and associated “unpredictable” properties (such as line power and temporal profile), but they generally mode-lock easily and stably under an isolated III-V pump (W. Jin et al., 2021). The optical line power at the spectral endpoints is high, so is the generated microwave power when photodetected.

There are significant challenges in generating microcombs using the ultra-low-loss Si_3N_4 platform for the 2P-OFD. (1) The spectral coverage of the comb is narrow, because of the large GVD of the used platform (Figure 1.2). During my PhD, two separate strategies are adapted, including near-zero group velocity dispersion microcomb generation using two-coupled-ring resonator and dispersive wave formation in a three-coupled-ring resonator, which will be introduced in the next two chapters. (2) To achieve low-noise OFD, effective control of the repetition rate is required. This is approached in the next section of the chapter.

Low-noise actuation of the microcomb (smaller $S_{\text{IF}}(f)$)

For a low-noise 2P-OFD system, fast actuation is required to reduce $S_{\text{IF}}(f)$, so that f_{IF} closely follows the low-noise f_{LO} in Figure 2.1. In a typical servo system with integration gain, the in-loop noise is reduced from the free-running level by 20 or 40 dB per decade toward lower offset frequencies, starting from the corner frequency of the servo loop. As a result, a higher corner frequency is always preferred. Since the achievable corner frequency is ultimately limited by the actuator, faster actuation is essential for reducing $S_{\text{IL}}(f)$.

A quiet free-running state of the microcomb is important. Operating the microcomb

near its “quiet point” can help achieve this (Yi, Q.-F. Yang, X. Zhang, et al., 2017; Lucas et al., 2020; Q.-F. Yang et al., 2021). Specifically, under the pump laser self-injection locking mode, excess $1/f$ frequency noise is widely observed for bright solitons (Voloshin et al., 2021), dark pulse microcomb (Ji, W. Jin, et al., 2023; Lihachev et al., 2022), second harmonic generation (B. Li, Yuan, et al., 2023) and Brillouin laser (Ji, P. Liu, et al., 2024). The origin of this noise is yet not understood.

It is also worth noting that, in the case of 2P-OFD, only the repetition rate (f_{rep}) is stabilized and actuated, while the optical carrier frequency (f_0) remains free-running. In some applications, both f_{rep} and f_0 must be stabilized, which requires a second actuator. Ideally, a good actuator should allow for independent control of f_{rep} and f_0 (Newbury and Swann, 2007; W. Zhang, Lours, et al., 2012). However, this remains challenging, as changes in f_{rep} and f_0 are strongly correlated in microcombs (Lei et al., 2022).

Improvement of SNR in the 2P-OFD (lower $S_{\text{SNR}}(f)$)

The limited signal-to-noise ratio (SNR) of microcomb locking imposes a floor—typically in the form of white phase noise—on the stabilized f_{rep} . To reduce $S_{\text{SNR}}(f)$, it is critically important to control both the optical power and the frequency of the comb lines at the spectral endpoints used in the 2P-OFD. High optical power at these endpoints is necessary for generating low-phase-noise microwave signals upon photo-detection, while accurate frequency positioning is essential for coarse alignment with the reference laser frequencies. Achieving both conditions simultaneously presents a significant challenge in microcomb systems. Careful handling of the beatnote signals in the electronic feedback loop is also essential. As illustrated in Figure 2.4, two low-pass filters are employed to suppress harmonic distortion in the electrical mixing. The power levels of the beatnotes must be properly conditioned, either amplified using low-noise amplifiers or attenuated—to meet the input specifications of the electrical mixer. After mixing, the output is passed through a band-pass filter that selects the intermediate frequency ($f_1 + f_2$), which is then amplified to approximately 0 dBm.

Characterization of the 2P-OFD results

The primary goal of the 2P-OFD system is to generate a low-noise microwave tone, whose noise spectrum should be precisely measured. This is a rather specific topic, and is briefed in detail in Chapter B.4. In addition, several intermediate measurements are useful for diagnosing the performance limits of the system, as

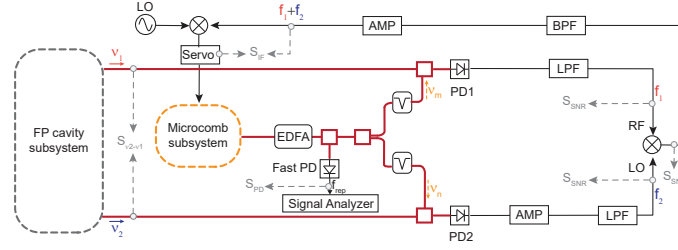


Figure 2.4: **2P-OFD locking setup.** EDFA: erbium-doped fiber amplifier. PD: photo detector. LPF: low-pass filter. BPF: band-pass filter. AMP: amplifiers. LO: local oscillator.

indicated by the gray dashed arrows in Figure 2.4. These relate to the terms in Equation 2.1:

- (1) $S_{PD}(f)$ typically manifests as white phase noise and can be inferred from the phase noise floor of the free-running f_{rep} .
- (2) $S_{SNR}(f)$ is also generally white phase noise and should be monitored at several points by inspecting beatnotes using an electrical signal analyzer (ESA). A typical setup involves centering the ESA around the beatnote with a 10 MHz span and a resolution bandwidth (RBW) of 10 kHz or 100 kHz. The resulting noise limit due to finite SNR is given by:

$$S_{SNR} = \frac{1}{SNR \times RBW} \times \frac{1}{(n - m)^2}.$$

For example, if the SNR is 60 dB with a 10 kHz RBW and $(n - m)^2 = 10^4$, then $S_{SNR} = -140$ dBc/Hz for f_{rep} .

- (3) $S_{IF}(f)$ can be characterized either by measuring the phase noise of $f_{IF} = f_1 + f_2$ directly, or by monitoring the residual error signal from the servo loop. Caution is needed, as the error monitor often contains a built-in low-pass filter that may distort the true error spectrum.
- (4) The relative phase noise between the two lasers, $S_{\nu_2 - \nu_1}(f)$, is difficult to measure directly at THz frequencies. As an approximation, the lasers can be tuned to be separated by one or more FSRs of the FP cavity and locked with identical PDH parameters. Their beatnote—now in the microwave domain—can be measured using standard microwave phase noise techniques (similar to Figure 2.3), and the result scaled down by $(n - m)^2$.

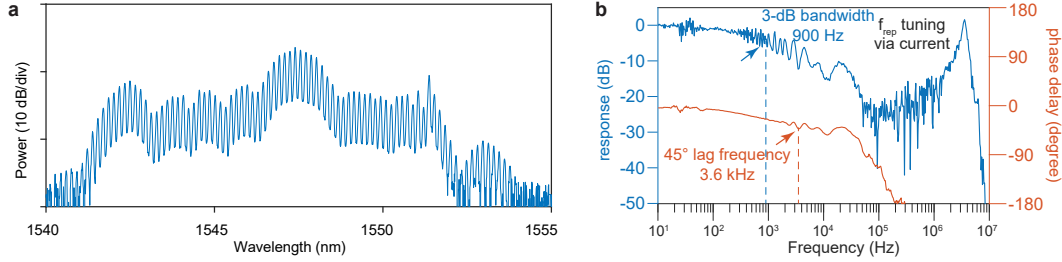


Figure 2.5: **DFB current tuning response bandwidth characterization.** **a**, Optical spectrum of the dark pulse microcomb. **b**, Tuning response of the f_{rep} when the DFB current is tuned. DC tuning efficiency is 69 kHz/mA.

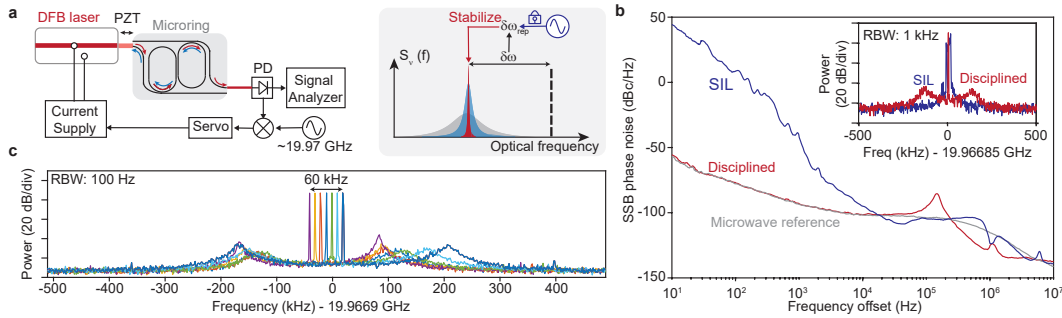


Figure 2.6: **Discipline of the SIL microcomb repetition rate to an external microwave reference.** **a**, Experimental setup for external disciplining of the SIL microcomb repetition rate. PZT: Piezo-electric transducer. PD: photo detector. Servo: laser servo. Inset: schematic view of laser detuning $\delta\omega$ stabilization via repetition rate discipline. Fluctuation in $\delta\omega$ leads to fluctuation in repetition rate $\delta\omega_{\text{rep}}$, which is measured and compared to a microwave reference to generate the error signal for feedback to the laser driving current. Frequency noise of the free-running DFB laser (gray) is reduced by SIL (blue) and then reduced further by repetition rate locking (red). **b**, Repetition rate phase noise and microwave spectra of the free-running SIL microcomb (blue) and the externally disciplined microcomb (red). Measured phase noise of the microwave reference is plotted in gray.

2.4 Dark pulse microcombs in two-coupled-ring resonator

The self-injection-locked (SIL) dark pulse microcomb operating near the zero second-order dispersion regime (Ji, W. Jin, et al., 2023) is used in the 2P-OFD system (Kudelin et al., 2024; Ji, W. Zhang, Wu, et al., 2024), based on the two-coupled-ring (2CR) design. Zero second-order dispersion is used to spectrally broaden the microcomb, offering larger division factor $(n - m)^2$ and high SNR in the 2P-OFD. The experiential optical spectrum is in Figure 2.5a (detailed in Chapter 3). Besides, the microcomb is with high pump-to-comb power conversion efficiency (as in Figure 2.5a, with no extra pump attenuation is present). With this optical

spectrum, division across 1 THz frequency span (50 comb lines) is expected.

The actuation of a self-injection locked microcomb is based on the current modulation of the DFB laser. Recall that the repetition rate is mostly determined by the pump-cavity detuning. Naively, the SIL laser-resonator system can be viewed as a nonlinear resonator plus a single-mode laser rate equation, plus the reflection coupling. Theoretical analysis shows that, the laser-cavity detuning is ideally determined by the feedback phase of the SIL, while tuning of pump laser makes little contribution. However, experimentally the SIL laser-resonator system behaves much more complicated than the picture, with behavior including coherence collapse, dual-mode lasing (Galiev et al., 2018), etc.

Experimentally, it is reasonably efficient to control the laser-cavity detuning $\delta\omega$ (thus the microcomb's repetition rate) via direct current modulation. The real mechanism is not well-understood yet, and is believed to be a combination of thermal effect, Kerr nonlinearity and internal laser dynamics. With laser cavity detuning $\delta\omega$ controlled by the applied current on the pumping DFB laser, a fast feedback loop with laser current as an actuator can be used to stabilize the microcomb's repetition rate. Below are the details of how the modulation of the current on the DFB laser disciplines the microcomb's repetition rate to an external reference, mostly via control of the laser-cavity detuning $\delta\omega$. A measurement of the response in the repetition rate tuning when the pump current is modulated is depicted in Figure 2.5b.

In the repetition rate locking experiment (Figure 2.6a), the microcomb's repetition rate is detected at the resonator drop port by a fast photo detector, and analyzed by a signal analyzer (R&S FSUP). Pumping is at 1559.22 nm. The detected repetition rate tone is simultaneously split by a directional coupler after electrical amplification and mixed with a local oscillator which serves as the reference (R&S SMB 100A). The mixed-down signal is sent to a servo controller and fed back to the current supply (LDX-3620B, DC modulation response bandwidth <1 MHz) of the DFB laser to provide fine tuning control of the pump-laser cavity detuning frequency. The gap distance between the bus waveguide facet and the DFB laser head is regulated by a closed loop piezo (PZT) with a built-in strain gauge displacement sensor (Thorlabs MAX311D).

The measured phase noise of the detected repetition rate tone under open-loop and disciplined (locked) conditions is shown in Figure 2.6b. The phase noise of the microwave reference is shown in gray. The phase noise of the disciplined repetition rate follows that of the microwave reference within the feedback bandwidth

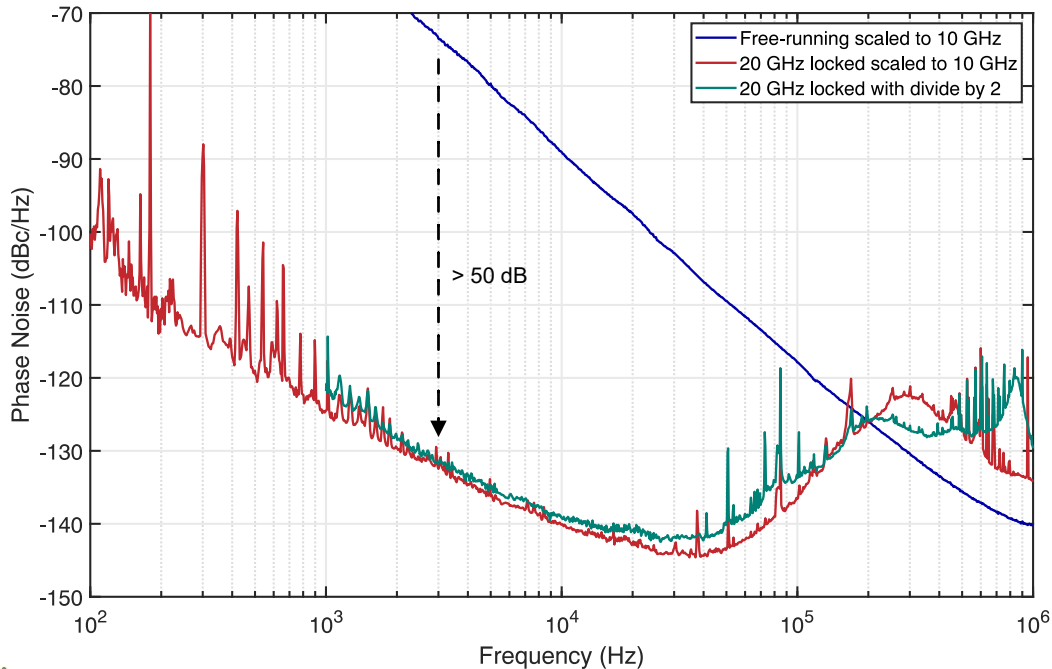


Figure 2.7: **Microcomb phase noise characterization.** Single side-band (SSB) phase noise scaled to 10 GHz of free-running 20 GHz microcomb (blue), locked 20 GHz microwave (red), and locked 20 GHz microwave after regenerative frequency division by 2 (green).

of approximately 100 kHz (as defined by the offset frequency where a “bump” is observed in its frequency spectrum). The microwave spectra of the SIL and disciplined comb are plotted in inset of Figure 2.6b. The repetition rate could be tuned by 60 kHz through tuning of the microwave reference (Figure 2.6c).

Figure 2.7 shows measured phase noise of the microcomb at NIST, under the 2P-OFD. Results credit to Kudelin and Groman.

2.5 Bright soliton microcomb with agile dispersive waves

2P-OFD is also demonstrated using a bright soliton microcomb with spectral endpoints that are both high in power and frequency tunable (Ji, W. Zhang, Savchenkov, et al., 2025). These features in combination with the spectral reach of microcomb achieve optical division noise reduction to a detectable microwave signal. For bright solitons, the f_{rep} is mainly determined by the laser-pump detuning, through the mechanisms including stimulated Raman self-frequency shift and dispersive wave recoil (Yi, Q.-F. Yang, X. Zhang, et al., 2017). The mechanism happens within the cavity life time ($>$ MHz bandwidth), thus is fast enough for repetition rate actuation. Then

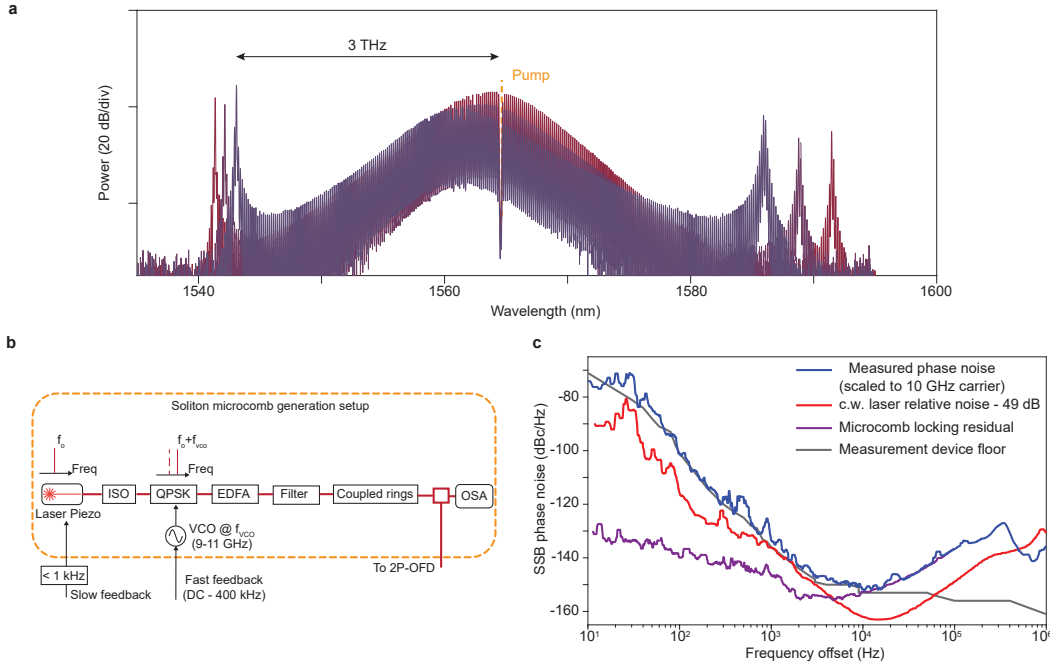


Figure 2.8: 2P-OFD Details. **a**, Optical spectral of bright soliton microcomb showing tuning of the dispersive waves. 2P-OFD across 3 THz is possible. **b**, Experimental setup for bright bright soliton microcomb generation. A c.w. laser (Orbits lightwave) near 1565 nm is isolated (ISO), frequency-shifted by a quadrature phase shift key modulator (QPSK), and amplified by an Erbium-doped fiber amplifier (EDFA). The light is then bandpass filtered to reduce the amplified spontaneous emission noise and coupled to the resonator chip using a lensed fiber. The coupled on-chip power is ~ 150 mW. Most of the soliton power is routed to the 2P-OFD system (see text). A small portion is monitored by an optical spectrum analyzer. **c**, Phase noise spectra summary of the generated microwave signal in the 2P-OFD experiment. All noise levels are scaled to a 10 GHz carrier.

it comes to the fast control of either the pump laser frequency, or the cavity resonant frequency. In this work, it is achieved by tuning the pump laser frequency using a quadrature phase-shift keying (QPSK); in the future, it could potentially be replaced with monolithic-integrated piezo-electric control (J. Liu, Tian, et al., 2020).

As detailed in Figure 2.8, a fiber laser (Orbits Lightwave) is isolated and frequency-shifted by a QPSK (KG), where a sideband serves as pump. The QPSK is driven by a voltage-controlled oscillator (Hittite 108646-1), whose tuning range is artificially reduced (by adding attenuation to Vtune) to 9-11 GHz to reduce its phase noise. The pump is amplified by an erbium-doped fiber amplifier (EDFA, IPG Photonics) and filtered by a notch filter to reduce the amplified spontaneous emission noise. The microcomb is triggered using the method described in (Stone

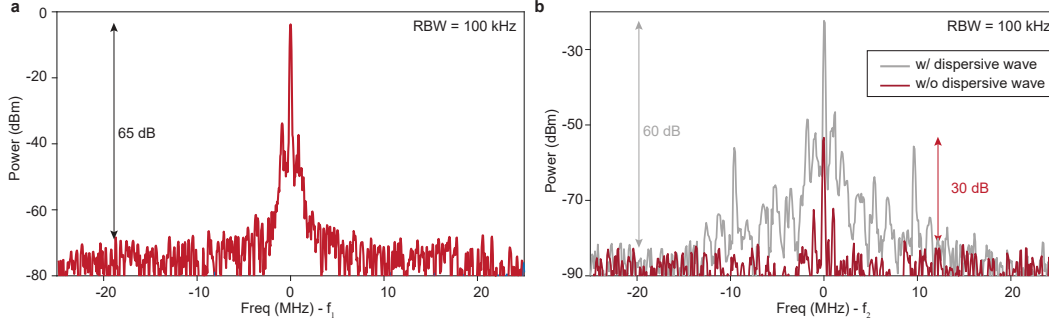


Figure 2.9: **Measured beatnotes f_1 and f_2 in Figure 2.1 with and without dispersive-wave enhancement.** **a**, Measured beatnote between the stabilized c.w. laser (ν_1) and comb line (ν_m), where f_1 is 507.4 MHz. An SNR of 65 dB is measured with resolution bandwidth of 100 kHz. **b**, Measured beatnote between the stabilized c.w. laser (ν_2) and the dispersive wave (ν_n). An SNR of 60 dB is measured with resolution bandwidth of 100 kHz. f_2 is 743.6 MHz for the case with dispersive wave, and $f_2 = 979.9$ MHz for the case without the dispersive wave. A 30 dB improvement in SNR is demonstrated with the dispersive wave.

et al., 2018), and is stable without feedback for a while. The output of the microcomb is collected at the drop port to reject the pump, and amplified by another EDFA (Armonics) to about 60 mW. 75 % of the amplified power is split evenly and filtered by two optical bandpass filters to select two desired comb lines. These are combined with their respective stabilized c.w. laser, and detected by two photo detectors (New Focus 1611) to generate beatnotes at frequencies f_1 and f_2 . The formation of the dispersive wave improves the signal to noise ratio (SNR) of this beatnote by 30 dB (Figure 2.9). This enhancement makes possible 2P-OFD over this broader comb span of 3 THz (i.e., $\nu_n - \nu_m$). The two beatnote signals are electrically amplified before mixing to generate their frequency-summed signal. This signal at frequency f_{LO} is amplified and mixed with a local oscillator at 1.25 GHz to generate the error signal. The error signal is processed by a servo (Vescent D2-125) for feedback to the microcomb to control its repetition rate. This closed loop thereby implements 2P-OFD.

2.6 Conclusion and summary

Confirmation of microcomb spectral coherence

Equation 2.1 is confirmed experimentally (Ji, W. Zhang, Wu, et al., 2024). We measure the relative phase noise of the two CW lasers ($S_{\nu_2-\nu_1}(f)$) and repetition rate phase noise of the microcomb ($S_{\text{rep}}(f)$) for different OFD ratios $(n - m)^2$. In the measurement of $S_{\nu_2-\nu_1}(f)$, the two lasers are separated by one FSR of the

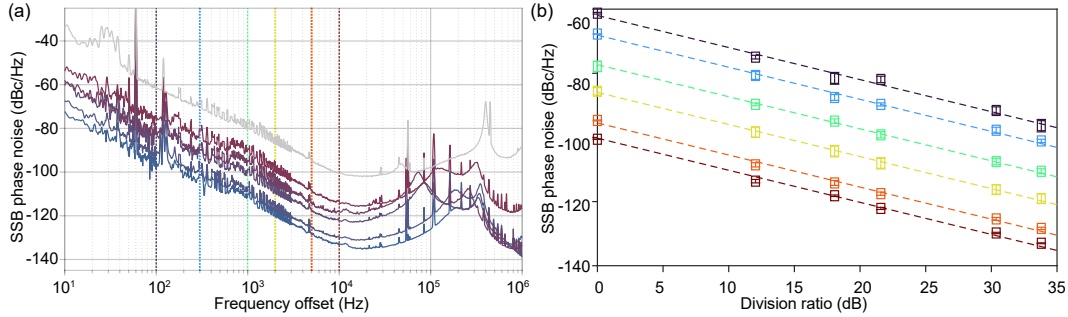


Figure 2.10: Phase noise spectrum measurement of optical and microwave tones confirming the coherent optical-to-microwave link. (a), Gray line: measured SSB phase noise of the relative phase noise of the two lasers. The other lines are measured phase noise of the generated 20 GHz microwave tone using the 2P-OFD. From top to bottom, the division ratio ($n - m$) is 4, 8, 12, 33, 49, respectively. (b), Measured phase noise versus the division ratio at different offset frequencies. From top to bottom, the frequency offset (whose color corresponds to the vertical dashed lines in panel (b)) is 100 Hz, 300 Hz, 1 kHz, 2 kHz, 5 kHz and 10 kHz. The dashed line denotes the theoretical predictions from Equation 2.1.

Fabry–Pérot resonator, and their beating at 16 GHz is detected by a fast photodetector (Thorlabs) followed by characterization with an electrical signal analyzer (R&S FSWP). This relative phase noise of the optical reference is plotted as the upper (grey) curve in Figure 2.10(a). Note that spurs are suppressed in this plot as discussed in the Appendix.

Next, the frequency of the laser at ν_1 (RIO PLANEX) is held fixed while the other laser at ν_2 (Toptica DLC pro) is tuned to other resonances of the Fabry–Pérot cavity. The microcomb is stabilized for each tuning via the aforementioned 2P-OFD scheme, and its detected repetition rate tone is characterized using the signal analyzer. The corresponding phase noise spectra are presented in Figure 2.10(a) for a series of ($n - m$) values: 4, 8, 12, 33, 49. Here, the exact ($n - m$) values are chosen so that the frequency f_1 is lower than 1.5 GHz as required by the electronics used for signal processing. From 10^1 to 10^4 Hz in offset frequency, the microcomb-repetition-rate tone phase noise relative to the optical reference noise scales inversely with the square of the division ratio $(n - m)^2$, as depicted in Figure 2.10(b). The dashed lines in the plots are the theoretical phase-noise scaling. Each phase noise value is calculated by averaging the phase noise around 20 nearby points in the phase noise trace, with the error bar denoting standard deviation of the averaging.

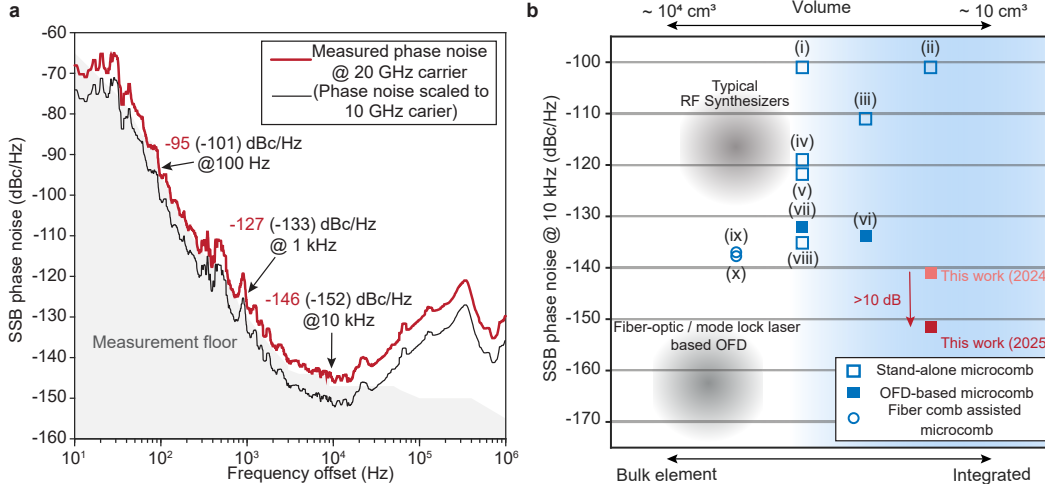


Figure 2.11: Phase noise comparison of microwave generations based on microcomb, scaled to 10 GHz. **a**, Single-sideband phase noise spectrum measurement with carrier frequency near 20 GHz (red). The instrumental measurement floor is the gray shaded area. For comparison, the phase noise is scaled by $\mathcal{L}_{\phi,10\text{GHz}} = \mathcal{L}_{\phi,f_{\text{rep}}} - 20 \times \log_{10}(f_{\text{rep}}/10 \text{ GHz})$, and plotted in black. **b**, The platforms are categorized based on the integration capability of microcomb generator and the reference laser source, excluding the inter-connecting optical/electrical parts. Filled (blank) squares are based on the OFD (stand-alone microcomb) approach. (i) 22 GHz silica microcomb (Yi, Q.-F. Yang, K. Y. Yang, Suh, et al., 2015), (ii) 5 GHz Si_3N_4 microcomb (W. Jin et al., 2021), (iii) 10.8 GHz Si_3N_4 microcomb (J. Liu, Lucas, et al., 2020), (iv) 22 GHz microcomb (J. Li, H. Lee, et al., 2012), (v) MgF_2 microcomb (Liang et al., 2015), (vi) 100 GHz Si_3N_4 microcomb (Sun, B. Wang, et al., 2024), (vii) 22 GHz fibre-stabilised SiO_2 microcomb (Kwon et al., 2022), (viii) MgF_2 microcomb (Matsko et al., 2016), (ix) 14 GHz MgF_2 microcomb pumped by an ultrastable laser (Weng et al., 2019), (x) 14 GHz microcomb-based transfer oscillator (Lucas et al., 2020).

Phase noise performance

Figure 2.11a shows the results obtained in (Ji, W. Zhang, Savchenkov, et al., 2025), which could be viewed as the state-of-the-art phase noise results among those using integrated photonics. Figure 2.11b places the level of phase noise we achieve in context with other photonic approaches, including recent works based on microcombs and mode-locked laser frequency combs. The comparison is classified by level of photonic integration of the microcomb source and pumping/reference lasers, as applicable. It is also noted that some of the microcomb systems require the assistance of a fiber-based frequency comb (Figure 2.11 (ix), (x) (Weng et al., 2019; Lucas et al., 2020)). The phase noise performance of other systems, which could be chip integrated (Figure 2.11 (ii), (iii) (W. Jin et al., 2021; J. Liu, Lucas, et al., 2020)),

is more than 30 dB greater than the results we present, with the exception of the recent work by Sun, *et al.* (vi) (Sun, B. Wang, et al., 2024). Other notable works on low-noise microwave generation in a low-SWaP systems, which are not shown in Figure 2.11, include ‘quite point’ operation (Yi, Q.-F. Yang, X. Zhang, et al., 2017; Lucas et al., 2020; Q.-F. Yang et al., 2021; Yao et al., 2022), single laser optical frequency division (Zhao et al., 2024), and high-end commercial products (*Hi-Q X-band OEO* n.d.; J. Li and K. J. Vahala, 2023; *Ultra-Low-Noise Microwave Oscillator* n.d.).

References

- Aeppli, Alexander et al. (2024). “Clock with 8×10^{-19} systematic uncertainty.” In: *Physical Review Letters* 133.2, p. 023401.
- Black, Eric D. (2001). “An introduction to Pound–Drever–Hall laser frequency stabilization.” In: *American journal of physics* 69.1, pp. 79–87.
- Caldwell, Emily D. et al. (2023). “Quantum-limited optical time transfer for future geosynchronous links.” In: *Nature* 618.7966, pp. 721–726.
- Del’Haye, Pascal et al. (2014). “Self-injection locking and phase-locked states in microresonator-based optical frequency combs.” In: *Physical review letters* 112.4, p. 043905.
- Deschênes, Jean-Daniel et al. (2016). “Synchronization of distant optical clocks at the femtosecond level.” In: *Physical Review X* 6.2, p. 021016.
- Diddams, Scott A. et al. (2000). “Direct link between microwave and optical frequencies with a 300 THz femtosecond laser comb.” In: *Physical Review Letters* 84.22, p. 5102.
- Drake, Tara E. et al. (2019). “Terahertz-rate Kerr-microresonator optical clockwork.” In: *Physical Review X* 9.3, p. 031023.
- Galiev, Ramzil R. et al. (2018). “Spectrum collapse, narrow linewidth, and Bogatov effect in diode lasers locked to high-Q optical microresonators.” In: *Optics Express* 26.23, pp. 30509–30522.
- Giorgetta, Fabrizio R. et al. (2013). “Optical two-way time and frequency transfer over free space.” In: *Nature Photonics* 7.6, pp. 434–438.
- Groman, William et al. (2024). “Photonic millimeter-wave generation beyond the cavity thermal limit.” In: *Optica* 11.11, pp. 1583–1587.
- Hall, John L. (2006). “Nobel Lecture: Defining and measuring optical frequencies.” In: *Reviews of modern physics* 78.4, p. 1279.
- Hänsch, Theodor W. (2006). “Nobel lecture: passion for precision.” In: *Reviews of Modern Physics* 78.4, p. 1297.

- He, Yang et al. (2024). “Chip-scale high-performance photonic microwave oscillator.” In: *arXiv preprint arXiv:2402.16229*.
- Hi-Q X-band OEO* (n.d.). <https://www.oewaves.com/oe3700>. Accessed: 2023-06-18.
- Ji, Qing-Xin, Warren Jin, et al. (2023). “Engineered zero-dispersion microcombs using CMOS-ready photonics.” In: *Optica* 10.2, pp. 279–285.
- Ji, Qing-Xin, Peng Liu, et al. (2024). “Multimodality integrated microresonators using the Moiré speedup effect.” In: *Science* 383.6687, pp. 1080–1083.
- Ji, Qing-Xin, Wei Zhang, Anatoliy A. Savchenkov, et al. (2025). “Dispersive-wave-agile optical frequency division.” In: *Nature Photonics*.
- Ji, Qing-Xin, Wei Zhang, Lue Wu, et al. (2024). “Coherent optical-to-microwave link using an integrated microcomb.” In: *IEEE Journal of Selected Topics in Quantum Electronics*.
- Jin, Warren et al. (2021). “Hertz-linewidth semiconductor lasers using CMOS-ready ultra-high-Q microresonators.” In: *Nature Photonics* 15.5, pp. 346–353.
- Jin, Xing et al. (2024). “Microresonator-referenced soliton microcombs with zeptosecond-level timing noise.” In: *arXiv preprint arXiv:2401.12760*.
- Jones, David J. et al. (2000). “Carrier-envelope phase control of femtosecond mode-locked lasers and direct optical frequency synthesis.” In: *Science* 288.5466, pp. 635–639.
- Kudelin, Igor et al. (2024). “Photonic chip-based low-noise microwave oscillator.” In: *Nature* 627.8004, pp. 534–539.
- Kwon, Dohyeon et al. (2022). “Ultrastable microwave and soliton-pulse generation from fibre-photonic-stabilized microcombs.” In: *Nature Communications* 13.1, p. 381.
- Le Targat, Rodolphe et al. (2013). “Experimental realization of an optical second with strontium lattice clocks.” In: *Nature Communications* 4.1, p. 2109.
- Lei, Fuchuan et al. (2022). “Optical linewidth of soliton microcombs.” In: *Nature Communications* 13.1, p. 3161.
- Li, Bohan, Warren Jin, et al. (2021). “Reaching fiber-laser coherence in integrated photonics.” In: *Optics Letters* 46.20, pp. 5201–5204.
- Li, Bohan, Zhiquan Yuan, et al. (2023). “High-coherence hybrid-integrated 780 nm source by self-injection-locked second-harmonic generation in a high-Q silicon-nitride resonator.” In: *Optica* 10.9, pp. 1241–1244.
- Li, Jiang, Hansuek Lee, et al. (2012). “Low-pump-power, low-phase-noise, and microwave to millimeter-wave repetition rate operation in microcombs.” In: *Physical Review Letters* 109.23, p. 233901.

- Li, Jiang and Kerry J. Vahala (2023). “Small-sized, ultra-low phase noise photonic microwave oscillators at X-Ka bands.” In: *Optica* 10.1, pp. 33–34.
- Li, Jiang, Xu Yi, et al. (2014). “Electro-optical frequency division and stable microwave synthesis.” In: *Science* 345.6194, pp. 309–313.
- Liang, Wei et al. (2015). “High spectral purity Kerr frequency comb radio frequency photonic oscillator.” In: *Nature Communications* 6, p. 7957.
- Lihachev, Grigory V. et al. (2022). “Platicon microcomb generation using laser self-injection locking.” In: *Nature Communications* 13.1, p. 1771.
- Liu, Junqiu, Erwan Lucas, et al. (2020). “Photonic microwave generation in the X-and K-band using integrated soliton microcombs.” In: *Nature Photonics* 14.8, pp. 486–491.
- Liu, Junqiu, Hao Tian, et al. (2020). “Monolithic piezoelectric control of soliton microcombs.” In: *Nature* 583.7816, pp. 385–390.
- Lucas, Erwan et al. (2020). “Ultralow-noise photonic microwave synthesis using a soliton microcomb-based transfer oscillator.” In: *Nature Communications* 11.1, pp. 1–8.
- Matsko, Andrey et al. (2016). “Turn-key operation and stabilization of Kerr frequency combs.” In: *2016 IEEE International Frequency Control Symposium (IFCS)*. IEEE, pp. 1–5.
- Newbury, Nathan R. and William C. Swann (2007). “Low-noise fiber-laser frequency combs.” In: *Journal of the Optical Society of America B* 24.8, pp. 1756–1770.
- Newman, Zachary L. et al. (2019). “Architecture for the photonic integration of an optical atomic clock.” In: *Optica* 6.5, pp. 680–685.
- Papp, Scott B. et al. (2014). “Microresonator frequency comb optical clock.” In: *Optica* 1.1, pp. 10–14.
- Pavlov, Nikolay G. et al. (2018). “Narrow-linewidth lasing and soliton Kerr microcombs with ordinary laser diodes.” In: *Nature Photonics* 12.11, pp. 694–698.
- Rosenband, Till et al. (2008). “Frequency ratio of Al⁺ and Hg⁺ single-ion optical clocks; metrology at the 17th decimal place.” In: *Science* 319.5871, pp. 1808–1812.
- Shen, Boqiang et al. (2020). “Integrated turnkey soliton microcombs.” In: *Nature* 582.7812, pp. 365–369.
- Shen, Qi et al. (2022). “Free-space dissemination of time and frequency with 10-19 instability over 113 km.” In: *Nature* 610.7933, pp. 661–666.
- Stone, Jordan R. et al. (2018). “Thermal and nonlinear dissipative-soliton dynamics in Kerr-microresonator frequency combs.” In: *Physical Review Letters* 121.6, p. 063902.

- Sun, Shuman, Mark W. Harrington, et al. (2024). “Kerr optical frequency division with integrated photonics for stable microwave and mmWave generation.” In: *arXiv preprint arXiv:2402.11772*.
- Sun, Shuman, Beichen Wang, et al. (2024). “Integrated optical frequency division for microwave and mmWave generation.” In: *Nature* 627.8004, pp. 540–545.
- Swann, William C. et al. (2011). “Microwave generation with low residual phase noise from a femtosecond fiber laser with an intracavity electro-optic modulator.” In: *Optics Express* 19.24, pp. 24387–24395.
- Ulanov, Alexander E. et al. (2024). “Synthetic reflection self-injection-locked microcombs.” In: *Nature Photonics*, pp. 1–6.
- Ultra-Low-Noise Microwave Oscillator* (n.d.). <https://www.quantxlabs.com/capabilities/product-development/ultra-low-phase-noise-oscillators/>. Accessed: 2023-07-03.
- Voloshin, Andrey S. et al. (2021). “Dynamics of soliton self-injection locking in optical microresonators.” In: *Nature communications* 12.1, p. 235.
- Wang, Heming et al. (2022). “Self-regulating soliton switching waves in microresonators.” In: *Physical Review A* 106.5, p. 053508.
- Weng, Wenle et al. (2019). “Spectral purification of microwave signals with disciplined dissipative Kerr solitons.” In: *Physical Review Letters* 122.1, p. 013902.
- Wong, Ngai C. and John L. Hall (1985). “Servo control of amplitude modulation in frequency-modulation spectroscopy: demonstration of shot-noise-limited detection.” In: *Journal of the Optical Society of America B* 2.9, pp. 1527–1533.
- Yang, Qi-Fan et al. (2021). “Dispersive-wave induced noise limits in miniature soliton microwave sources.” In: *Nature Communications* 12.1, p. 1442.
- Yao, Lu et al. (2022). “Soliton microwave oscillators using oversized billion Q optical microresonators.” In: *Optica* 9.5, pp. 561–564.
- Yi, Xu, Qi-Fan Yang, Ki Youl Yang, Myoung-Gyun Suh, et al. (2015). “Soliton frequency comb at microwave rates in a high-Q silica microresonator.” In: *Optica* 2.12, pp. 1078–1085.
- Yi, Xu, Qi-Fan Yang, Ki Youl Yang, and Kerry Vahala (2016). “Active capture and stabilization of temporal solitons in microresonators.” In: *Optics Letters* 41.9, pp. 2037–2040.
- Yi, Xu, Qi-Fan Yang, Xueyue Zhang, et al. (2017). “Single-mode dispersive waves and soliton microcomb dynamics.” In: *Nature Communications* 8.1, pp. 1–9.
- Zhang, Wei, Eric Kittlaus, et al. (2024). “Monolithic optical resonator for ultrastable laser and photonic millimeter-wave synthesis.” In: *Communications Physics* 7.1, p. 177.

- Zhang, Wei, Michel Lours, et al. (2012). “Characterizing a fiber-based frequency comb with electro-optic modulator.” In: *IEEE transactions on ultrasonics, ferro-electrics, and frequency control* 59.3, pp. 432–438.
- Zhang, Wei, Michael J. Martin, et al. (2014). “Reduction of residual amplitude modulation to 1×10^{-6} for frequency modulation and laser stabilization.” In: *Optics Letters* 39.7, pp. 1980–1983.
- Zhao, Yun et al. (2024). “All-optical frequency division on-chip using a single laser.” In: *Nature* 627.8004, pp. 546–552.

Chapter 3

DISPERSION ENGINEERING USING COUPLED RING RESONATORS

More is different.

P.W. Anderson

The concept of coupled ring resonators dates back to early studies of supermodes in coupled optical waveguides (Yariv et al., 1999). More recently, it has been extended to the ultra-high- Q regime, notably in coupled toroidal microresonator designs (Grudinin et al., 2010). Applications of two coupled rings (2CR) span a range of physical phenomena and technologies, including Brillouin lasers (Grudinin et al., 2010), non-Hermitian physics and exceptional points (Peng et al., 2014).

In the context of microcomb generation, the 2CR platform offers several key advantages. These include the ability to engineer significant and broadband dispersion modifications for spectral shaping (Kim et al., 2017), introduce controlled mode splitting to facilitate soliton turn-on dynamics (Xue, Xuan, et al., 2015; Helgason, Arteaga-Sierra, et al., 2021), enhance power conversion efficiency (Xue, Zheng, and Zhou, 2019; Helgason, Girardi, et al., 2023), and enable topological protection of soliton states (Tikan et al., 2022).

In this chapter, I present the theoretical framework for dispersion engineering using a pair of Vernier-coupled microring resonators, hereafter referred to as the 2CR platform. This theoretical development is based on work presented in (Ji, W. Jin, et al., 2023; Yuan et al., 2023). I then describe the experimental realization of near-zero group velocity dispersion (GVD) in this system, along with microcomb generation in the integrated 2CR device (Ji, W. Jin, et al., 2023).

3.1 Theoretical dispersion of two-coupled-ring resonator

In this section, dispersion of a pair of Vernierly coupled ring resonator (hereafter referred to as 2CR) is derived. The results are published in (Yuan et al., 2023), where the theoretical calculation is credit to H. Wang and Y. Yu. Earlier work on the calculation of eigen-modes in coupled resonators using similar methods are also present (Boeck et al., 2010). The resonator schematic is shown in Figure 3.1. For

later simplicity, we denote the round trip optical path length of ring A(B) as L_A and L_B , respectively. We now assume that light with a single frequency is propagating in the system. The propagation illustrated in Figure 3.1 is also based on the optical path length, instead of the in the real space. At the points opposite to the coupling region, the field amplitude in each ring is denoted as $\psi_{I,A}$ and $\psi_{I,B}$. These amplitudes can be assembled into a vector as $\psi_I = (\psi_{I,A}, \psi_{I,B})^T$, where T denotes the transpose of a vector or matrix. Similarly, the field just before the coupling part can be found as

$$\begin{pmatrix} \psi_{II,A} \\ \psi_{II,B} \end{pmatrix} = \begin{pmatrix} e^{i\omega(L_A - L_{co})/(2c)} & 0 \\ 0 & e^{i\omega(L_B - L_{co})/(2c)} \end{pmatrix} \begin{pmatrix} \psi_{I,A} \\ \psi_{I,B} \end{pmatrix}. \quad (3.1)$$

For the coupling section, we denote the coupling rate per unit optical path length as g_{co} . The coupling depends on ω , and is assumed to be uniform along the coupling section (i.e., boundary effects from adiabatic bends are included in the effective coupling length). The field after the coupling section can be expressed with a matrix exponential:

$$\begin{pmatrix} \psi_{III,A} \\ \psi_{III,B} \end{pmatrix} = \exp \left\{ \left[iL_{co} \begin{pmatrix} \omega/c & g_{co} \\ g_{co} & \omega/c \end{pmatrix} \right] \right\} \begin{pmatrix} \psi_{II,A} \\ \psi_{II,B} \end{pmatrix}. \quad (3.2)$$

Finally, returning to the points opposite to the coupling region, the field reads

$$\begin{pmatrix} \psi_{IV,A} \\ \psi_{IV,B} \end{pmatrix} = \begin{pmatrix} e^{i\omega(L_A - L_{co})/(2c)} & 0 \\ 0 & e^{i\omega(L_B - L_{co})/(2c)} \end{pmatrix} \begin{pmatrix} \psi_{III,A} \\ \psi_{III,B} \end{pmatrix}. \quad (3.3)$$

For modes in the system, we require the state to reproduce itself after one round trip:

$$\psi_{IV} = e^{i\Theta} \psi_I. \quad (3.4)$$

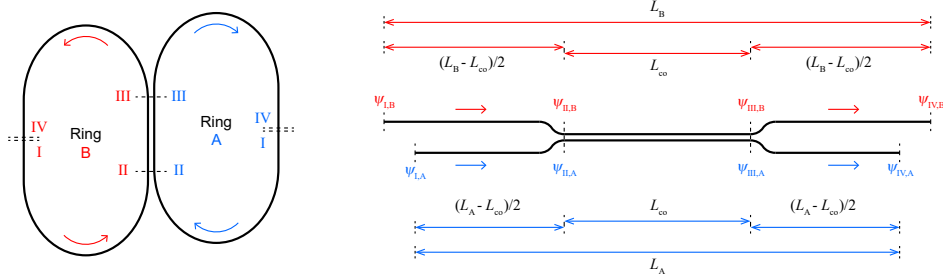


Figure 3.1: **Schematic of the two-ring coupled resonator.** Left panel: Top view of the coupled resonator with key points marked. Right panel: Schematic of the resonator with straightened waveguides (not to scale). Segment lengths and field amplitudes have been marked.

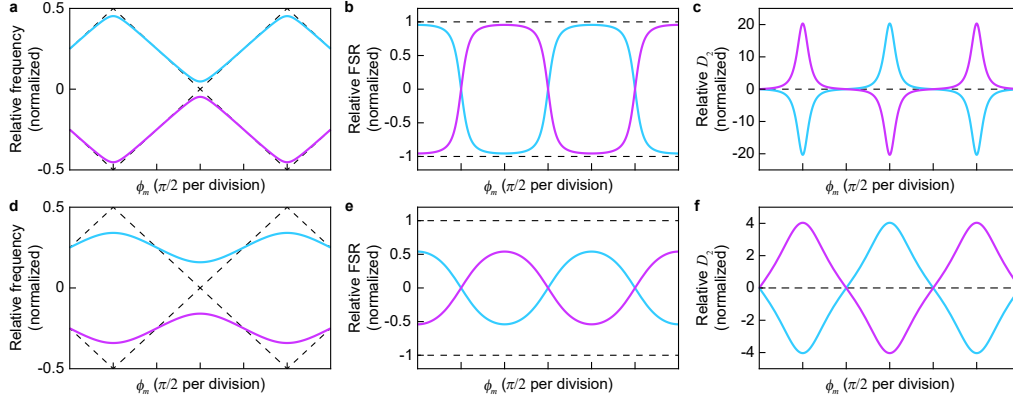


Figure 3.2: Eigenfrequency plots for the two-ring coupled resonator. **a-c** Relative frequency (normalized to $D_{1,m}$), relative FSR (normalized to $\epsilon D_{1,m}$) and relative D_2 (normalized to $\epsilon^2 D_{1,m}$) plots for $g_{co}L_{co} = 0.3$. **d-f** Similar plots but with $g_{co}L_{co} = 1.0$. The horizontal axis is defined as $\phi_m = 2\pi\epsilon m$. Relative mode frequency, FSR and D_2 for individual rings before coupling have been superimposed (black dashed lines). The relative FSR is found by differentiating the relative frequency, and the relative D_2 is found by differentiating the relative FSR.

This requires finding the eigenvalues of the roundtrip transfer matrix T , which is the product of the previous three transfer matrices:

$$\psi_{IV} = T\psi_I, \quad T = e^{i\omega\bar{L}/c} \begin{pmatrix} e^{-i\omega\Delta L/c} \cos(g_{co}L_{co}) & i \sin(g_{co}L_{co}) \\ i \sin(g_{co}L_{co}) & e^{i\omega\Delta L/c} \cos(g_{co}L_{co}) \end{pmatrix}, \quad (3.5)$$

where $\bar{L} = (L_A + L_B)/2$ and $\Delta L = (L_B - L_A)/2$. Each one of the two eigenvalues defines a transverse mode family of the system. Furthermore, when the accumulated phase Θ equals an integer multiple of 2π , a longitudinal mode can be found at the corresponding frequency. Diagonalizing the T matrix gives

$$\Theta = \omega\bar{L}/c \mp \arccos[\cos(g_{co}L_{co}) \cos(\omega\Delta L/c)]. \quad (3.6)$$

Now we define a mode number associated with the average length of the rings:

$$m \equiv \frac{\omega\bar{L}}{2\pi c}. \quad (3.7)$$

The relation can be inverted to give a solution of ω_m dependent on m . When m is an integer, ω_m would be the mode frequencies for a ring resonator with length \bar{L} . As $g_{co} \ll \omega/c$ and $\Delta L \ll \bar{L}$, the phase contribution related to the coupling varies slowly compared to the $\omega\bar{L}/c$ part. This allows us to approximate the coupled mode

frequencies using ω_m , and the eigenfrequencies $\omega_{m,\pm}$ can be solved as:

$$\begin{aligned} 2\pi m &= \omega_{m,\pm} \bar{L}/c \mp \arccos[\cos(g_{\text{co}} L_{\text{co}}) \cos(\omega_{m,\pm} \Delta L/c)] \\ &\approx \omega_{m,\pm} \bar{L}/c \mp \arccos[\cos(g_{\text{co}} L_{\text{co}}) \cos(\omega_m \Delta L/c)], \end{aligned} \quad (3.8)$$

$$\begin{aligned} \omega_{m,\pm} &= \omega_m \pm \frac{c}{\bar{L}} \arccos \left[\cos(g_{\text{co}} L_{\text{co}}) \cos \left(2\pi \frac{\Delta L}{\bar{L}} m \right) \right] \\ &= \omega_m \pm \frac{D_{1,m}}{2\pi} \arccos [\cos(g_{\text{co}} L_{\text{co}}) \cos(2\pi \epsilon m)], \end{aligned} \quad (3.9)$$

where $D_{1,m}$ is the local FSR that depends on ω_m and $\epsilon = \Delta L/\bar{L}$ is the length contrast of the rings. The result shows that the mode structure can be seen as splitting off from the length-averaged resonator modes, where the splitting gap is determined by g_{co} and modulated with respect to mode number with period ϵ^{-1} .

To gain insight into the model, Figure 3.2 plots mode frequency, FSR and the second-order dispersion parameter D_2 relative to ω_m for different values of g_{co} as predicted by Equation (3.9). In these plots ω_m has been subtracted from the mode frequencies, and only the contributions associated with FSR difference of the two rings and the coupling are considered. The $D_{1,m}$ is also approximated as a constant. The FSRs of the transverse modes show a typical avoided crossing behavior as shown in Figure 3.2b and 3.2e. The FSR of one mode continuously transitions to the other mode at the avoided crossing, and similar to the coupling itself, this process is also periodic in the frequency domain. The calculated D_2 shows spikes at the avoided crossing center, and the positive spike can be used to counter the normal dispersion present in the averaged resonator dispersion. Smaller g_{co} leads to higher peak D_2 with smaller crossing bandwidth. To get a larger crossing bandwidth, g_{co} could be increased at the expense of lower D_2 , but the maximum bandwidth is half the modulation period (i.e., the Vernier FSR) as the effect of the neighboring crossings set in and shifts the D_2 in the opposite direction.

In addition to the mode frequency, the mode compositions can also be derived from the transfer matrix T . As the change of mode profile is large enough across the measured optical bandwidth, the mode compositions has an impact on soliton power distribution in the rings, and complements FSRs and dispersions when describing the dispersion characteristics. The eigenvectors of T read,

$$\psi_1 \propto \left(\sqrt{\frac{\sin(\alpha \pm \phi_m)}{2 \sin \alpha \cos \phi_m}}, \mp \sqrt{\frac{\sin(\alpha \mp \phi_m)}{2 \sin \alpha \cos \phi_m}} \right)^T, \quad \phi_m = 2\pi \epsilon m, \quad \alpha = \arccos [\cos(g_{\text{co}} L_{\text{co}}) \cos \phi_m]. \quad (3.10)$$

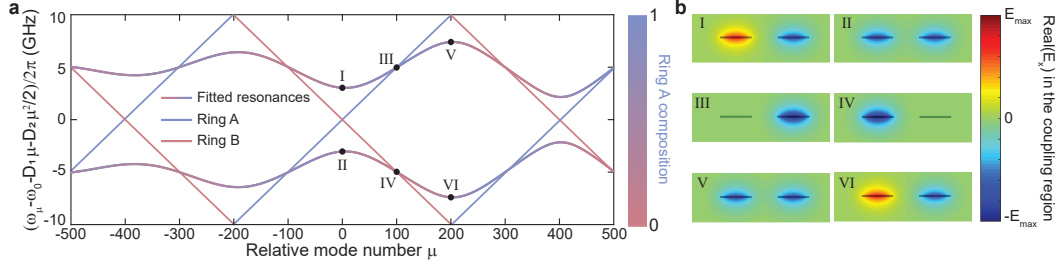


Figure 3.3: Illustration of mode hybridization in the coupling region. **a**, Fitted optical resonance frequency dispersion of the coupled resonator (solid curves) and fitted mode frequency dispersion of the single rings (red and blue lines) plotted versus relative mode number μ . **b**, Cross-sectional view of simulated electric field amplitudes in the coupled region at mode numbers indicated in panel **a** by the black points. The right (left) waveguide belongs to ring A (B). At the crossing center (I, II, V and VI), two waveguides have the same field intensity and the opposite (same) phase for the anti-symmetric (symmetric) mode. When hybrid mode frequencies meet the single-ring resonances (III and IV), the electrical field at the coupled region is contributed by a single ring.

This gives the relative field intensities in the non-coupled regions of the rings for a particular mode. Another point of interest is the center of the coupled region. Here the field can be found as

$$\psi_{co} \propto \begin{pmatrix} \cos(g_{co}L_{co}/2) & i \sin(g_{co}L_{co}/2) \\ i \sin(g_{co}L_{co}/2) & \cos(g_{co}L_{co}/2) \end{pmatrix} \begin{pmatrix} e^{-i\phi_m/2} & 0 \\ 0 & e^{i\phi_m/2} \end{pmatrix} \psi_I \propto \begin{pmatrix} \sqrt{\frac{\sin \alpha \pm \sin \phi_m}{2 \sin \alpha}} & \mp \sqrt{\frac{\sin \alpha \mp \sin \phi_m}{2 \sin \alpha}} \end{pmatrix}^T. \quad (3.11)$$

Similarly, the optical field at any point z in the rings can be calculated and is denoted as $\psi_{A(B)}(z)$. The fractional energy contribution from ring A (η_A) reads as

$$\eta_A = \frac{\int_A |\psi_A(z)|^2 dz}{\int_A |\psi_A(z)|^2 dz + \int_B |\psi_B(z)|^2 dz}. \quad (3.12)$$

There are some special cases of ϕ_m that lead to simplified field distributions and are demonstrated in Figure 3.3. For example, if ϕ_m/π is an integer (crossing centers), the modes become purely symmetrical and anti-symmetrical:

$$\psi_I \propto (\sqrt{1/2}, \mp \sqrt{1/2})^T, \quad \psi_{co} \propto (\sqrt{1/2}, \mp \sqrt{1/2})^T. \quad (3.13)$$

Points I, II, V, and VI in Figure 3.3b belong to these cases. Points II and V are symmetric modes formed by the two rings, with equal mode intensities and the same phase. On the other hand, points I and VI are anti-symmetric modes, with equal mode intensities but opposite phase. These results happen to agree with

coupled-mode calculations when only the pair of degenerate longitudinal modes from each ring are considered. However, while the energy is equally distributed in the two rings in the same way as the reduced coupled-mode theory predicted, other longitudinal modes still participate in the coupling because the wavevector in the coupled region differs from that in the uncoupled region. On the other hand, if ϕ_m/π is a half-integer (halfway between crossing centers), then at the center of coupling position the field is entirely within a single ring:

$$\psi_I \propto (\cos(g_{co}L_{co}/2), \mp \sin(g_{co}L_{co}/2))^T, \quad \psi_{co} \propto (1, 0)^T, \quad (3.14)$$

or,

$$\psi_I \propto (\sin(g_{co}L_{co}/2), \pm \cos(g_{co}L_{co}/2))^T, \quad \psi_{co} \propto (0, -1)^T, \quad (3.15)$$

Points III and IV in Figure 3.3b belong to these cases.

An interesting feature of the field distribution is that, for a single continuous branch, the field compositions exchange parity at the next degeneracy point, and the anti-symmetric mode now becomes the symmetric mode (from point I to V) and vice versa (from point II to VI). The change of parity shows that the modes repeat themselves every two Vernier periods (every two degeneracy points) instead of one, in agreement with Eq. (3.9). While the parity exchange is obvious after plotting the dispersion (Figure 3.3a), it can also be understood from a mode number argument. We consider the total phase accumulated in ring A for a specific mode divided by 2π , which should be an integer and denoted as m_A . This is the ‘‘mode number’’ for ring A for the specific mode. Similarly m_B could be defined. These two numbers equal to the respective mode numbers of the closest uncoupled modes, which can be seen by adiabatically turning off the coupling. For a single Vernier period, the total mode number changes by an odd number. However, going to the next longitudinal mode by changing the frequency alone changes both m_A and m_B by one. The only way to induce a separate mode number change is to create a zero in the field amplitude somewhere in the respective ring, which is indeed the case for points III and IV shown in Figure 3.3b. Considering that the individual mode numbers are about equally distributed around the averaged-length mode number m (e.g., $|(m_B - m) - (m - m_A)| \leq 1$), the extra increment of m_B and decrement of m_A should have taken place alternatively between the Vernier periods, indicating the mode branch switches mode compositions for each Vernier period.

3.2 Device design and characterization

Design and tape-out of the first 2CR device is credit to Warren Jin at UCSB.

Design of the Vernier ring coupling

Based on the theoretical framework in Chapter 3.1, the key design parameters for the two-coupled-ring (2CR) device are the dimensionless coupling strength $g_{\text{co}}L_{\text{co}}$ and the optical path length contrast ϵ between the rings. The design is implemented on a 100-nm-thick Si_3N_4 platform, operating in the TE polarization. The waveguide width is chosen to be $2.8 \mu\text{m}$, the widest geometry that still supports single-TE-mode operation.

The design proceeds as follows:

1. The coupling strength $g_{\text{co}}L_{\text{co}}$ is initially set to $\pi/4$. This ensures sufficiently strong coupling to allow for significant dispersion modification.
2. With $g_{\text{co}}L_{\text{co}}$ fixed, the arched sections of the racetrack resonators are designed with large bending radii to minimize bending losses. This determines $\bar{L} - L_{\text{co}}$, where \bar{L} is the average ring length.
3. The target average free spectral range (FSR) is set to 19.95 GHz, which fixes the value of \bar{L} . Given step (2), this then determines L_{co} , and in turn the coupling coefficient g_{co} .
4. Using COMSOL simulations, g_{co} is mapped to the physical gap spacing between the two resonators at the coupling section. The result is a designed gap of $2.4 \mu\text{m}$.
5. The path length contrast ϵ is chosen such that the resulting mode hybridization period, given by $\text{FSR}/(2\epsilon)$, is both measurable in dispersion characterization and sufficiently large to allow a practical window for microcomb generation. A value of $\epsilon = 1/400$ yields a periodicity of approximately 4 THz.

This design process does not converge to a single optimal set of parameters, but rather represents a compromise among coupling strength, bending loss minimization, and chip-level routing constraints.

After fabrication, the measured coupling strength is $g_{\text{co}}L_{\text{co}} = 0.954$, which is over 10% higher than the nominal design value of 0.785. This discrepancy is attributed to fabrication variations, such as thinner Si_3N_4 layer thickness or lower-than-expected refractive index. Furthermore, the coupling strength exhibits a 5.5% increase per 10 nm toward longer wavelengths. The path length contrast ϵ is precisely controlled by lithographic mask design, and its deviation is estimated to be on the order of 10^{-5} .

Light propagation loss

The sidewall roughness of a 100-nm-thickness, $2.8\text{-}\mu\text{m}$ -width, single ring resonator generally limits the Q_0 to 100-150 million. In the case of the 2CR, under the

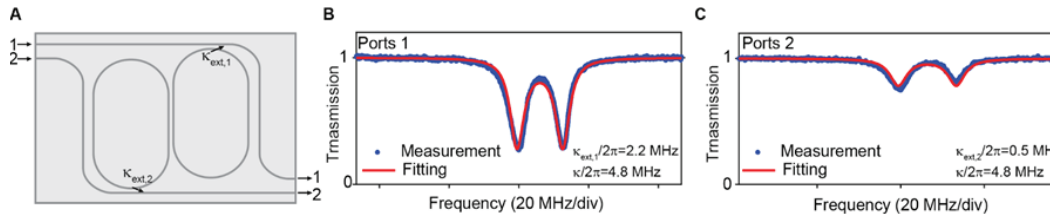


Figure 3.4: **Loss characterization of the 2CR resonator.**

coupled-mode theory, if the two rings are individually with the same Q_0 , then the Q_0 should not be modified for the supermodes, under conservative mode couplings. In reality, the coupling section L_{co} is considerably long (compared with the round-trip \bar{L}). Resultantly, the light in a ring resonator can be efficiently scattered by the sidewall of the other ring resonator at the coupling section, and the Q_0 factor of the supermodes is experimentally reduced to 80 – 120 million level. With this, the coupling Q_{ex} is designed to be around 100 million for critical coupling to a single racetrack resonator. More details of the bus waveguide design can be found in the PhD thesis of Warren Jin (W. Jin, 2022).

As in Figure 3.4, the Q factor of the 2CR is measured by coupling light into port 1 (2) and measuring the transmission at the corresponding port 1 (2), while the laser's frequency is scanned and calibrated. By fitting using a Lorentzian lineshape with back scattering-induced mode splitting (W. Jin et al., 2021), the bus waveguide coupling $\kappa_{ex,1}$ and $\kappa_{ex,2}$ are extracted, and the intrinsic loss rate κ_0 (intrinsic quality factor Q_0) is calculated using $\kappa_0 = \kappa - \kappa_{ex,1} - \kappa_{ex,2}$ and $Q_0 = \omega_0/\kappa_0$. Note that the two bus waveguide coupler is designed to be identical in geometry, and the different $\kappa_{ex,1}$ and $\kappa_{ex,2}$ are due to mode hybridization, that the energy distributes unequally inside the two rings (see Figure 3.3).

3.3 Integrated near-zero-GVD microcomb operation

Soliton mode locking in optical microresonators is receiving intense interest for chip-scale integration of frequency comb systems (Kippenberg et al., 2018; Diddams, K. J. Vahala, and Udem, 2020). An important advancement has been the realization of microcombs that are directly pumped by semiconductor lasers without amplification (Stern et al., 2018; Boqiang Shen et al., 2020; W. Jin et al., 2021; Xiang et al., 2021). These systems have resulted from steady progress in boosting of resonator Q factor so as to lower pumping power, especially in detectable-rate microcombs (Herr et al., 2014; Yi, Q.-F. Yang, K. Y. Yang, Suh, et al., 2015; Liang et al., 2015; Suh and

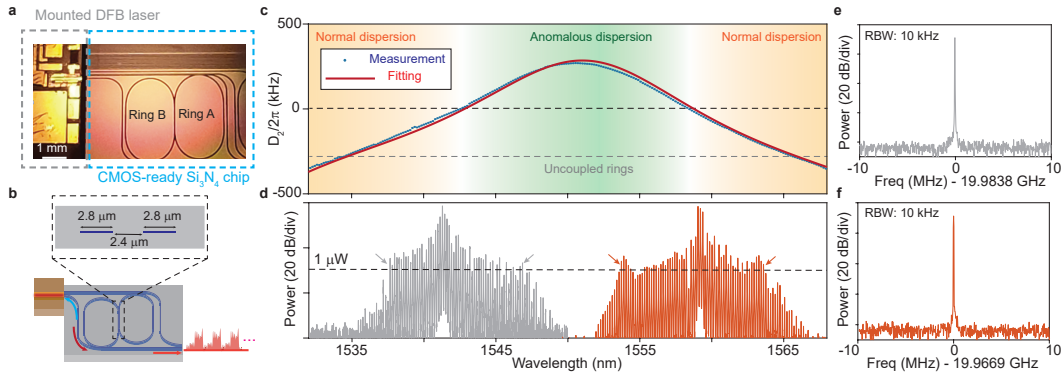


Figure 3.5: Self-injection-locked zero-dispersion microcomb using a coupled-ring resonator. **a**, Photograph of the coupled ring resonators showing DFB pump laser. The two rings are nearly degenerate (FSR difference is ~ 100 MHz). **b**, Lower panel shows the coupled rings pumped by a DFB laser which is self-injection locked to a resonator mode. Periodic pulse trains (light red arrow) are generated. Upper panel shows the cross-sectional waveguide geometry of the ring coupling region ($2.8 \mu\text{m}$ waveguide width and $2.4 \mu\text{m}$ waveguide gap). **c**, Measured group velocity dispersion (GVD) parameter D_2 of the mode resonances versus wavelength. Zero dispersion is achieved near 1542 nm and 1559 nm. **d**, Optical spectra of the generated frequency comb when pumped near the two zero dispersion points. For the comb pumped at 1541 nm (gray), the span is 9.2 nm (as marked by the arrows). For the comb pumped at 1559 nm (orange), the span is 9.9 nm. The dashed line indicates the estimated on-chip line power of $1 \mu\text{W}$. **e,f**, Measured microwave frequency spectrum of the detected microcomb output when pumped at 1542 nm (**e**) and 1560 nm (**f**). The resolution bandwidth is 10 kHz.

K. Vahala, 2018; K. Y. Yang et al., 2018; J. Liu et al., 2020; W. Jin et al., 2021). The directly pumped systems benefit from self-injection-locking (SIL) of the pump by feedback from the microcomb resonator (Konratiev et al., 2017; Pavlov et al., 2017). SIL operation simplifies integration by eliminating the optical isolator component between pump and microcomb, and it also narrows the pump line. Critically, it has also been shown that SIL tends to simplify the soliton turn-on process, making it deterministic (or turnkey) for bright solitons (Boqiang Shen et al., 2020).

Normal GVD dispersion microcombs (Xue, Xuan, et al., 2015) have also been shown to benefit from SIL operation (W. Jin et al., 2021; H. Wang et al., 2022; Lihachev et al., 2022). Not only does the pulse triggering become deterministic, but switching-wave stability dynamics that normally favor large or very small duty cycles, are overcome and pulse duty cycle lies closer to the ideal 50% for maximal comb power and efficiency (H. Wang et al., 2022). This is advantageous for microwave generation as well as for use of the microcomb as a WDM communications source

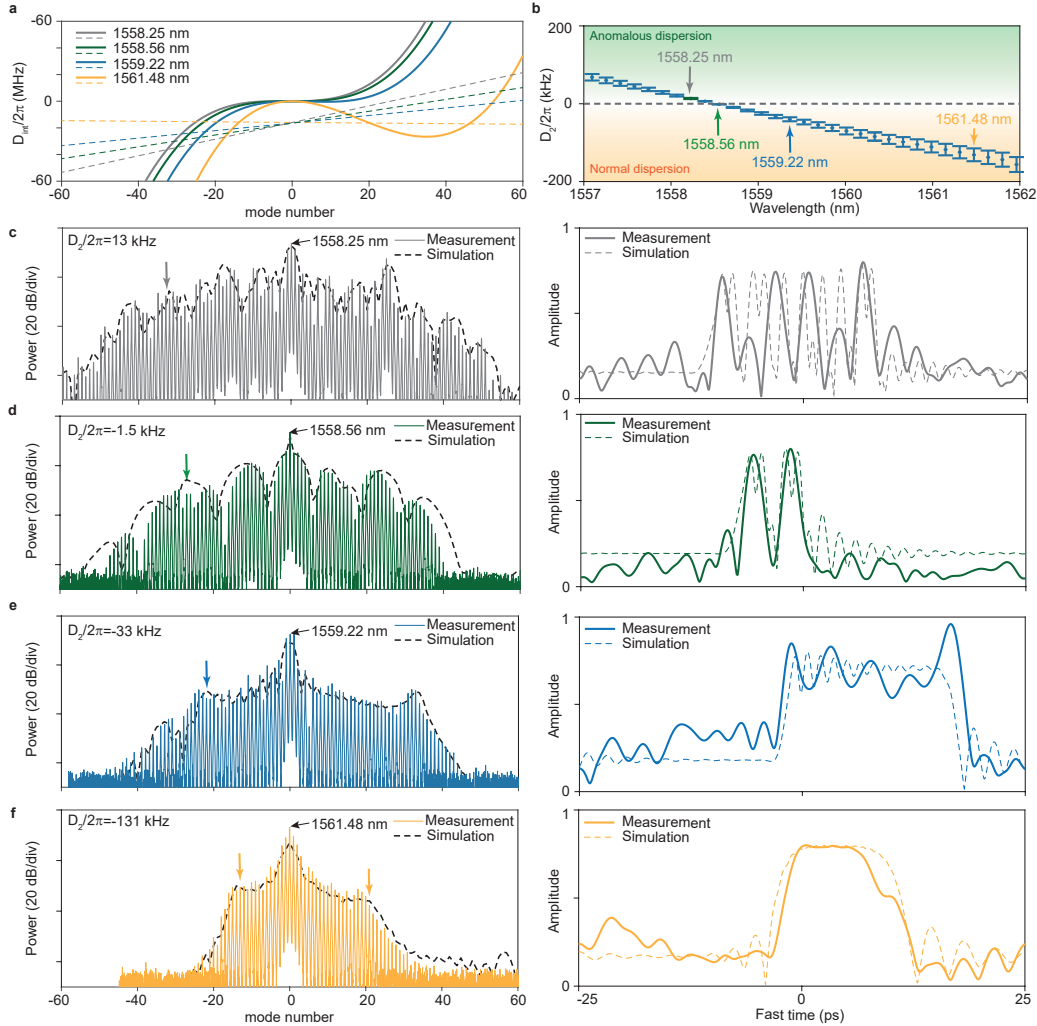


Figure 3.6: Microcomb optical spectra and temporal waveforms measured at specific pumping wavelengths near the zero GVD wavelength. **a**, Solid lines give the integrated dispersion, defined as $D_{int} = \omega_{\mu} - \omega_0 - D_1\mu$ (right-hand side of Equation 3.16), measured at pumping wavelengths shown in the legend. The colored dashed lines denote the comb line frequencies (left-hand side of Equation 3.16) when pumped at the specified pumping wavelengths. The intersection of the mode resonances (solid line) and comb lines (dashed line) generates a dispersive wave. **b**, Measured GVD parameter D_2 versus wavelength near the zero GVD point. Arrows correspond to the pump wavelengths shown in panel a. Errorbar denotes standard deviation from the third-order polynomial fitting. **c-f**, Left panels: optical spectra of the microcomb when pumped near the zero-dispersion wavelength (specific pumping wavelength indicated and correspond to values in panel a). Simulated optical spectrum is plotted as the dashed black curve. The dispersive wave position from panel a is marked by arrows. Right panel: measured microcomb temporal waveform during one round trip for the pumping wavelength given in left panel.

(Fülöp et al., 2018). Despite these useful properties of the normal GVD SIL microcombs, the spectral width of these systems is limited. For example, in high- Q CMOS-ready resonators, comb lines extend to about 4 nm due to the strong normal chromatic dispersion of the low-confinement waveguides (W. Jin et al., 2021). An intriguing approach to extend bandwidth has been to drive microcombs near the zero GVD wavelength where pulse formation is influenced by higher-order dispersion (Anderson, Weng, et al., 2022; S. Zhang, Bi, and Del’Haye, 2023; Z. Li, Xu, Todd, et al., 2021). Besides permitting a range of new pulse behaviors as the system is operated above, below, or near the zero-dispersion wavelength, flattening in the dispersion spectrum is generally possible, which broadens the comb span. Under pulsed pumped operation near octave span detectable repetition rates have been possible (Anderson, Weng, et al., 2022).

Here, dual coupled-ring (CR) resonators are used to produce near-zero-GVD microcombs using the normal dispersion CMOS-ready platform. While prior zero-GVD systems have used pulse pumping or optical amplification of continuous-wave sources, the CR resonators feature high intrinsic Q factors over 100 million (the highest of any CR resonator system), enabling SIL operation of the microcombs with a heterogeneously-integrated III-V laser. This is also the first application of the SIL mode of operation to zero-GVD on-chip systems and it is observed to provide the turnkey benefit previously observed for anomalous and normal dispersion systems, including high efficiency comb operation (H. Wang et al., 2022). Comb bandwidth up to 9.9 nm (1.22 THz) is set by design for application in a two-point optical frequency division system (Papp et al., 2014; J. Li et al., 2014). This significantly improves upon prior CMOS-ready designs and also offers high comb line powers required in the division system. To our knowledge, the number of combs lines generated is a record for non-amplified and non-pulse-pumped zero-GVD systems. The precise stepper-lithography-defined geometry of the CMOS-ready system also enables good control of the zero-GVD wavelength. By tuning the pumping laser near the zero-dispersion point, various mode-locked comb states at microwave rates are observed. And by utilizing the linear optical sampling technique assisted with an electro-optic frequency comb (Yi, Q.-F. Yang, K. Y. Yang, and K. Vahala, 2018), the temporal profiles of these states are measured for the first time including soliton molecules (Anderson, Weng, et al., 2022; S. Zhang, Bi, and Del’Haye, 2023), switching waves (Lihachev et al., 2022; H. Wang et al., 2022) and their hybrids (Anderson, Weng, et al., 2022). Numerical modeling is in agreement with the optical spectra as well as the measured temporal profiles. Servo locking of the microcomb

repetition rate to a microwave reference is also demonstrated and stabilized the comb repetition rate, offset frequency and temporal waveform.

3.4 Dispersion and SIL microcomb spectra

In the measurement, a DFB laser operating in the vicinity of one of the two zero-dispersion wavelengths is butt-coupled to the resonator with $\sim 30 - 40$ mW power coupled onto the waveguide (Figure 3.5a,b). Rayleigh scattering inside the resonator reflects $\sim 2\%$ of the power into the pumping laser. An Emcore Corp. DFB laser is used for pumping near 1559 nm and a PhotonX Inc. DFB laser is used for pumping near 1541 nm. Temperature tuning of the DFB lasers allows fine tuning control of the pumping wavelength for access to slightly anomalous, near-zero, and slightly normal dispersion wavelengths of the resonator. Figure 3.6a shows measurements of integrated dispersion of the resonator for pumping at specific wavelengths (provided in the legend) near 1559 nm. In the plots, $\mu = 0$ corresponds to the pump line. The dispersion curves are measured using a radio-frequency calibrated interferometer reference (Yi, Q.-F. Yang, K. Y. Yang, Suh, et al., 2015).

When pumped at near-zero dispersion, the comb spectral span is strongly influenced by comb radiation into a dispersive wave, which corresponds to cavity modes that are nearly resonant with comb lines. The mode number μ_{dw} of the dispersive wave is given as the solution to the equation (Z. Li, Xu, Coen, et al., 2020),

$$-\delta\omega + 2gP_0 + \delta\omega_{\text{rep}}\mu_{\text{dw}} = \frac{D_2}{2}\mu_{\text{dw}}^2 + \frac{D_3}{6}\mu_{\text{dw}}^3, \quad (3.16)$$

where $\delta\omega$ is the pump-laser cavity detuning as regulated by the self-injection feedback, g is Kerr nonlinear coefficient, P_0 is photon number of the pumped cavity resonance, $\delta\omega_{\text{rep}}$ is the difference between comb repetition rate and cavity free-spectral range (D_1), and D_2 and D_3 are second- and third-order dispersion parameters, respectively. Figure 3.6b gives the measured second-order dispersion (D_2) parameter at these same pumping wavelengths, and $D_3 = 7.5$ kHz is used for all pumping wavelengths. The left side of Equation 3.16 corresponds to the frequency comb lines and is plotted as the colored dashed lines in Figure 3.6a. In making these these line plots, $\delta\omega$ and $\delta\omega_{\text{rep}}$ are numerically simulated. The right side of Equation 3.16 is the integrated dispersion and fitted to the experimentally measured dispersion as noted above. At each pumping wavelength, the dispersive wave mode number μ_{dw} can be obtained as the intercept between the comb frequencies (dashed lines) and the corresponding integrated dispersion curve (solid lines).

The dispersive wave position is marked with an arrow in the left panel of Figure 3.6 c-f, which show measured spectra for SIL pumping at the wavelengths in Figure 3.6a. The arrow position provides a trend of measured comb span for negative mode numbers. Overall comb spectral span tends to be determined by this dispersive wave. Note that in Figure 3.6, the third dispersive wave (after mode number ~ 50) is absent in both the measured and simulated optical spectrum, which is a result of insufficient pump power. The comb spectrum in Figure 3.5d spans 9.9 nm (1.22 THz) and features on-chip comb-line power higher than $1 \mu\text{W}$, marked with arrows. This comb has superior spectral coverage compared to previous SIL operated normal GVD microcombs (W. Jin et al., 2021; Lihachev et al., 2022). It also features an increased number of comb lines compared with higher repetition rate non-bright combs directly III-V pumped with optical isolation (Shu et al., 2023). When pumped at 1541 nm near the other zero-dispersion wavelength, a microcomb spanning 9.2 nm (1.16 THz) is realized. The comb states both feature pump power conversion efficiency as high as 26%. These comb spectra are plotted in Figure 3.5d.

3.5 Imaging of mode-locked microcomb states

While the temporal envelope of pulses produced by normal GVD combs has been measured using cross-correlation (Xue, Xuan, et al., 2015), near-zero-GVD operation allows access to a wider variety of comb states including soliton molecules (bounded bright solitons) and switching waves (Garbin et al., 2017; Z. Li, Xu, Coen, et al., 2020). These interesting states have been analyzed numerically (Parra-Rivas, Damià Gomila, et al., 2014; Parra-Rivas, Damià Gomila, and Gelens, 2017; Anderson, Weng, et al., 2022), but they have so far not been observed in the time domain. This is result of current zero-dispersion systems being generated with a pulsed pump where the comb waveform is influenced by the pump pulse waveform or at challenging high repetition rates (Anderson, Leo, et al., 2016; S. Zhang, Bi, and Del'Haye, 2023; Xiao et al., 2021). Here, the linear optical sampling technique assisted with an electro-optic frequency comb is implemented to image the temporal profile of the various comb states (Yi, Q.-F. Yang, K. Y. Yang, and K. Vahala, 2018; H. Wang et al., 2022). The sampling EO comb spans ~ 5 nm with 33 lines, corresponding to a ~ 1.5 ps pulse in the time domain, and its repetition rate is set to be slightly higher than the zero-dispersion microcomb. Note that the temporal duration of the soliton pulse (for example, 2.6 ps FWHM in Figure 3.6d for the left pulse in measurement) is close to the pulse width of the EO-comb (~ 1.5 ps), thus the imaging result may not perfectly resolve fine structure in the temporal

waveforms. By combining the EO comb and the generated comb at the “drop” port, and detecting with a fast photodetector, the sampled microcomb signal is recorded by an oscilloscope for processing.

Experimental results are presented in the right panels of Figures 3.6c,d,e,f. At the anomalous side ($D_2 > 0$) of the near-zero GVD wavelength, the strong dispersive wave binds several solitons into soliton clusters, as observed in Figure 3.6c (right panel). The interference between the pulses creates the multiple fringes that are apparent in the optical spectrum (left panel). Numerically simulated time domain and spectra are also presented as dashed curves in Figure 3.6c,d,e,f. The clustered soliton formation is preserved for near-vanishing GVD ($D_2/2\pi = -1.5$ kHz) as shown in Figure 3.6d, where a soliton dimer is imaged. The corresponding optical spectrum is shown in the left panel of Figure 3.6d. For the pumping wavelength with normal dispersion, the resulting waveforms are often called switching waves or “platicons” (Lihachev et al., 2022; H. Wang et al., 2022). Here, the waveform evolves towards a square pulse as the dispersion becomes more normal ($D_2 < 0$) (Figure 3.6e-f, right panels). The present results experimentally demonstrate the evolution of comb states in the near zero GVD regime with different GVD sign, and are consistent with a previous numerical study (Anderson, Weng, et al., 2022).

Generally, operation of the comb with a small amount of normal dispersion (e.g. the state in Figure 3.6e, pumped at 1559.2 nm) provides both good spectral coverage as well as a temporal and spectral waveform that is more regular in shape. Furthermore, the square pulse nature of these states (apparent in Figure 3.6e-f, right panels) offers an increased duty cycle, which boosts comb power conversion efficiency. As a result, the microwave and optical performance of the comb state in Figure 3.6e is further studied and adapted for optical frequency division, as detailed in the last chapter.

3.6 Discussion and summary

We have demonstrated a microwave-rate mode-locked microcomb near zero GVD using a CMOS-ready coupled ring resonators. The reduced GVD enables broader microcomb operation using integrated photonics with high conversion efficiency, while maintaining the benefits of the self-injection feedback, including turnkey operation and optical linewidth reduction. A record number of comb lines is generated for non-amplified and non-pulse-pumped operation of a normal dispersion microcomb. The dispersion engineering scheme in this paper can be extended to

other wavelengths and different photonic platforms.

The results reported here are lately used in a two-point optical frequency division system (Kudelin et al., 2024; Ji, W. Zhang, et al., 2024) for low-noise microwave synthesis, as mentioned in chapter 2.

Repeatability of the dispersion engineering among different devices

Besides, the dispersion curves are observed to be very repeatable between the different devices, while the zero-GVD wavelengths vary between different devices. This is because the envelope depends on the FSR ratio of the two rings which to be 1.005. This ratio corresponds to a 50 μm difference in roundtrip lengths of ring A and ring B, which is extremely well controlled by the sub-micron lithographic precision.

On the other hand, the mode degenerate wavelength λ_0 is determined by the vernier matching condition that $\lambda_0 = \frac{n_{\text{eff,A}}L_A}{m_A} = \frac{n_{\text{eff,B}}L_B}{m_B}$, where $n_{\text{eff,A}}$ and $n_{\text{eff,B}}$ are effective mode index of the two rings, respectively, m_A and m_B are integers. Here $n_{\text{eff,A}}$ and $n_{\text{eff,B}}$ can vary in two ways: (1) from chip-to-chip as a result of SiN layer thickness variation, and (2) from device-to-device on the same chip as a result of slight fabrication errors that produce variations in local dimensions. The latter of these variations is expected to be much smaller. The above two kinds of fabrication imperfection influence the λ_0 in two ways. (1) Suppose that $n_{\text{eff,A}}$ and $n_{\text{eff,B}}$ are simultaneously perturbed by Δn where $n_{\text{eff,A}} \approx n_{\text{eff,B}} \equiv n_{\text{eff}}$, then $\Delta\lambda_0 = \lambda_0\Delta n/n_{\text{eff}}$. With a realistic $\Delta n/n_{\text{eff}} = 0.01$, $\Delta\lambda_0 \approx 16$ nm. (2) Suppose that $n_{\text{eff,B}}$ is perturbed by $\Delta n_{\text{eff,B}}$ while $n_{\text{eff,A}}$ is not changed, while the mode number for λ_0 is accordingly changed by Δm , such that $n_{\text{eff,A}}/(m_A + \Delta m) = (n_{\text{eff,B}} + \Delta n_{\text{eff,B}})/(m_B + \Delta m)$. Δm ($\Delta\lambda_0$) is then given by,

$$\frac{\Delta\lambda_0}{\lambda_0} = -\frac{\Delta m}{m_B} = -\frac{n_{\text{eff,B}}}{n_{\text{eff,A}} - n_{\text{eff,B}}} \frac{\Delta n_{\text{eff,B}}}{n_{\text{eff,B}}} = -200 \frac{\Delta n_{\text{eff,B}}}{n_{\text{eff,B}}}. \quad (3.17)$$

As a result, when the effective index of the waveguides is separately perturbed by fabrication errors, the change in the degenerate wavelength is magnified by 200 times compared with a single ring case (due to the vernier effect). The above two effects both contribute uncertainty in degenerate wavelength λ_0 . Since the zero-GVD wavelength shifts with the degenerate wavelength λ_0 , it is also less controlled. This inconvenience is lately overcome (or even upgraded) via the differential heater tuning method, as detailed in the next chapter.

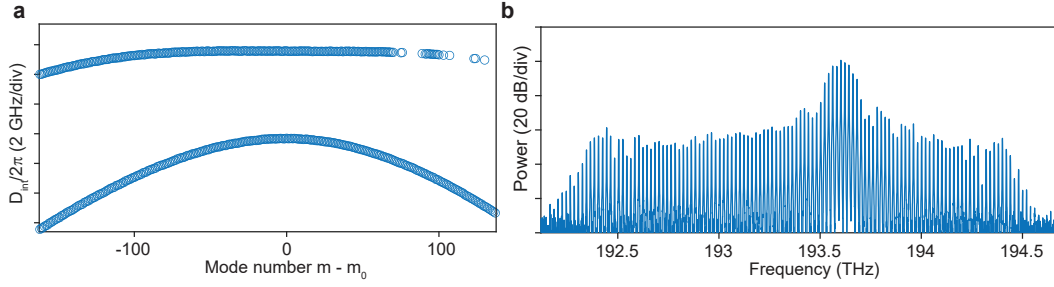


Figure 3.7: **Dispersion and microcomb generation of the 2CR device with optimized ϵ .** **a**, The measured integrated dispersion is plotted versus mode number. **b**, Experimentally measured microcomb spectrum under laser SIL.

The optimum parameters for near-zero-GVD microcomb operation

The parameters $g_{co}L_{co}$ and ϵ used in Section 3.2 are not optimized for dispersion cancellation over a broad bandwidth for microcomb generation. In an ideal scenario, the mode-coupling-induced group velocity dispersion (GVD) should exactly cancel the intrinsic second-order dispersion of the waveguide, $D_{20}/2\pi = -284$ kHz. Under this condition, the third-order dispersion D_3 also vanishes.

The optimal value of ϵ can be analytically derived. The free spectral range (FSR) of the hybridized supermodes $\omega_{m,\pm}$ is obtained by differentiating with respect to the mode index m :

$$FSR_{m,\pm} = FSR_m \pm \overline{FSR} \frac{\cos(g_{co}L_{co}) \sin(2\pi\epsilon m)}{\sqrt{1 - \cos^2(g_{co}L_{co}) \cos^2(2\pi\epsilon m)}}, \quad (3.18)$$

where $FSR_m = (\partial\omega_{m,\pm}/\partial m)/2\pi$ is the baseline FSR, and the dispersion of the coupling coefficient ($\partial g_{co}/\partial m$) is neglected for simplicity.

The corresponding second-order dispersion parameter $D_{2,\pm}$ can be evaluated as:

$$D_{2,\pm} - D_{20} = \pm \overline{D_1} \times \frac{2\pi\epsilon^2 \cos(g_{co}L_{co}) \sin^2(g_{co}L_{co}) \cos(2\pi\epsilon m)}{[1 - \cos^2(g_{co}L_{co}) \cos^2(2\pi\epsilon m)]^{3/2}} \equiv D_{2c,\pm}. \quad (3.19)$$

Optimal dispersion cancellation is achieved when $D_{2,+} = 0$ at the dispersion center, corresponding to $\cos(2\pi\epsilon m) = 1$. This yields the condition:

$$2\pi\epsilon^2 \tan^{-1}(g_{co}L_{co}) = -D_{20}.$$

Substituting $g_{co}L_{co} = 0.954$ results in an optimum ϵ of 0.0016, corresponding to a 60 MHz FSR difference between the two rings near the average FSR of 19.95 GHz.

To accommodate fabrication variability, three sets of devices were fabricated with FSR differences of 50 MHz, 60 MHz, and 70 MHz (tape-out is by Joel Guo). In

this batch, the actual measured $g_{\text{co}}L_{\text{co}}$ was 0.917. The best dispersion flattening was observed in the device with a 70 MHz *FSR* difference ($\epsilon = 0.00175$), shown in Figure 3.7a. A flat dispersion profile spanning more than 100 modes (>2 THz) was measured. As shown in Figure 3.7b, the resulting microcomb also spans over 2 THz. This is significantly broader than the 1 THz span achieved under self-injection locking (SIL) conditions using the same pump power (Figure 3.5).

References

- Anderson, Miles H., Francois Leo, et al. (2016). “Measurement of the Raman self-frequency shift of a temporal cavity soliton.” In: *Nonlinear Photonics*. OSA, NW4A–4.
- Anderson, Miles H., Wenle Weng, et al. (2022). “Zero dispersion Kerr solitons in optical microresonators.” In: *Nature Communications* 13.1, p. 4764.
- Boeck, Robi et al. (2010). “Series-coupled silicon racetrack resonators and the Vernier effect: theory and measurement.” In: *Optics Express* 18.24, pp. 25151–25157.
- Diddams, Scott A., Kerry J. Vahala, and Thomas Udem (2020). “Optical frequency combs: coherently uniting the electromagnetic spectrum.” In: *Science* 369.6501, eaay3676.
- Fülöp, Attila et al. (2018). “High-order coherent communications using mode-locked dark-pulse Kerr combs from microresonators.” In: *Nature Communications* 9.1, pp. 1–8.
- Garbin, Bruno et al. (2017). “Experimental and numerical investigations of switching wave dynamics in a normally dispersive fibre ring resonator.” In: *The European Physical Journal D* 71, pp. 1–8.
- Grudinin, Ivan S. et al. (2010). “Phonon laser action in a tunable two-level system.” In: *Physical Review Letters* 104.8, p. 083901.
- Helgason, Óskar B., Francisco R. Arteaga-Sierra, et al. (2021). “Dissipative solitons in photonic molecules.” In: *Nature Photonics* 15.4, pp. 305–310.
- Helgason, Óskar B., Marcello Girardi, et al. (2023). “Surpassing the nonlinear conversion efficiency of soliton microcombs.” In: *Nature Photonics* 17.11, pp. 992–999.
- Herr, Tobias et al. (2014). “Mode spectrum and temporal soliton formation in optical microresonators.” In: *Physical Review Letters* 113.12, p. 123901.
- Ji, Qing-Xin, Warren Jin, et al. (2023). “Engineered zero-dispersion microcombs using CMOS-ready photonics.” In: *Optica* 10.2, pp. 279–285.

- Ji, Qing-Xin, Wei Zhang, et al. (2024). “Coherent optical-to-microwave link using an integrated microcomb.” In: *IEEE Journal of Selected Topics in Quantum Electronics*.
- Jin, Warren (2022). *Ultra-Low-Loss Silicon Nitride Photonic Integrated Circuits for Highly Coherent Lasers*. University of California, Santa Barbara.
- Jin, Warren et al. (2021). “Hertz-linewidth semiconductor lasers using CMOS-ready ultra-high-Q microresonators.” In: *Nature Photonics* 15.5, pp. 346–353.
- Kim, Sangsik et al. (2017). “Dispersion engineering and frequency comb generation in thin silicon nitride concentric microresonators.” In: *Nature Communications* 8.1, p. 372.
- Kippenberg, Tobias J. et al. (2018). “Dissipative Kerr solitons in optical microresonators.” In: *Science* 361.6402, eaan8083.
- Kondratiev, Nikita M. et al. (2017). “Self-injection locking of a laser diode to a high-Q WGM microresonator.” In: *Opt. Express* 25.23, pp. 28167–28178.
- Kudelin, Igor et al. (2024). “Photonic chip-based low-noise microwave oscillator.” In: *Nature* 627.8004, pp. 534–539.
- Li, Jiang et al. (2014). “Electro-optical frequency division and stable microwave synthesis.” In: *Science* 345.6194, pp. 309–313.
- Li, Zongda, Yiqing Xu, Stéphane Coen, et al. (2020). “Experimental observations of bright dissipative cavity solitons and their collapsed snaking in a Kerr resonator with normal dispersion driving.” In: *Optica* 7.9, pp. 1195–1203.
- Li, Zongda, Yiqing Xu, Caleb Todd, et al. (2021). “Observations of existence and instability dynamics of near-zero-dispersion temporal Kerr cavity solitons.” In: *Physical Review Research* 3.4, p. 043207.
- Liang, Wei et al. (2015). “High spectral purity Kerr frequency comb radio frequency photonic oscillator.” In: *Nature Communications* 6, p. 7957.
- Lihachev, Grigory V. et al. (2022). “Platicon microcomb generation using laser self-injection locking.” In: *Nature Communications* 13.1, p. 1771.
- Liu, Junqiu et al. (2020). “Photonic microwave generation in the X-and K-band using integrated soliton microcombs.” In: *Nature Photonics* 14.8, pp. 486–491.
- Papp, Scott B. et al. (2014). “Microresonator frequency comb optical clock.” In: *Optica* 1.1, pp. 10–14.
- Parra-Rivas, Pedro, Damia Gomila, and Lendert Gelens (2017). “Coexistence of stable dark-and bright-soliton Kerr combs in normal-dispersion resonators.” In: *Physical Review A* 95.5, p. 053863.
- Parra-Rivas, Pedro, Damià Gomila, et al. (2014). “Third-order chromatic dispersion stabilizes Kerr frequency combs.” In: *Optics Letters* 39.10, pp. 2971–2974.

- Pavlov, Nikolay G. et al. (2017). “Soliton dual frequency combs in crystalline microresonators.” In: *Optics Letters* 42.3, pp. 514–517.
- Peng, Bo et al. (2014). “Parity–time–symmetric whispering-gallery microcavities.” In: *Nature Physics* 10.5, pp. 394–398.
- Shen, Boqiang et al. (2020). “Integrated turnkey soliton microcombs.” In: *Nature* 582.7812, pp. 365–369.
- Shu, Haowen et al. (2023). “Submilliwatt, widely tunable coherent microcomb generation with feedback-free operation.” In: *Advanced Photonics* 5.3, pp. 036007–036007.
- Stern, Brian et al. (2018). “Battery-operated integrated frequency comb generator.” In: *Nature* 562.7727, p. 401.
- Suh, Myoung-Gyun and Kerry Vahala (2018). “Gigahertz-repetition-rate soliton microcombs.” In: *Optica* 5.1, pp. 65–66.
- Tikan, Alexey et al. (2022). “Protected generation of dissipative Kerr solitons in supermodes of coupled optical microresonators.” In: *Science Advances* 8.13, eabm6982.
- Wang, Heming et al. (2022). “Self-regulating soliton switching waves in microresonators.” In: *Physical Review A* 106.5, p. 053508.
- Xiang, Chao et al. (2021). “Laser soliton microcombs heterogeneously integrated on silicon.” In: *Science* 373.6550, pp. 99–103.
- Xiao, Zeyu et al. (2021). “Zero-dispersion soliton generation in a high-Q fiber Fabry-Pérot microresonator.” In: *CLEO: Science and Innovations*. Optica Publishing Group, SW2H–6.
- Xue, Xiaoxiao, Yi Xuan, et al. (2015). “Mode-locked dark pulse Kerr combs in normal-dispersion microresonators.” In: *Nature Photonics* 9.9, pp. 594–600.
- Xue, Xiaoxiao, Xiaoping Zheng, and Bingkun Zhou (2019). “Super-efficient temporal solitons in mutually coupled optical cavities.” In: *Nature Photonics* 13.9, pp. 616–622.
- Yang, Ki Youl et al. (2018). “Bridging ultrahigh-Q devices and photonic circuits.” In: *Nature Photonics* 12.5, p. 297.
- Yariv, Amnon et al. (1999). “Coupled-resonator optical waveguide: a proposal and analysis.” In: *Optics Letters* 24.11, pp. 711–713.
- Yi, Xu, Qi-Fan Yang, Ki Youl Yang, Myoung-Gyun Suh, et al. (2015). “Soliton frequency comb at microwave rates in a high-Q silica microresonator.” In: *Optica* 2.12, pp. 1078–1085.
- Yi, Xu, Qi-Fan Yang, Ki Youl Yang, and Kerry Vahala (2018). “Imaging soliton dynamics in optical microcavities.” In: *Nature Communications* 9.1, pp. 1–8.

- Yuan, Zhiquan et al. (2023). “Soliton pulse pairs at multiple colours in normal dispersion microresonators.” In: *Nature Photonics* 17.11, pp. 977–983.
- Zhang, Shuangyou, Toby Bi, and Pascal Del’Haye (2023). “Quintic dispersion soliton frequency combs in a microresonator.” In: *Laser & Photonics Reviews* 17.10, p. 2300075.

DISPERSION TUNING OF THE COUPLED-RING RESONATOR AND MULTI-MODALITY OPERATION

The motivation of the work in this chapter originates from the problem that the zero-GVD wavelengths of the 2CR devices in the previous chapter are not well-controlled. With this, screening a number of devices is necessary to find the one with correct operation wavelength. The Vernier differential tuning of the 2CR device was originally conceived to solve this problem, and consequently the operation wavelength can be conveniently re-located for the near-zero-GVD microcomb operation. The tuning was lately found so simple but powerful, and combined with the high- Q property of the ultra-low-loss Si_3N_4 platform, Brillouin laser, bright soliton microcomb, and dark-pulse microcomb can be demonstrated using the same device under a III-V laser direct pump. This ability, referred to as “multi-modality” operation, is unprecedented in integrated photonics and found interesting by journal referees (Ji, P. Liu, et al., 2024).

4.1 Theory of Moiré-enhanced dispersion tuning

In this section, we discuss the theory that describes the Moiré-speedup of the dispersion spectrum when the two rings are differentially tuned. Calculation of the dispersion in the Vernier-coupled ring resonators is detailed in (Yuan, Gao, et al., 2023) (also in Chapter 2 of this thesis). Briefly, a transfer matrix, T , is used to propagate a 2-component wave function through a round trip,

$$T = e^{i\omega_{\pm}\bar{L}/c} \begin{pmatrix} e^{-i\omega\Delta L/c} \cos(g_{\text{co}}L_{\text{co}}) & i \sin(g_{\text{co}}L_{\text{co}}) \\ i \sin(g_{\text{co}}L_{\text{co}}) & e^{i\omega\Delta L/c} \cos(g_{\text{co}}L_{\text{co}}) \end{pmatrix}. \quad (4.1)$$

The resulting secular equation gives the eigenfrequencies, $\omega_{m,\pm}$, of the two mode families (see plots in Figure 4.3B and Figure 4.3C),

$$\omega_{m,\pm} - \omega_m = \pm \frac{D_{1,m}}{2\pi} \arccos [\cos(g_{\text{co}}L_{\text{co}}) \cos(2\pi\epsilon m)] \equiv D_{\text{int},c}, \quad (4.2)$$

where m is mode number, $\epsilon = \Delta L/\bar{L}$ is the optical path length contrast of the rings ($\bar{L} \equiv (n_{\text{wg},A}l_A + n_{\text{wg},B}l_B)/2$ is the averaged optical path length of the two rings, and $\Delta L \equiv (n_{\text{wg},A}l_A - n_{\text{wg},B}l_B)/2$), g_{co} is the coupling strength per unit length, L_{co} is the length of the coupling section, $\omega_m = 2\pi mc/\bar{L}$ with c the speed of light in vacuum,

and $D_{1,m} \equiv \partial\omega_m/\partial m$. The coupling strength $g_{\text{co}}L_{\text{co}}$ has a weak dependence on m (and wavelength), decreasing by 4.1% per 1 THz towards higher optical frequencies in the current design. This results from the wavelength dependence of the evanescent field coupling between the two rings.

Free spectral range $FSR_{m,\pm}$ of the two bands is obtained by calculating derivative of $\omega_{m,\pm}$ with respect to m :

$$FSR_{m,\pm} = FSR_m \pm \epsilon FSR_0 \frac{\cos(g_{\text{co}}L_{\text{co}}) \sin(2\pi\epsilon m)}{\sqrt{1 - \cos^2(g_{\text{co}}L_{\text{co}}) \cos^2(2\pi\epsilon m)}}, \quad (4.3)$$

where dispersion of the mode coupling strength $\partial g_{\text{co}}/\partial m$ is neglected in the calculation, and where $FSR_m = D_{1,m}/2\pi$ and $FSR_0 = c/\bar{L} = \bar{D}_1/2\pi$. The group velocity dispersion parameter $D_{2,c}$ (as plotted in Figure 4.4C) is obtained by calculating the derivative of $FSR_{m,\pm}$ with respect to m ,

$$D_{2,m,\pm} - D_{2,o} \approx \pm D_1 \frac{-2\pi\epsilon^2 \cos(g_{\text{co}}L_{\text{co}}) \sin^2(g_{\text{co}}L_{\text{co}}) \cos(2\pi\epsilon m)}{[1 - \cos^2(g_{\text{co}}L_{\text{co}}) \cos^2(2\pi\epsilon m)]^{3/2}} \equiv D_{2,c}, \quad (4.4)$$

where again $\partial g_{\text{co}}/\partial m$ is neglected, and $D_{2,o}/2\pi = \partial FSR_m/\partial m$ is the GVD parameter of the uncoupled resonator waveguide. The r.h.s. of Eqn. (4.4) vanishes when $2\epsilon m = N + \frac{1}{2}$ where N is an integer.

Equation (4.4) also predicts the accessible dispersion regime when the two rings are differentially tuned,

$$|D_{2,c}| \equiv |D_{2,m,\pm} - D_{2,o}| \leq 2\pi\epsilon^2 \bar{D}_1 \cot(g_{\text{co}}L_{\text{co}}). \quad (4.5)$$

The r.h.s. of Eqn. (4.5) corresponds to the shaded orange area in Figure 4.4C.

Note that $2\epsilon m = N$ (where N is an integer) corresponds to the mode numbers m where the ring frequencies overlap and hybridize. The broadband nature of the Moiré pattern modulation results from the separation of these mode numbers ($\Delta m \sim 1/\epsilon$) being large. In the present system $\Delta m = 200$. Also, note that $2\epsilon m = N + 1/2$ corresponds to frequencies where mode resonances in the two rings interleave. Differential temperature tuning varies ϵ , thereby shifting the mode number locations where strong hybridization occurs (as well as the overall Moiré pattern). To calculate the corresponding shift in frequency, consider the change δf_o in optical frequency at a given overlap frequency f_o (or an interleave frequency) as given by,

$$\frac{\delta f_o}{f_o} = \frac{\delta m}{m} = -\frac{\delta \epsilon}{\epsilon} = -\frac{1}{2\epsilon} \frac{\delta(L_A - L_B)}{\bar{L}} \equiv -R \frac{\delta(L_A - L_B)}{\bar{L}}, \quad (4.6)$$

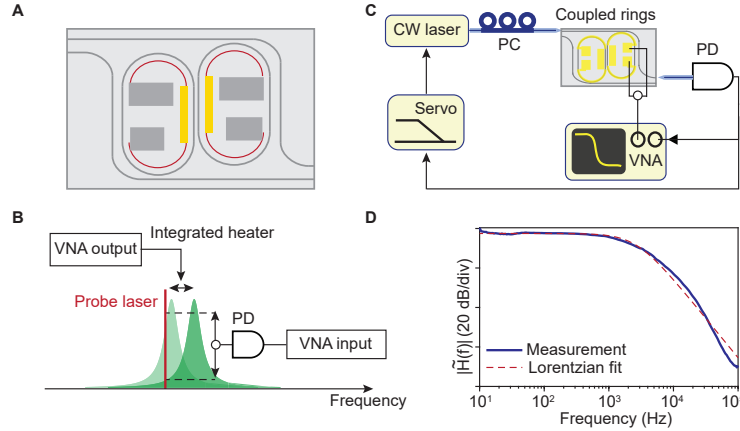


Figure 4.1: **Differential temperature tuning using integrated heaters.** (A), Details of the heater routing. The electrodes (gray rectangles) are wire bonded to an external circuit board to apply the heating current. Heaters (red) are located at the arcs of the racetrack and are electrically connected with a wider electrical trace (yellow). The wider trace has less electrical resistance and thus reduces the heating effect at the coupling section of the two rings. This design improves the differential thermal tuning efficiency. All three parts (red, yellow and gray) are deposited with the same Pt layer thickness. (B), Principle of integrated heater frequency response characterization. (C), Heater frequency response characterization setup. (D), Measured frequency response of the heater transfer function. The dashed line is a Lorentzian fitting where the 6 dB bandwidth is 2.67 ± 0.05 kHz.

where $R \equiv 1/(2\epsilon)$ is the Vernier ratio. A simple relation between the differential ring tuning $\delta(L_A - L_B)$ and tuning of the dispersion spectrum δf_o is thus established. On the other hand, the mode resonance tuning of a single ring via optical path length change is given by,

$$\frac{\delta f}{f} = -\frac{\delta L}{L}, \quad (4.7)$$

from which it follows that the Vernier tuning scheme enhances the tuning rate by a factor of R . This is also the speedup factor of the Moiré pattern (Gabrielyan, 2007).

4.2 Differential temperature tuning control

A pair of metallic resistance heaters (platinum with titanium as an adhesion layer) are deposited using Ebeam evaporation and liftoff. As shown in Figure 4.2C, the metal is offset from the SiN waveguides by $8 \mu\text{m}$ to avoid metal-induced optical absorption. To suppress cross-talk heating is minimized near the coupling section between the two rings as described in Figure 4.1A. The heaters are wire-bonded to a printed circuit board to apply direct-current voltages. The chip is attached to a copper submount using thermal-conductive epoxy. A thermistor and a ceramic

heater are used in combination with a PID control loop to stabilize temperature within < 1 mK error, while ~ 10 mK temperature variation is generally allowed for the device operation. The metallic heaters are used for differential tuning. The common temperature is varied using the ceramic heater.

The frequency response of the metallic heater tuners was also measured. The principle of the measurement approach is shown in Figure 4.1B. A single frequency probe laser (red line) is tuned into a mode resonance of the coupled rings. One of the heaters is then modulated by a vector network analyzer (VNA) which causes modulation of the mode resonant frequency. The laser's frequency is fixed so that the thermal-induced mode resonance modulation is transferred as modulation of transmitted laser power on the bus waveguide. The modulated power is monitored by a photodetector and measured by the VNA to determine the frequency response $|\tilde{H}(f)|$.

The experimental setup is shown in Figure 4.1C. A CW Toptica ECDL is coupled into the bus waveguide using a lensed fiber, and the power transmission signal is collected by a Newport 1811 photodetector. The laser is loosely stabilized (feedback bandwidth < 10 Hz) to the cavity resonance by locking to a certain transmitted power. The measured $|\tilde{H}(f)|$ is given in Figure 4.1D where the 6 dB bandwidth is 2.67 ± 0.05 kHz, when fitted by a Lorentzian response (Panuski, Englund, and Hamerly, 2020).

4.3 Multi-modality operation

The Vernier effect, used in measurement instruments such as calipers and micrometers, overlays two scales or rulings with slightly different divisions to improve accuracy. Its analog in optical resonators overlays two frequency scales with different divisions set by the free spectral range, FSR , of two resonators. The coupling of such resonators is mediated by the frequency Vernier and creates useful tuning effects that benefit optical add-drop filters (Little et al., 1997), semiconductor lasers (Hulme, Doylend, and John E. Bowers, 2013), and frequency microcombs (Xue, Xuan, P.-H. Wang, et al., 2015; Helgason, Arteaga-Sierra, et al., 2021; Okawachi et al., 2022; Helgason, Girardi, et al., 2023; Ji, W. Jin, et al., 2023; Yuan, Gao, et al., 2023). Verniers feature a larger scale periodicity associated with the Moiré pattern (Oster and Nishijima, 1963) they form when overlaid. And this Moiré pattern exhibits a speedup effect when either scale in the Vernier is shifted. That is, when the two sets of scales are displaced differentially, the collective movement of the

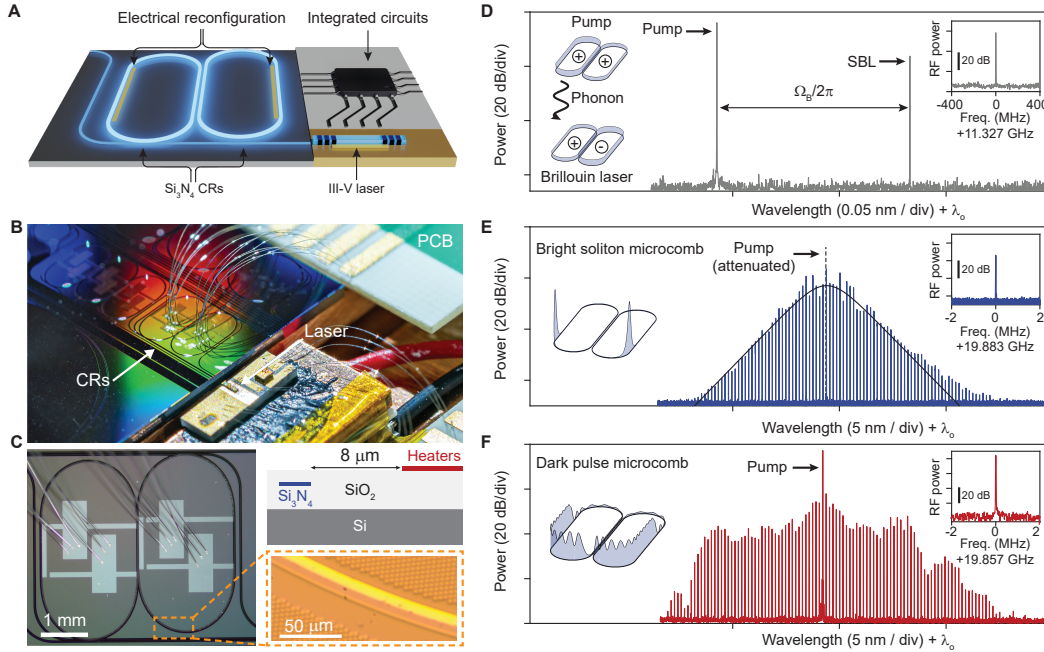


Figure 4.2: **A hybridly integrated microresonator and optical pump can be operated as a Brillouin laser, bright microcomb, or dark pulse microcomb source with on-demand electrical control and at a user-defined wavelength across C-band.** (A), Illustration of the reconfigurable hybridly integrated device. Si_3N_4 coupled rings (CRs) are directly pumped by an integrated III-V laser. Dispersion of the CRs is tuned by differential tuning of the rings using integrated resistive heaters. The III-V laser and the heaters are wire-bonded to printed circuit boards for electrical control. (B), Photograph of the integrated device depicted in panel A. (C), Zoom-in image of the coupled racetrack ring resonator. Resistive heaters are deposited atop the chip and offset from the Si_3N_4 waveguide by $8\ \mu\text{m}$ to avoid metal-induced optical absorption. (D-F), Optical spectra for on-demand operation of the Brillouin laser (panel D), bright microcomb (panel E) and dark pulse microcomb (panel F), all operated at the same III-V laser pumping wavelength $\lambda_0=1548.4\ \text{nm}$ per the system layout in panel B. In each case, dispersion is reconfigured via simple electrical tuning. In panel E the black curve denotes the sech^2 envelope and gives an optical pulse width of 800 fs. **Left insets:** schematic drawings of Brillouin emission between symmetric and antisymmetric hybrid modes (panel D) and pulse shape temporal waveforms inside the coupled rings (panels E and F). **Right insets:** RF beatnote (panel D) between the pump laser and Brillouin laser (resolution bandwidth is 100 kHz). Repetition rate tone (panels E, F) confirming mode locking (resolution bandwidth is 10 kHz).

Moirépattern is multiplied by the Vernier ratio (R) (Gabrielyan, 2007; Oster and Nishijima, 1963). Here, the speedup effect is adapted to demonstrate broadband electrical control (via differential thermal tuning) of dispersion.

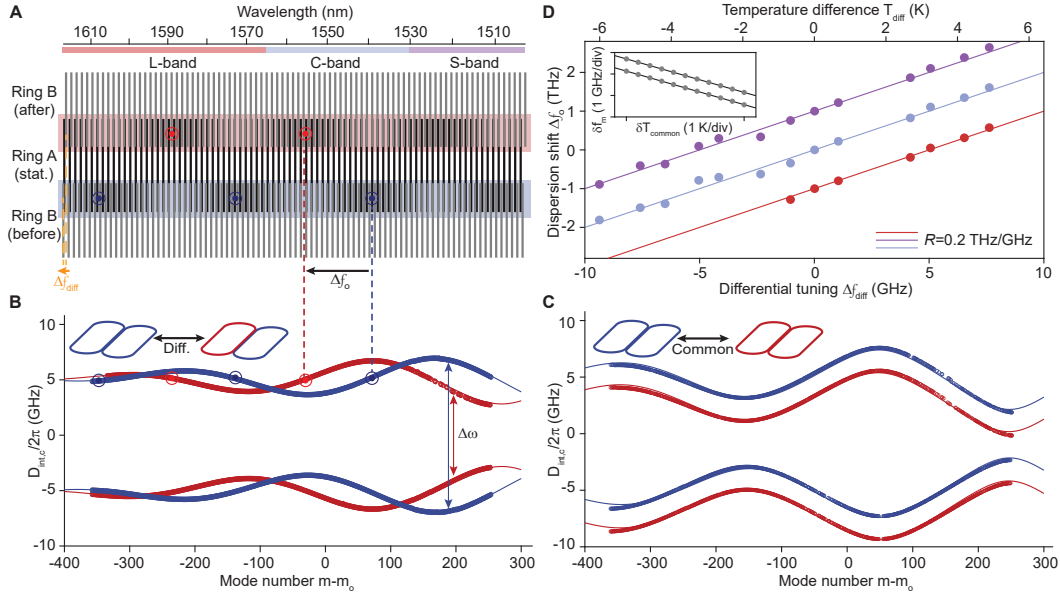


Figure 4.3: Measurement of Moiré speedup of the dispersion spectrum. (A), Illustration of the Moiré pattern formed by mode frequencies in ring A and ring B resonators. A large shift Δf_0 of Moiré pattern is caused by a small uniform shift Δf_{diff} of the ring B frequencies. Brighter regions in the pattern correspond to degeneracy of the local ring modes and lead to strong modal hybridization. Here ring A is assumed stationary (stat.), while ring B is tuned and illustrated before and after the differential tuning. (B), Each color shows the measured (bold) and fitted (fine solid line) dispersion spectra for the two frequency bands of the system. Mode number $m_0 = 0$ corresponds to 1550 nm. The red spectra result from differential heating. (C), Dispersion tuning for non-differential heating (i.e., common mode tuning) by 10 K (blue and red). No dispersion change is observed and the curves have been intentionally offset by 2 GHz for comparison. (D), Measurement of the Moiré speedup effect wherein dispersion tuning of the circled dots in panel (A) are measured versus differential heating. Solid lines give a linear fit with Vernier ratio $R = 0.2$ THz/GHz. The three colors correspond to different reference points when evaluating the dispersion tuning, as illustrated in panel (A): S band (light purple), C band (light blue) and L band (light red). Inset: calibration of mode resonant frequency shift versus chip temperature: $\delta f_m / \delta T_{\text{common}} = 1.561 \pm 0.003$ GHz/K (upper band) and 1.558 ± 0.001 GHz/K (lower band).

Generally, anomalous dispersion is necessary for mode-locking of bright soliton microcombs (Herr et al., 2014), which feature a femtosecond timescale optical pulse and find applications in various fields such as LiDAR (Suh and Vahala, 2018; Trocha et al., 2018), dual comb spectroscopy (Suh, Q.-F. Yang, et al., 2016; Bao et al., 2021), optical frequency synthesis (Spencer et al., 2018), optical clocks (Newman et al., 2019), and astrocombs (Suh, Yi, et al., 2019; Obrzud et al., 2019).

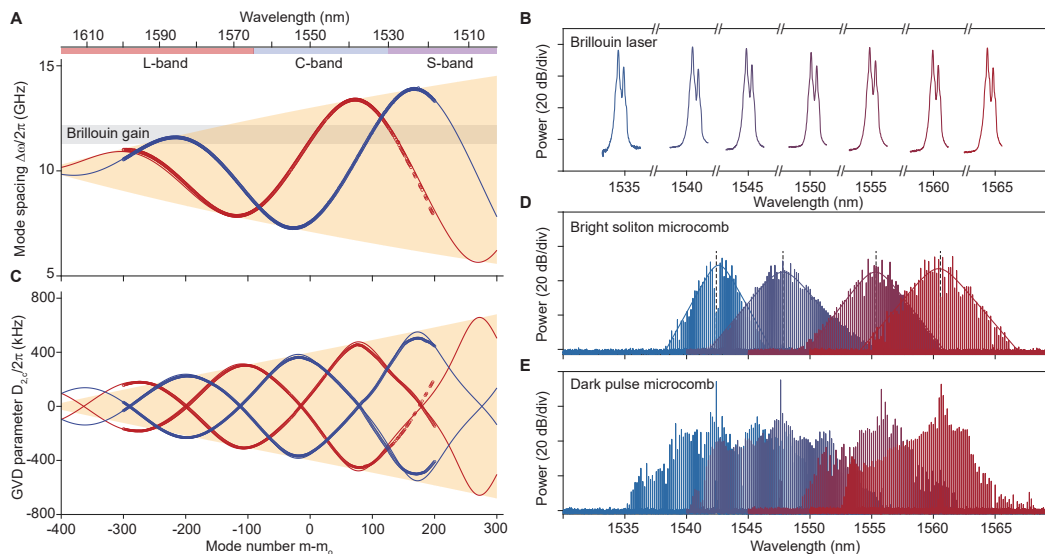


Figure 4.4: Broadband operation of the Brillouin laser, bright soliton microcomb and dark pulse microcomb. (A), Broadband tuning of the Brillouin phase matching condition across the optical C band and partial S, L bands. Frequency spacing between the upper and lower bands in Figure 2 is plotted versus relative mode number (upper scale: wavelength) for two different T_{diff} . Red and blue curves are data (bold curve) and model (fine curve). The orange region gives the accessible mode frequency spacing. The gray area denotes the approximate frequencies where Brillouin gain is possible. (B), Experimental demonstration of reconfigured Brillouin lasing across the optical C band. (C), Reconfiguration of group velocity dispersion (GVD) for bright soliton and dark pulse generation. The fitted GVD parameter D_{2c} at two different T_{diff} is plotted versus mode number (upper scale: wavelength). Red and blue curves are data fit (dots) and model (fine curve). The orange region gives the theoretically accessible D_{2c} values. The discontinuity of the red dots at large mode numbers is due to the insufficient bus-ring coupling at shorter wavelengths, making it challenging to capture and analyze these mode resonances. (D-E), Experimental demonstration of reconfigured bright soliton microcomb (D) and dark pulse microcomb (E) under DFB laser self-injection-locked operation at four different wavelengths. Mode locking is confirmed by the high signal-to-noise ratio photodetected repetition rate tone.

On the other hand, normal dispersion microcombs (Xue, Xuan, Y. Liu, et al., 2015), while having narrower spectral coverage compared to bright microcombs, offer higher power efficiency and comb line power. These properties are advantageous for applications like microwave generation via photodetection (Kudelin et al., 2024) and WDM-based coherent optical communications (Fülöp et al., 2018; Shu et al., 2022). Finally, Brillouin lasers are known for their high spectral coherence (J. Li, H. Lee, T. Chen, et al., 2012; Gundavarapu et al., 2019) that is useful in applications including microwave signal generation (J. Li, H. Lee, and Vahala, 2013), gyroscopes (Yu-Hung Lai et al., 2020) and clock signal sources (Loh et al., 2020). However, they require precise phase matching for operation, and this involves setting the frequency difference between two optical resonances to closely match the phonon frequency shift. The phase matching condition is normally set during device fabrication by adjusting the device FSR (i.e., device diameter). And, in effect, this permanently fixes the pump wavelength (i.e., each device has a set pumping wavelength). As now shown, on-demand operation across C-band is possible for each of these three modes of operation.

Hybrid integration of the coupled ring chip and III-V laser pump

Our prototype device consists of a pair of coupled, single-mode Si_3N_4 racetrack-shaped ring resonators with metallic heaters deposited along their periphery and wire-bonded to a printed circuit board (PCB) for electrical control (Figure 4.2A-C). The intrinsic Q factor is 95 million, the average FSR of the two rings is 19.95 GHz and their FSR difference is $\delta FSR = 100$ MHz so that $R \approx FSR/\delta FSR = 200$. The rings couple along a straight section to form hybrid mode frequency bands (Ji, W. Jin, et al., 2023; Yuan, Gao, et al., 2023) whose dispersion spectra are modulated by the Moiré effect. And by applying voltage to one of the ring heaters, the frequency ruling of the corresponding resonator is shifted, thereby inducing a much larger spectral shift of the dispersion through the speedup effect. Large changes in dispersion over frequency spans in excess of the telecom C-band are possible, so that a single device can be reconfigured on-demand for operation in several different modalities.

To illustrate, Figure 4.2D,E,F show respectively the spectra from a single device operated as a stimulated Brillouin laser (SBL), a bright pulse microcomb, and a dark pulse microcomb. Each of these operational modes was set by differential tuning of the resonators. The beatnote between the pump laser and SBL, as well as the repetition rates for the microcombs are photodetected and their coherent electrical spectra are shown in the insets. Moreover, on account of the high optical

Q of the coupled rings, and correspondingly low turn-on power of these devices, direct pumping from the same semiconductor laser is possible in a hybrid-integrated design (see Figure 4.2B).

Real-time switching between a bright soliton and a dark pulse microcomb state

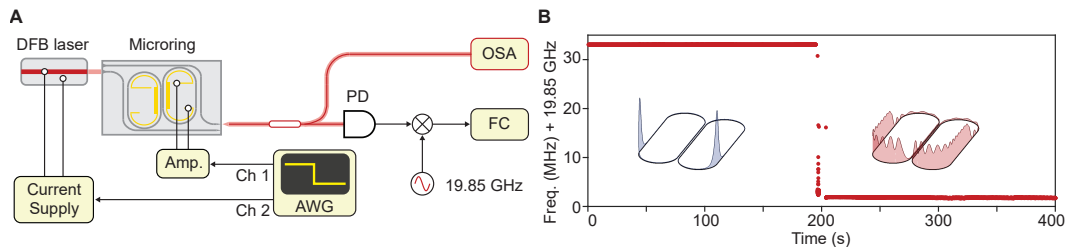


Figure 4.5: **Real time switching between a bright pulse microcomb and a dark pulse microcomb.** (A), Experimental setup. (B), Measured repetition rate when the microcomb is switched from a bright pulse microcomb to a dark pulse microcomb.

A measurement of real-time switching between a bright soliton and dark pulse microcomb state is presented in Figure 4.5. As an aside, because there is no optical isolation or amplification of the pumping lasers in these measurements, the setup is both suitable for integration and also operates in the self-injection locking (turnkey) mode (Pavlov et al., 2018; Boqiang Shen et al., 2020).

In this measurement, a DFB laser (at around 1548 nm) is self-injection locked to the coupled rings. Switching is induced with an arbitrary waveform generator (AWG) whose output was amplified by an electrical waveform amplifier (Amp.) to drive the heaters for differential thermal tuning. Current applied on the DFB laser is simultaneously switched to maintain the self-injection lock. Microcomb states are monitored using an optical spectrum analyzer (OSA), while the repetition rate tone is mixed down by a local microwave synthesizer near the repetition rate, and then monitored in real time using a frequency counter (FC). As noted in Figure 4.2E and Figure 4.2F, the repetition rate frequency of the bright soliton microcomb is slightly higher than the dark pulse microcomb (also noted in Figure 4.2E-F). The measurement results are shown in Figure 4.5B. In this measurement, the bright soliton state stays stationary for 200 seconds, at which time the microcomb state is switched. A dark pulse microcomb state emerges in seconds and remains stationary afterwards for another 200 seconds.

Dispersion tuning results

The Moiré speedup effect is depicted in Figure 4.3A where the mode frequencies within two resonators (ring A and B) are depicted as black lines. The line spacing, corresponding to the $FSRs$ are assumed to be slightly different, and their initial Moiré pattern is illustrated by light red shading. As a result of modal coupling between the two rings, the Moiré pattern dictates the mode hybridization and consequently the dispersion characteristics. Lighter regions in the Moiré pattern indicate that ring mode frequencies coincide to form anti-symmetric and symmetric hybrid modes. Conversely, in the ‘interleaved’ regions where the mode resonant frequencies are spaced by $FSR/2$, the mode hybridization is greatly reduced (circled dots in Figure 4.3A). Next assume that the modes in ring B are collectively tuned by an optical frequency difference of Δf_{diff} relative to ring A modes. The minute adjustment is magnified by the Vernier ratio R causing a large shift in the Moiré pattern by Δf_o ($\Delta f_o = R\Delta f_{\text{diff}}$) that is illustrated by the blue shaded region.

The integrated dispersion of the coupled ring system is measured using a calibrated Mach-Zehnder interferometer (J. Li, H. Lee, K. Y. Yang, et al., 2012) and is shown for the two hybridized frequency bands in Figure 4.3B. Here, the quantity plotted is the integrated dispersion which is defined by $D_{\text{int,c}} = \omega_\mu - \omega_o - \overline{D}_1\mu - \frac{1}{2}D_{2,o}\mu^2$, where $\omega_o/2\pi$ is mode resonance frequency at $\mu \equiv m - m_o = 0$, $\overline{D}_1/2\pi$ is average FSR of the two rings, and $D_{2,o}$ is waveguide intrinsic group velocity dispersion. By differential tuning of the ring $FSRs$ the second set of dispersion spectra are measured in Figure 4.3B. Overall, the dispersion curve is shifted by 2.0 THz with an estimated temperature difference of 6 °C corresponding to a frequency shift by 10 GHz.

In Figure 4.3C dispersion spectra of the upper and lower frequency bands are again measured except for common-mode (not differential) tuning of the two rings. There is no measurable change in dispersion under this common mode tuning (note: the red and blue spectra are shifted vertically for comparison). Finally, to obtain an approximate value for the applied differential temperature change for the measurements in Figure 4.3B, common-mode frequency tuning data (inset of Figure 4.3D) is used to infer differential temperature change as shown in Figure 4.3D. Here, the measured dispersion shift at three points in Figure 4.3A is first plotted versus frequency by assuming a theoretical $R=200$ (expressed as 0.2 THz/GHz in the figure). Then, this scale is converted to differential temperature (upper horizontal axis) using the common-mode tuning data (inset data). Comparing the electrical

power consumption of the heaters, the measured differential tuning efficiency is 19.2 GHz/W, corresponding to phase change of 6.2×10^{-4} /W.

4.4 C-band operation of the same coupled ring device

Besides operation of a single device in three different modalities (see Figure 4.2D,E,F), it is significant to note that operation wavelength in any of these modes can be broadly tuned to match the requirements of a specific pump laser. For example, pumping of the upper band in Figure 4.3B will induce stimulated Brillouin lasing in the lower band provided that the difference in these frequencies ($\Delta\omega$) matches the phonon frequency. The idea is illustrated in Figure 4.4A which plots $\Delta\omega$ for the two tuning configurations in Figure 4.3B. A grey band gives the region where Brillouin phase matching is possible, while the accessible $\Delta\omega$ range is shaded in orange. The plots show that Brillouin laser operation over the entire optical C band is possible using a single device. This is demonstrated in Figure 4.4B where optical spectra show a series of pump and Brillouin laser operating wavelengths from a single device where phase matching has been electrically-controlled. In the spectra, the peak at the lower (higher) optical wavelength corresponds to the pump (Brillouin) laser. The Brillouin laser has been pumped using a tunable external cavity diode laser. However, as shown in Figure 4.2D, direct pumping from a hybridly-integrated semiconductor laser is also possible.

Broadband group velocity dispersion (GVD) tuning for dark and bright pulse generation at an arbitrary pumping wavelength is also possible. GVD (excluding single-ring waveguide dispersion, as defined by $D_{2,c} \equiv D_2 - D_{2,o}$) is evaluated by fitting the dispersion curve with a 3rd order polynomial (Figure 4.4C). The envelope of the dispersion curves sets a boundary of accessible anomalous and normal dispersion denoted by the shaded area (which is detailed in the next section). Figure 4.4D,E present a series of bright and dark soliton spectra obtained using a single device that has been directly pumped using the setup in Figure 4.2B. Four different DFB semiconductor lasers operating at four different wavelengths have been used. At each pumping wavelength tuning of the resonator dispersion allows operation in either the bright or dark mode (Yuan, Gao, et al., 2023; Ji, W. Jin, et al., 2023).

4.5 Noise performance

One concern of the system is if the enhanced tuning will simultaneously enhance the noise, like the case of exceptional point enhanced systems (H. Wang et al., 2020). The enhanced tuning in this system can make possible magnified fluctuations

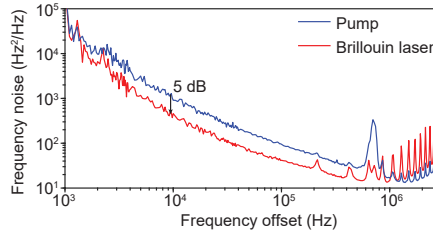


Figure 4.6: **Optical frequency noise spectrum of pump (self-injection-locked) and the Brillouin laser.**

in dispersion through differential temperature fluctuations. The exact impact of such fluctuations is still under investigation, however, some preliminary data and discussion is presented here.

Noise performance of the Brillouin laser

First, the optical frequency noise of the pump and SBS laser were characterized by collecting output from the bus waveguide using a lensed fiber. An Erbium-doped fiber amplifier was then used to boost optical power for measurements, followed by filtering of the pump (or the Brillouin laser) using a tunable fiber Bragg grating. The frequency noise spectrum was measured using the method in the reference Yuan, H. Wang, et al., 2022. Representative frequency noise spectra from the III-V pump and the Brillouin laser are shown in Figure 4.6.

Noise performance of the microcombs

Second, concerning microcomb repetition rate noise measurements, a similar version of the integrated microcomb studied here has been characterized in both free-running operation and in an optical frequency division (OFD) system. For the latter, the comb OFD system generated record-low noise microwave signals for a microcomb system suggesting that the Moiré effect does not significantly impair this critical application (Kudelin et al., 2024).

4.6 Conclusion

In conclusion, a single microresonator device is demonstrated to be electrically reconfigurable for operation as a Brillouin laser, a bright soliton microcomb or a dark pulse microcomb. This capability allows identical devices from the same wafer to be used in very different applications, or even mixed-mode operation on the same photonic chip. Consisting of a hybrid-integrated DFB laser (without optical isolators or amplifiers) and coupled-ring resonator the module is capable of full

heterogeneous integration (Xiang et al., 2023). The dispersion reconfiguration is also compatible with microresonators with larger *FSRs*, as well as faster actuators including piezoelectric (W. Jin et al., 2018; Alexander et al., 2018; J. Liu et al., 2020) and electro-optic control (C. Wang et al., 2019; Y. He et al., 2023) when required. Other potential applications that may benefit from the enhanced tunability include resonant electro-optic frequency combs (M. Zhang et al., 2019) and terahertz wave generation (Pidgayko et al., 2023; Chermoshentsev et al., 2022).

References

- Alexander, Koen et al. (2018). “Nanophotonic Pockels modulators on a silicon nitride platform.” In: *Nature Communications* 9.1, p. 3444.
- Bao, Chengying et al. (2021). “Architecture for microcomb-based GHz-mid-infrared dual-comb spectroscopy.” In: *Nature Communications* 12.1, p. 6573.
- Chermoshentsev, Dmitry A. et al. (2022). “Dual-laser self-injection locking to an integrated microresonator.” In: *Optics Express* 30.10, pp. 17094–17105.
- Fülöp, Attila et al. (2018). “High-order coherent communications using mode-locked dark-pulse Kerr combs from microresonators.” In: *Nature Communications* 9.1, pp. 1–8.
- Gabrielyan, Emin (2007). “The basics of line Moiré patterns and optical speedup.” In: *arXiv preprint physics/0703098*.
- Gundavarapu, Sarat et al. (2019). “Sub-hertz fundamental linewidth photonic integrated Brillouin laser.” In: *Nature Photonics* 13.1, pp. 60–67.
- He, Yang et al. (2023). “High-speed tunable microwave-rate soliton microcomb.” In: *Nature Communications* 14.1, p. 3467.
- Helgason, Óskar B., Francisco R. Arteaga-Sierra, et al. (2021). “Dissipative solitons in photonic molecules.” In: *Nature Photonics* 15.4, pp. 305–310.
- Helgason, Óskar B., Marcello Girardi, et al. (2023). “Surpassing the nonlinear conversion efficiency of soliton microcombs.” In: *Nature Photonics* 17.11, pp. 992–999.
- Herr, Tobias et al. (2014). “Temporal solitons in optical microresonators.” In: *Nature Photonics* 8.2, pp. 145–152.
- Hulme, Jared C., Jonathan K. Doylend, and John E. Bowers (2013). “Widely tunable Vernier ring laser on hybrid silicon.” In: *Optics Express* 21.17, pp. 19718–19722.
- Ji, Qing-Xin, Warren Jin, et al. (2023). “Engineered zero-dispersion microcombs using CMOS-ready photonics.” In: *Optica* 10.2, pp. 279–285.
- Ji, Qing-Xin, Peng Liu, et al. (2024). “Multimodality integrated microresonators using the Moiré speedup effect.” In: *Science* 383.6687, pp. 1080–1083.

- Jin, Warren et al. (2018). “Piezoelectrically tuned silicon nitride ring resonator.” In: *Optics Express* 26.3, pp. 3174–3187.
- Kudelin, Igor et al. (2024). “Photonic chip-based low-noise microwave oscillator.” In: *Nature* 627.8004, pp. 534–539.
- Lai, Yu-Hung et al. (2020). “Earth rotation measured by a chip-scale ring laser gyroscope.” In: *Nature Photonics* 14, pp. 345–349.
- Li, Jiang, Hansuek Lee, Tong Chen, et al. (2012). “Characterization of a high coherence, Brillouin microcavity laser on silicon.” In: *Optics Express* 20.18, pp. 20170–20180.
- Li, Jiang, Hansuek Lee, and Kerry J. Vahala (2013). “Microwave synthesizer using an on-chip Brillouin oscillator.” In: *Nature Communications* 4.1, pp. 1–7.
- Li, Jiang, Hansuek Lee, Ki Youl Yang, et al. (2012). “Sideband spectroscopy and dispersion measurement in microcavities.” In: *Optics Express* 20.24, pp. 26337–26344.
- Little, Brent E. et al. (1997). “Microring resonator channel dropping filters.” In: *Journal of Lightwave Technology* 15.6, pp. 998–1005.
- Liu, Junqiu et al. (2020). “Monolithic piezoelectric control of soliton microcombs.” In: *Nature* 583.7816, pp. 385–390.
- Loh, William et al. (2020). “Operation of an optical atomic clock with a Brillouin laser subsystem.” In: *Nature* 588.7837, pp. 244–249.
- Newman, Zachary L. et al. (2019). “Architecture for the photonic integration of an optical atomic clock.” In: *Optica* 6.5, pp. 680–685.
- Obrzud, Ewelina et al. (2019). “A microphotonic astrocomb.” In: *Nature Photonics* 13.1, p. 31.
- Okawachi, Yoshitomo et al. (2022). “Active tuning of dispersive waves in Kerr soliton combs.” In: *Optics Letters* 47.9, pp. 2234–2237.
- Oster, Gerald and Yasunori Nishijima (1963). “Moiré patterns.” In: *Scientific American* 208.5, pp. 54–63.
- Panuski, Christopher, Dirk Englund, and Ryan Hamerly (2020). “Fundamental thermal noise limits for optical microcavities.” In: *Physical Review X* 10.4, p. 041046.
- Pavlov, Nikolay G. et al. (2018). “Narrow-linewidth lasing and soliton Kerr microcombs with ordinary laser diodes.” In: *Nature Photonics* 12.11, pp. 694–698.
- Pidgayko, Dmitry et al. (2023). “Voltage-tunable optical parametric oscillator with an alternating dispersion dimer integrated on a chip.” In: *Optica* 10.11, pp. 1582–1586.
- Shen, Boqiang et al. (2020). “Integrated turnkey soliton microcombs.” In: *Nature* 582.7812, pp. 365–369.

- Shu, Haowen et al. (2022). “Microcomb-driven silicon photonic systems.” In: *Nature* 605.7910, pp. 457–463.
- Spencer, Daryl T. et al. (2018). “An optical-frequency synthesizer using integrated photonics.” In: *Nature* 557.7703, pp. 81–85.
- Suh, Myoung-Gyun and Kerry J. Vahala (2018). “Soliton microcomb range measurement.” In: *Science* 359.6378, pp. 884–887.
- Suh, Myoung-Gyun, Qi-Fan Yang, et al. (2016). “Microresonator soliton dual-comb spectroscopy.” In: *Science* 354.6312, pp. 600–603.
- Suh, Myoung-Gyun, Xu Yi, et al. (2019). “Searching for exoplanets using a microresonator astrocomb.” In: *Nature Photonics* 13, pp. 25–30.
- Trocha, Philipp et al. (2018). “Ultrafast optical ranging using microresonator soliton frequency combs.” In: *Science* 359.6378, pp. 887–891.
- Wang, Cheng et al. (2019). “Monolithic lithium niobate photonic circuits for Kerr frequency comb generation and modulation.” In: *Nature Communications* 10.1, p. 978.
- Wang, Heming et al. (2020). “Petermann-factor sensitivity limit near an exceptional point in a Brillouin ring laser gyroscope.” In: *Nature Communications* 11.1, p. 1610.
- Xiang, Chao et al. (2023). “3D integration enables ultralow-noise isolator-free lasers in silicon photonics.” In: *Nature* 620.7972, pp. 78–85.
- Xue, Xiaoxiao, Yi Xuan, Yang Liu, et al. (2015). “Mode-locked dark pulse Kerr combs in normal-dispersion microresonators.” In: *Nature Photonics* 9.9, pp. 594–600.
- Xue, Xiaoxiao, Yi Xuan, Pei-Hsun Wang, et al. (2015). “Normal-dispersion microcombs enabled by controllable mode interactions.” In: *Laser & Photonics Reviews* 9.4, pp. L23–L28.
- Yuan, Zhiquan, Maodong Gao, et al. (2023). “Soliton pulse pairs at multiple colours in normal dispersion microresonators.” In: *Nature Photonics* 17.11, pp. 977–983.
- Yuan, Zhiquan, Heming Wang, et al. (2022). “Correlated self-heterodyne method for ultra-low-noise laser linewidth measurements.” In: *Optics Express* 30.14, pp. 25147–25161.
- Zhang, Mian et al. (2019). “Broadband electro-optic frequency comb generation in a lithium niobate microring resonator.” In: *Nature* 568.7752, pp. 373–377.

DISPERSION-AGILE THREE-COUPLED-RING RESONATOR

The *Moiré speedup effect* can be naturally extended to systems of more than two Vernier-coupled rings. In practice, dispersion tuning in two-coupled-rings (2CR) devices is primarily limited to second-order dispersion (D_2), while the residual third-order dispersion (D_3) often remains significant. This residual dispersion constrains the range of accessible microcomb states. By introducing a third ring, an additional degree of freedom is enabled for dispersion control. This allows for simultaneous tuning of both D_2 and D_3 , enabling generation of bright soliton microcombs with agile dispersive waves and shorter pulse durations. These features benefit applications such as the 2P-OFD (Q.-X. Ji, W. Zhang, Savchenkov, et al., 2025) and supercontinuum generation.

Despite its seemingly complex structure, the dispersion tuning process in the three coupled ring (3CR) resonator is systematic and programmable. Moreover, microcombs in this configuration can be generated using pump power levels accessible to compact III-V distributed feedback (DFB) lasers, paving the way for low-power, integrated solutions.

5.1 Theory of dispersion tuning in the three-coupled-ring resonator

In this section, the theory that describes the dispersion spectrum of the 3-coupled-ring resonator is described. Calculation of the dispersion is detailed in (Yuan et al., 2023). Briefly, a transfer matrix, T , is used to propagate a 3-component wave function through a round trip.

$$T = e^{i\omega\bar{L}/c} \begin{pmatrix} e^{i2\pi m(-\epsilon_1+\epsilon_2)} \cos(g_{\text{co}}L_{\text{co}}) & ie^{-i4\pi m\epsilon_2} \cos(g_{\text{co}}L_{\text{co}}) \sin(g_{\text{co}}L_{\text{co}}) & -e^{i2\pi m(\epsilon_1+\epsilon_2)} \sin^2(g_{\text{co}}L_{\text{co}}) \\ ie^{i2\pi m(-\epsilon_1+\epsilon_2)} \sin(g_{\text{co}}L_{\text{co}}) & e^{-4i\pi m\epsilon_2} \cos^2(g_{\text{co}}L_{\text{co}}) & ie^{i2\pi m(\epsilon_1+\epsilon_2)} \cos(g_{\text{co}}L_{\text{co}}) \sin(g_{\text{co}}L_{\text{co}}) \\ 0 & ie^{-i4\pi m\epsilon_2} \sin(g_{\text{co}}L_{\text{co}}) & e^{i2\pi m(\epsilon_1+\epsilon_2)} \cos(g_{\text{co}}L_{\text{co}}) \end{pmatrix}. \quad (5.1)$$

The resulting secular equation gives the eigenfrequencies, ω , of the three mode families (see plot in Figure 5.1a), where m is mode number, $\epsilon_1 \equiv (L_B - L_C)/2\bar{L}$, and $\epsilon_2 \equiv (L_B + L_C - 2L_A)/6\bar{L}$. Here, $\bar{L} \equiv (n_{\text{wg,B}}l_B + n_{\text{wg,C}}l_C)/2$ is the averaged optical path length of ring B and C (left and right rings), $L_i \equiv n_{\text{wg,i}}l_i$ is the round-trip optical path length of any of the three rings (i=A,B,C), where $n_{\text{wg,i}}$ is the effective index of the waveguide that forms the ring (which can be tuned via the thermo-optic effect) and l_i is the physical round trip length of an individual ring (which can

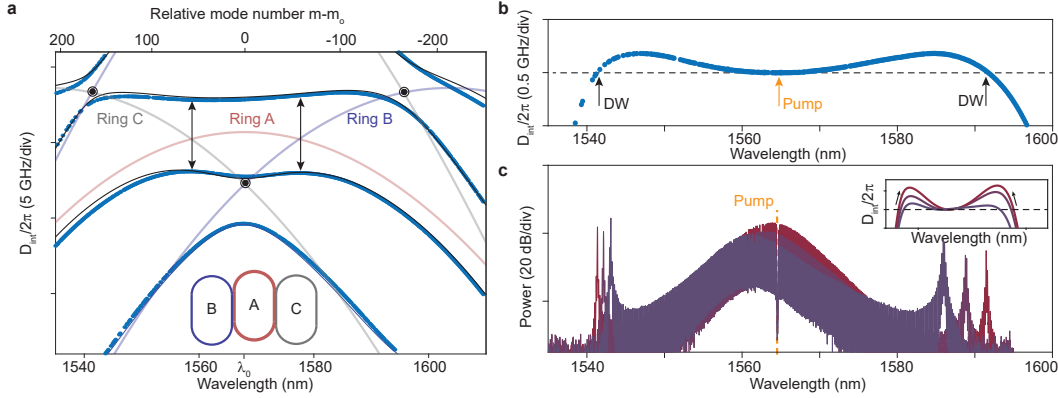


Figure 5.1: Dispersion and bright soliton microcomb with electrically tunable dispersive wave. **a**, Measured dispersion spectrum showing the 3 dispersion bands of the 3CR device (blue dots). The theoretical fitting is plotted as the solid curves, and the inferred dispersion of the uncoupled rings are the shaded lines (red, blue and gray for ring A, B, and C, respectively). The relative mode number $m - m_0$ is plotted in the upper axis, where m_0 corresponds to the intersection of the uncoupled ring B and ring C dispersion curves. The corresponding wavelength is $\lambda_0 = 1568$ nm (lower axis). **b**, Isolated dispersion spectrum for the upper band in panel a. Dashed horizontal line gives location of the dispersive wave phase matching wavelengths. **c**, Optical spectral of bright soliton microcomb showing tuning of the dispersive waves. Inset: illustration of the dispersion changing when the heaters are differentially fine-tuned. The arrows indicate the change of the dispersion curves when ring A is heated.

be tuned via the thermo-elastic effect). $g_{co}L_{co}$ is the amplitude coupling strength between the neighboring rings (ring A and B, ring A and C).

The secular equation after a round trip can be simplified to a polynomial equation,

$$x^3 - (e^{-2i\phi_2} \cos(g_{co}L_{co}) + 2e^{i\phi_2} \cos(\phi_1)) \cos(g_{co}L_{co})x^2 \quad (5.2)$$

$$+ (e^{2i\phi_2} \cos(g_{co}L_{co}) + 2e^{-i\phi_2} \cos(\phi_1)) \cos(g_{co}L_{co})x - 1 = 0, \quad (5.3)$$

where $x \equiv e^{i\theta}$ and $\omega = \omega_m - \frac{D_1}{2\pi}\theta$, with $\omega_m = 2\pi mc/\bar{L}$, $D_1/2\pi$ the average *FSR* of the three rings, and c the speed of light in vacuum. $\phi_1 \equiv 2\pi m\epsilon_1$ and $\phi_2 \equiv 2\pi m\epsilon_2$ are parameters that govern the dispersion spectrum. Three dispersion bands will be formed since Equation 5.3 is a third order polynomial of x .

The above Equation 5.3 does not have a simple solution, but there are still features that can be inferred in terms of the dispersion spectrum. For example, $\phi_1 = 2\pi\epsilon_1 m_0 = 2\pi N$ (N is an integer) defines the mode number where the dispersion curves of the uncoupled ring B and ring C will intersect (Figure 5.1a). At this

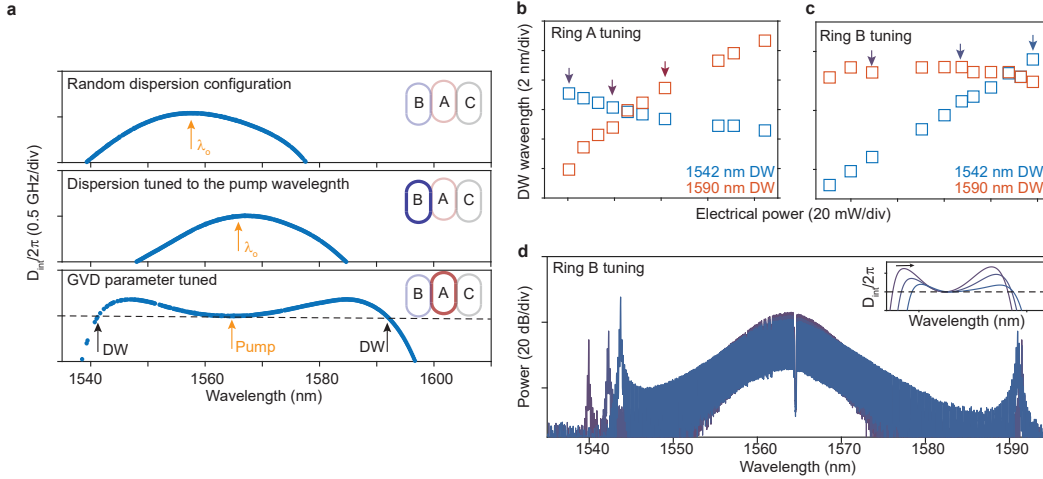


Figure 5.2: Dispersion tuning and dispersive wave tuning in the bright soliton microcomb using electrical heaters. **a**, Upper panel: measured dispersion spectrum of the 3-coupled-ring (3CR) resonator with random heater tuning. Middle panel: measured dispersion spectrum of the 3CR after tuning λ_0 closer to the pump wavelength (1565 nm) by heating ring B. Lower panel: measured dispersion spectrum of the 3CR after the local GVD parameter is tuned by heating ring A. **b,c**, Measurement of dispersive wave tuning when ring A (B) is fine-tuned. The 1542 nm dispersive wave is plotted in blue, while the 1590 nm dispersive wave is plotted in red. The corresponding data points in Figure 5.1c and panel d are indicated by the arrows (matched by the colours). **d**, Measured optical spectra of the bright soliton microcomb with three different dispersive wave tunings. Inset: theoretical dispersion spectra when ring B is tuned. The arrow indicates the change of the dispersion curves when ring B is heated.

mode number the corresponding wavelength is λ_0 . For the device used in this study, $\epsilon_1 \approx 3 \times 10^{-3}$ by design and is measured to be within 1% of this value. ϵ_2 is measured to be $\epsilon_2 \sim 10^{-5}$ which is consistent with a design target close to zero. However, slight fabrication variances modify the dispersion curve and impair soliton mode locking at the pump wavelength. To acquire dispersion bands that are favorable for soliton mode locking, heater tuning is applied to tune λ_0 (m_0) and ϕ_2 . After the heater tuning, the dispersion is as shown in Figure 5.1a wherein the fitted parameters are $\phi_2 = -0.36$, and $g_{co}l_{co} = 0.9$ near $\lambda_0 = 1568$ nm ($m_0 \approx 9567$). Further details on this tuning procedure are given below.

5.2 Dispersion centering and flattening

Based on the analysis in the previous section, the dispersion curve is determined by two parameters ϕ_1 and ϕ_2 . Experimentally, ring B (or C) is thermally tuned to change ϕ_1 and, in turn, λ_0 . Ring A is thermally tuned to change ϕ_2 and, in turn,

can be shown to tune the GVD parameter at λ_0 . Specifically, differential heating of ring A increases the curvature of the pumped band near λ_0 (amount of anomalous dispersion), as in the inset of Figure 5.1c. These tuning steps are largely independent and enable a 2-step dispersion tuning protocol described in Figure 5.2a. In the first step, ring B is tuned (ϕ_1 is tuned) such that λ_0 is tuned close to the pump wavelength (1565 nm). In the second step, ring A is tuned (ϕ_2 is tuned) with ϕ_1 unchanged. The resulting dispersion is shown in the lower panel of Figure 5.2a (also in Figure 5.1b).

The dispersion tuning is efficient, requiring only a moderate amount of actual temperature tuning. Tuning of λ_0 benefits from the Vernier effect as described in the reference (Q.-X. Ji et al., 2024), and experimentally ~ 10 °C of differential temperature tuning is sufficient to tune the pump wavelength λ_0 across the optical C band. The local curvature of the dispersion bands (GVD parameter) near λ_0 is determined by differential thermal tuning in ring A. The tuning of uncoupled mode resonance in ring A by one *FSR* (20 GHz) will access all the possible dispersion configurations. This corresponds to tuning of L_A by \bar{L}/m . With a large mode number $m \sim 10^4$ in the optical C band, this corresponds to < 10 °C of differential temperature tuning.

5.3 Dispersive wave emission and tuning

The upper band is used for microcomb generation and is pumped near 1565 nm. Concerning the structure of these bands, there is no simple closed-form expression for the dispersion spectrum, but there are some universal features. The dispersion spectra of the uncoupled rings are indicated by the colored curves (red, blue and gray for the three rings, respectively). Where ring A crosses ring B and ring C curves (indicated by the two arrows) two bandgaps are opened upon introduction of ring coupling. Also note that ring B and ring C are able to indirectly couple to each other through their mutual interaction with ring A. This coupling creates another smaller bandgap. The magnitude of these gaps can be related to coupling strength and dispersion, as previously discussed.

The dispersion curve of the 3CR system allows generation of double dispersive waves. These waves form at frequencies where soliton frequency components are nearly resonant with cavity modes (black arrows in Figure 5.1b). And controlled electrical (heater) tuning of the dispersive wave wavelength is used for matching to one of the c.w. lasers in the optical frequency division measurement. This capability

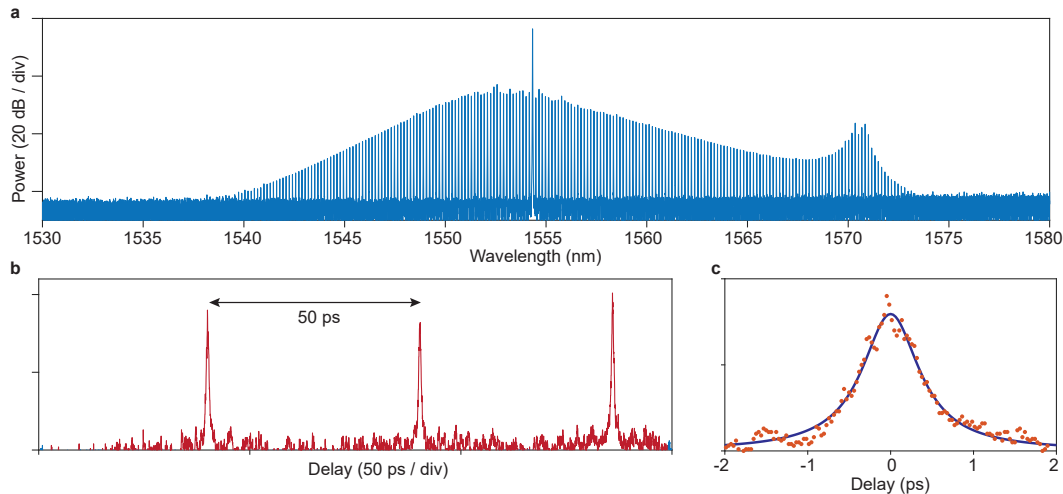


Figure 5.3: **Temporal characterization of the bright soliton microcomb.** **a**, Optical spectrum of the bright soliton microcomb. **b**, Autocorrelation trace showing repetitive pulses with a 50 ps period (20 GHz repetition rate). **c**, Autocorrelation data (red dots) with Lorentzian fitting (solid line). The full-width at half-maximum (FWHM) of the autocorrelation signal is 843 fs, corresponding to a single-pulse intensity FWHM of approximately 500 fs.

greatly strengthens the beatnote SNR and enables flexible access to a wider range of c.w. lasers, whose wavelengths may not be widely tunable. Microcomb optical spectra showing different dispersive wave tunings are plotted in Figure 5.1c. Tuning of the shorter wavelength dispersive wave by 4 nm and the longer wavelength dispersive wave by 8 nm is possible (see Figure 5.2). It is also noted that adjusting the pump laser-microresonator detuning allows tuning of the dispersive wave (Q.-F. Yang, Yi, et al., 2016), but this provides only limited tuning range (~ 0.2 nm). As an aside, the bright soliton microcomb is triggered using the method described in the reference (Stone et al., 2018).

5.4 Microcomb-pumped mid-infrared light generation

Mid-infrared (mid-IR) light sources are vital for applications such as molecular spectroscopy, environmental monitoring, and astrocomb. Optical frequency combs have been widely used in spectroscopic applications, both in single-comb (Bao, Yuan, H. Wang, et al., 2020; Stern et al., 2020) and dual-comb (Suh et al., 2016; Dutt et al., 2018; Q.-F. Yang, Shen, et al., 2019; Bao, Yuan, L. Wu, et al., 2021) schemes. However, low repetition-rate (~ 10 GHz) microcombs typically have limited bandwidth around the 1550 nm region, which is suboptimal for broadband molecular detection in the mid-IR. An alternative approach is to start with a sub-picosecond

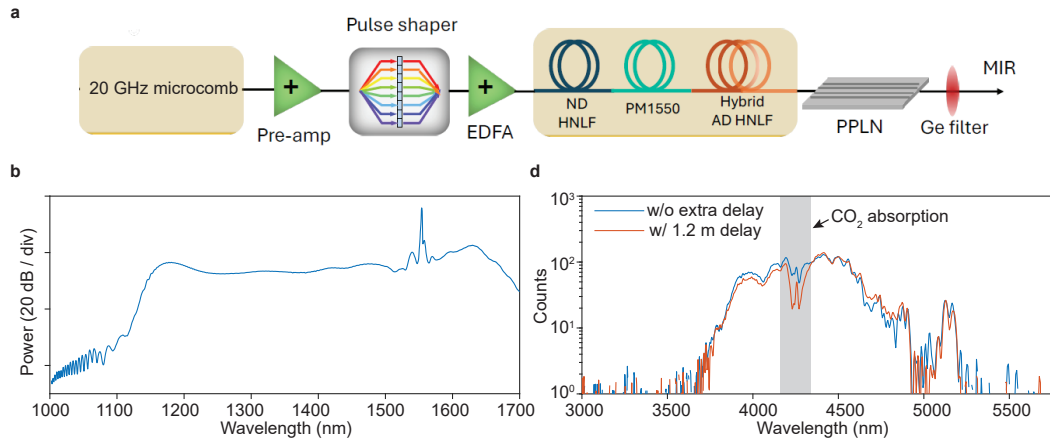


Figure 5.4: Mid-infrared light generation results. **a**, Experimental setup. EDFA: erbium-doped fiber amplifier. ND HNLF: normal-dispersion highly nonlinear fiber. AD HNLF: anomalous-dispersion highly nonlinear fiber. PPLN: periodically poled lithium niobate. (Materials courtesy of Pooja Sekhar, CU Boulder.)

microcomb pulse and use supercontinuum generation (SCG) to access broader spectral regions. With recent advances in chip-scale supercontinuum waveguides (Oh et al., 2014; T.-H. Wu et al., 2024), integrated amplifiers (Y. Liu et al., 2022), and pulse-shaping elements (Cohen et al., 2024), a fully miniaturized broadband mid-IR source becomes feasible.

The bright soliton microcomb demonstrated earlier in this chapter provides such a sub-picosecond source. It operates in a self-injection-locked configuration and is co-packaged with a III-V laser pump for long-term stability (details in Chapter 6.2). Temporal characterization is shown in Figure 5.3b,c.

The microcomb is delivered to CU Boulder for mid-infrared light generation. The setup and results are in Figure 5.4. The microcomb output is pre-amplified to 50 mW; a pulse shaper compensates the pre-amplifier dispersion. The other EDFA amplifies the microcomb to 5 W, and then the pulse is compressed to approximately 60 fs using a combination of normal dispersion highly-nonlinear fiber (ND HNLF) and PM1550. These compressed pulses are subsequently propagated through hybrid anomalous dispersion (AD) HNLF, consisting of 19 cm of $D = 2$ ps/nm/km and 9 cm of $D = 4.9$ ps/nm/km fiber, for spectral broadening to $\sim 1.16 \mu\text{m}$ (Figure 5.4b). After spectral broadening, the average power is measured to be ~ 1.4 W and the transform-limited pulse duration is approximately 17 fs. Details on the all-fiber-integrated temporal compression and nonlinear broadening can be found in (Sekhar et al., 2023).

After spectral broadening, the output from HNLFF is directly coupled into a periodically poled lithium niobate (PPLN) waveguide with a cross-section of $15\ \mu\text{m}$ by $16\ \mu\text{m}$. The commercial waveguide (NTT) is fabricated from ZnO-doped LN on a lithium tantalate substrate with poling periods ranging from 20 to $30\ \mu\text{m}$ along the 10 mm long waveguide (Figure 5.4a). These poling periods are designed to generate mid-infrared light spanning 3 to $5\ \mu\text{m}$ via intra-pulse difference frequency generation (IP-DFG). The output mid-infrared light, generated with only 35 pJ of in-coupled pump pulse energy from the 20 GHz microcomb, is filtered using a germanium filter and focused onto a Fourier-transform spectrometer (FTIR). The recorded spectrum, spanning 3.8 - $5.2\ \mu\text{m}$ as shown in Figure 5.4c, measures approximately 100 μW . Absorbance from atmospheric carbon-dioxide around $4.3\ \mu\text{m}$ is also observed (Figure 5.4c). The resolution of FTIR is insufficient to resolve the comb modes.

References

- Bao, Chengying, Zhiquan Yuan, Heming Wang, et al. (2020). “Interleaved difference-frequency generation for microcomb spectral densification in the mid-infrared.” In: *Optica* 7.4, pp. 309–315.
- Bao, Chengying, Zhiquan Yuan, Lue Wu, et al. (2021). “Architecture for microcomb-based GHz-mid-infrared dual-comb spectroscopy.” In: *Nature Communications* 12.1, p. 6573.
- Cohen, Lucas M. et al. (2024). “Silicon photonic microresonator-based high-resolution line-by-line pulse shaping.” In: *Nature Communications* 15.1, p. 7878.
- Dutt, Avik et al. (2018). “On-chip dual-comb source for spectroscopy.” In: *Sci. Adv.* 4.3, e1701858.
- Ji, Qing-Xin et al. (2024). “Multimodality integrated microresonators using the Moiré speedup effect.” In: *Science* 383.6687, pp. 1080–1083.
- Liu, Yang et al. (2022). “A photonic integrated circuit-based erbium-doped amplifier.” In: *Science* 376.6599, pp. 1309–1313.
- Oh, Dong Yoon et al. (2014). “Supercontinuum generation in an on-chip silica waveguide.” In: *Optics Letters* 39.4, pp. 1046–1048.
- Sekhar, Pooja et al. (2023). “20 GHz fiber-integrated femtosecond pulse and supercontinuum generation with a resonant electro-optic frequency comb.” In: *APL Photonics* 8.11.
- Stern, Liron et al. (2020). “Direct Kerr frequency comb atomic spectroscopy and stabilization.” In: *Science advances* 6.9, eaax6230.

- Stone, Jordan R. et al. (2018). “Thermal and nonlinear dissipative-soliton dynamics in Kerr-microresonator frequency combs.” In: *Physical Review Letters* 121.6, p. 063902.
- Suh, Myoung-Gyun et al. (2016). “Microresonator soliton dual-comb spectroscopy.” In: *Science* 354.6312, pp. 600–603.
- Wu, Tsung-Han et al. (2024). “Visible-to-ultraviolet frequency comb generation in lithium niobate nanophotonic waveguides.” In: *Nature Photonics* 18.3, pp. 218–223.
- Yang, Qi-Fan, Boqiang Shen, et al. (2019). “Vernier spectrometer using counter-propagating soliton microcombs.” In: *Science* 363.6430, pp. 965–968.
- Yang, Qi-Fan, Xu Yi, et al. (2016). “Spatial-mode-interaction-induced dispersive-waves and their active tuning in microresonators.” In: *Optica* 3, pp. 1132–1135.
- Yuan, Zhiquan et al. (2023). “Soliton pulse pairs at multiple colours in normal dispersion microresonators.” In: *Nature Photonics* 17.11, pp. 977–983.

Chapter 6

AVENUES OF SYSTEM INTEGRATION

As electronic equipment became more complex, shortcomings in this procedure began to appear. The cost of the equipment increased more rapidly than the component count, and equipment reliability suffered a corresponding decrease.

Jack S. Kilby

Integrated photonics holds immense promise: high-yield production, low cost, and superior SWaP (size, weight, and power). Yet, when photonic components are assembled into a complete, functional system, new challenges arise, and must be addressed to realize those promises in practice. This is especially true for the chip-scale 2P-OFD system proposed in this thesis.

This chapter explores paths toward full system integration, with the goal of realizing a robust, deliverable photonic system. Section 6.1 outlines the vision of integrating all components on a single silicon chip via heterogeneous integration—a compelling but ultimately difficult path. Section 6.2 presents progress in hybrid packaging of key components, demonstrating stable running and good performance in terms of Allan deviation. Section 6.3 describes early success in incorporating monolithic piezoelectric tuners, achieving simultaneous locking of both the reference laser and the microcomb.

6.1 Vision of full system integration in early 2023

In early 2023, a conceptual vision of full integration of the OFD system is presented, whereas all the components required in Chapter 2 can be integrated to the same chip (Kudelin et al., 2024). The concept of such a fully integrated system is shown in Figure 6.1 and would consist of heterogeneously integrated lasers at 1560 nm (Guo, Charles A. McLemore, et al., 2022), spiral resonators (B. Li et al., 2021) for SIL, a coupled-ring microcomb resonator (Q.-X. Ji, P. Liu, et al., 2024), photodetectors

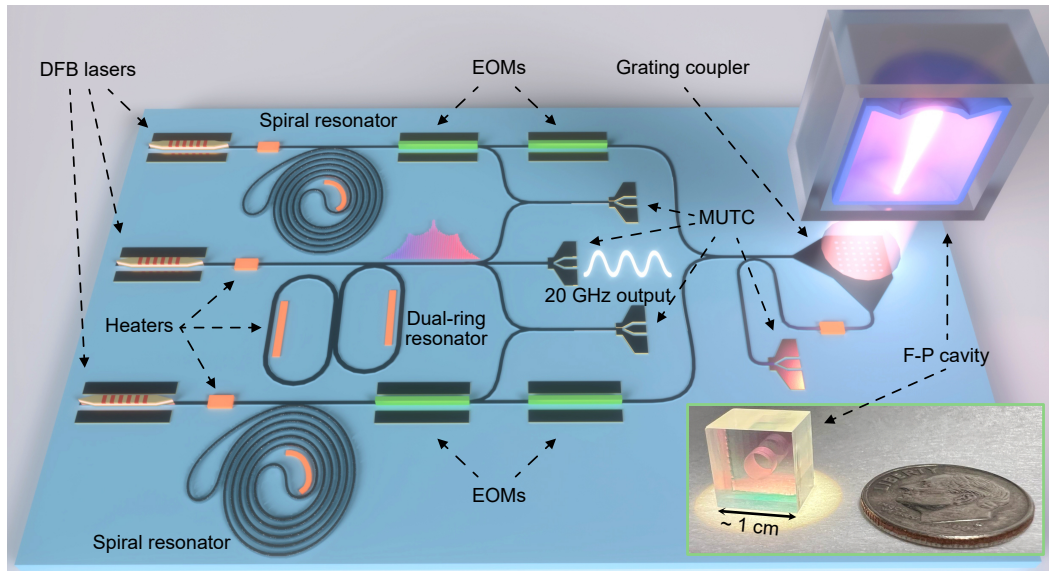


Figure 6.1: **Schematic design of a photonic microwave oscillator on a single chip.** The integrated system employs the same key photonic elements used in this work. Two spiral-resonator SIL lasers are PDH-locked to the same micro FP cavity with two EOMs in series for each SIL laser—the first for fast phase correction and the second for PDH sidebands. The right side of the schematic shows the FP cavity interface, where the two SIL laser paths are fed through an interferometer with an embedded polarization splitting grating. This serves as a reflection cancellation circuit while also shaping the planar waveguide mode to match the FP mode (Cheng et al., 2023). The reflection from the FP cavity is then detected by the right-most detector. Inset: Photo of the miniature FP cavity, consisted of micro-fabricated mirrors (N. Jin et al., 2022), with overall volume of $\sim 1 \text{ cm}^3$.

(Zang et al., 2018) and a micro-fabricated FP cavity that does not require high vacuum (N. Jin et al., 2022; Yifan Liu et al., 2024; W. Zhang et al., 2024).

Previous work already lays out the steps for heterogeneous integration of lasers and Si_3N_4 resonators with low loss (Xiang, J. Liu, et al., 2021; Xiang, W. Jin, et al., 2023), which can be applied to the 100-nm thick Si_3N_4 , coupled ring resonators. Furthermore, laser integration with modulators and detectors has also been previously demonstrated (Xie et al., 2019) and can be utilized for full integration of all the optical components comprising the PDH locking system (Idjadi and Aflatouni, 2017).

In the integration scheme, the laser locking feedback control can be replaced with a combination of slow feedback to the integrated heaters in the spirals and fast feedback to DFB current and EOMs (Endo and Schibli, 2018). The thermal tuning

can reach a bandwidth of a few kilohertz (Xiang, W. Jin, et al., 2023), whereas the fast feedback with a bandwidth of several megahertz could be provided by the EOM or current modulation (Idjadi and Aflatouni, 2017; Xie et al., 2019). We estimate that this combination can provide 40 dB feedback gain at 10 kHz offset frequency to match the phase noise performance of the presented work. The PDH locking approach can also be potentially replaced by self-injection locking a III-V DFB laser to the FP cavity (Savchenkov et al., 2024).

The integration of the active and passive components on a single platform greatly reduces loss (between fiber and chip) and may remove the need for optical amplifiers employed in the present work. Besides, photonic integration of SOAs or EDFAs is feasible (Yang Liu et al., 2022).

Integration of the FP cavity has been an outstanding challenge, but recent developments in micro-fabricated mirrors (N. Jin et al., 2022) and compact thermal-noise limited FP designs (Charles A. McLemore et al., 2022) provide new integration opportunities. Critically, it has been shown that 2P-OFD does not require FP operation in high-vacuum (Yifan Liu et al., 2024; W. Zhang et al., 2024), significantly simplifying future integration. Figure 6.1 shows a 1cm^3 cavity with fabricated micro-mirrors and details on an integration strategy with the the SIL lasers and microcomb. A planar waveguide feeds an inverse-designed polarization splitting grating embedded in an interferometer, which serves to shape the beam for coupling light to the cavity while also providing the cavity-reflected PDH locking signal and laser isolation (Cheng et al., 2023).

The integration scheme presented in Figure 6.1 has been actively pursued into reality since 2023 to the time of this thesis. However, despite numerous progress, it turns out a single-chip integration of all the components is overwhelmingly challenging. The routing between layers of III-V, silicon, Si_3N_4 also induce unexpected losses and failure possibility in fabrications. As a result, the avenue of hybrid integration is chosen as an alternative (Chapter 6.2); monolithic piezoelectric tuning of Si_3N_4 circuits, instead of routing light across different kinds of optical waveguides, is also achieving success (Chapter 6.3).

6.2 Hybrid system packaging and Allan deviation results

The high- Q factor property of the 3CR resonator allows low pumping power operation, enabling direct pumping by a III-V DFB laser under the turnkey self-injection locking mode (Shen et al., 2020). Here, a hybrid packaged module containing a

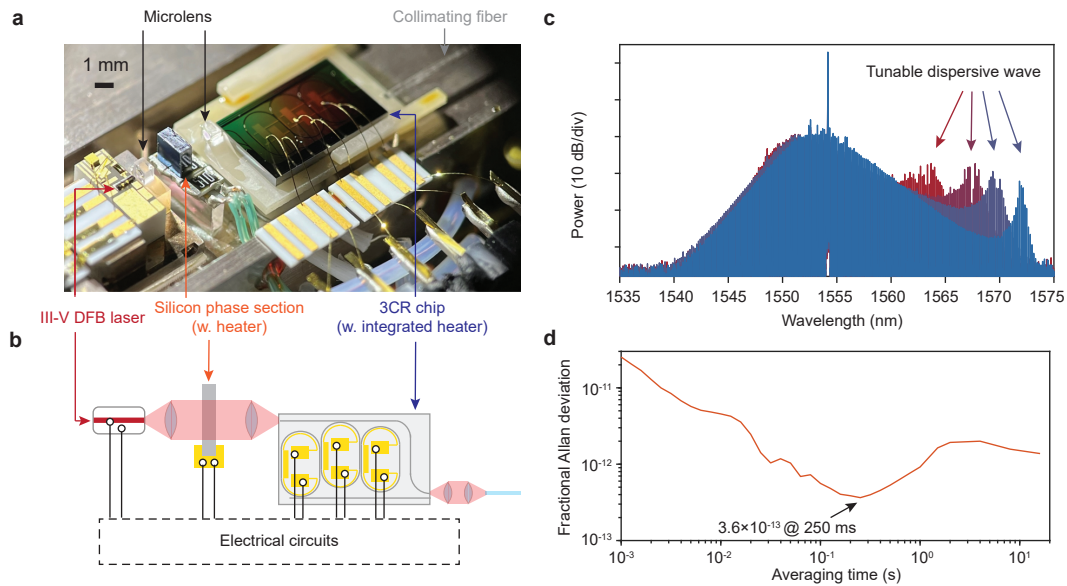


Figure 6.2: Hybrid packaging of the dispersive-wave-tunable microcomb, and Allan deviation results. **a**, Photograph of the hybridly packaged 3CR chip with III-V pump. **b**, Illustration of the packaging scheme. Output of the DFB laser is collected by a microlens, and passes through an anti-reflection coated silicon slab for feedback phase tuning (via electrical heating). The light is later focused by another microlens to be coupled into the Si_3N_4 waveguide. Heaters are deposited on the 3CR chip and wire-bonded, and dispersion is tuned to support bright soliton mode locking. The output beam of the Si_3N_4 waveguide is shaped by another pair of microlenses and collected by an optical fiber ferrule. **c**, Measured optical spectra from the hybrid-integrated microcomb module showing tuning of the dispersive wave. **d**, Allan deviation results. Fractional Allan deviation of 3.6×10^{-13} is measured at the averaging time of 250 ms. For averaging time > 1 s, a linear drift of 0.013 Hz/s is removed.

III-V DFB pump and the 3CR is demonstrated (module photograph in Figure 6.2a, and design concept in Figure 6.2b). A commercial III-V DFB laser (Emcore Corporation) emits ~ 100 mW laser light, and is collimated by a microlens. The beam passes through an anti-reflection coated silicon slab for feedback phase tuning in the self-injection lock process, below which a resistive heater is placed for thermal tuning. After that, the beam is focused by another microlens onto the 3CR bus waveguide facet, where ~ 30 mW of optical power is estimated on the chip. Dispersion of the 3CR resonator is tuned based on the procedure described in the earlier chapters, and the soliton microcomb with tunable dispersive wave is generated by approximately tuning the laser current and heating on the silicon phase section. The output of the 3CR bus waveguide is resized by two microlenses (Figure 6.2b), and

collected by a ferrule for fiber-coupled output. The nominal collected power in the fiber (when the DFB laser is not on resonance of the 3CR resonator) is ~ 8 mW. The collected optical spectra demonstrates the tunable dispersive wave (Figure 6.2c).

The hybrid packaging improves the long-term stability of the microcomb for Allan deviation characterization of the 2P-OFD system. In the packaging, the DFB and the 3CR are, respectively, temperature-controlled by a TEC and the thermistor, with below mK temperature fluctuation. The module assembly in Figure 6.2a is covered by an aluminum enclosure for passive stabilization. The module is embedded in the 2P-OFD setup (as in Figure 6.2e), by feeding back to the current of the DFB laser (Q.-X. Ji, W. Jin, et al., 2023; Kudelin et al., 2024). Fractional Allan deviation of 3.6×10^{-13} is measured at the averaging time of 250 ms (Figure 6.2d). It is noted that the Allan deviation benefits from the common mode suppression by locking the two C.W. lasers to the same mode family of the FP cavity (Groman et al., 2024).

The demonstrated fractional Allan deviation of the microwave output at 1s is the lowest reported to date using similar approaches (Papp et al., 2014; Newman et al., 2019; Kwon et al., 2022; Q.-X. Ji, W. Zhang, Wu, et al., 2024). The low level results from common mode suppression provided by locking the two lasers to the same mode of the FP cavity. Specifically, it is lower than the thermorefractive noise limit by ~ 20 times. To see this, consider that the thermorefractive noise limit is ~ 10 Hz in Allan deviation for each individual laser between the averaging times of 100 ms and 1 s (W. Zhang et al., 2024). To estimate the resulting noise limit after the 2P-OFD (without the common mode suppression), the relative Allan deviation of the two lasers is multiplied by a factor of $\sqrt{2}$, and divided by the 2P-OFD separation of 2 THz. The fractional Allan deviation is thus $10 \text{ Hz} \times \sqrt{2}/2 \text{ THz} = 7 \times 10^{-12}$. This is ~ 20 times higher than the measured Allan deviation of 3.6×10^{-13} at 250 ms.

6.3 Monolithic piezoelectric control: preliminary results

The piezoelectric actuators are fabricated using ultra-low-loss Si_3N_4 (W. Jin, Yang, et al., 2021; J. Liu et al., 2020). For the design of the piezoelectric actuators, AlN was chosen for its reasonably high piezoelectric coefficient, as well as its previously demonstrated low hysteresis compared with PZT. The actuator is deposited on the top silica cladding ($4.25 \mu\text{m}$ thickness) with $>6 \mu\text{m}$ horizontal offset to mitigate metal-induced absorption from the bottom electrode. This is illustrated in Figure 6.3a. The piezo elements wrap around the interior-edge of the ring waveguide circumference.

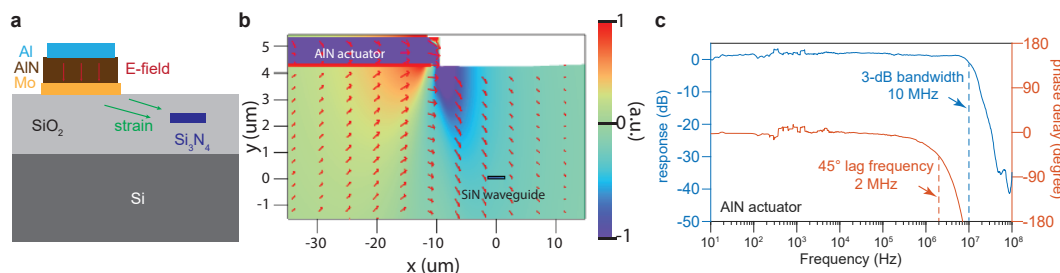


Figure 6.3: **Tuning of Si_3N_4 circuits via AlN piezoelectric actuation.** **a**, Schematic cross section of the chip. Piezoelectric strain induced by an electric field changes the refractive index of optical waveguides, resulting in resonance frequency shifts. **b**, AlN actuator induced stress tensor σ_{xx} is plotted in color, and the arrows denote the stress-induced mechanical force. **c**, Amplitude and phase of frequency response of the piezoelectric actuator on a single ring. The measurement used the method similar to Figure 4.1.

When the upper electrode is positively biased relative to the lower electrode, the electric field compresses the AlN layer vertically via the piezoelectric effect, and the mechanical strain propagates into the optical waveguide, increasing the refractive index via the photo-elastic effect (Tian, J. Liu, Attanasio, et al., 2024). This, in turn, decreases the resonance frequency of the ring. Similarly, the resonance frequency increases when the electrodes are negatively biased, enabling bidirectional, linear tuning with AlN actuators. Stress and force distribution upon piezoelectric tuning was simulated using COMSOL (Figure 6.3b). In this plot, the top electrode of the AlN actuator is positively biased, and the cross-section of the structure is presented. The color denotes the stress tensor σ_{xx} (Tian, J. Liu, Attanasio, et al., 2024) (blue implies compression while red implies expansion), and the arrows denote the stress-induced mechanical force.

In general, monolithically integrated piezoelectric actuators offer >MHz-level control of photonic circuits and resonators (Tian, J. Liu, Attanasio, et al., 2024; W. Jin, Polcawich, et al., 2018; J. Wang et al., 2022; M. Dong et al., 2022). This is also experimentally measured for our device (Figure 6.3c). Previously demonstrated applications include ranging (LiDAR) and quantum optics (Tian, J. Liu, Bin Dong, et al., 2020; J. Liu et al., 2020; Lihachev et al., 2022; Brydges et al., 2023), and they outperform hybrid-integrated actuators in mass production (Dale et al., 2014).

In our work, AlN piezoelectric actuators are fabricated based on the procedure in Figure 6.4. The resonators feature an intrinsic Q factor greater than 100 million at 1550 nm (the highest Q factor for devices with integrated piezoelectric actuators, to

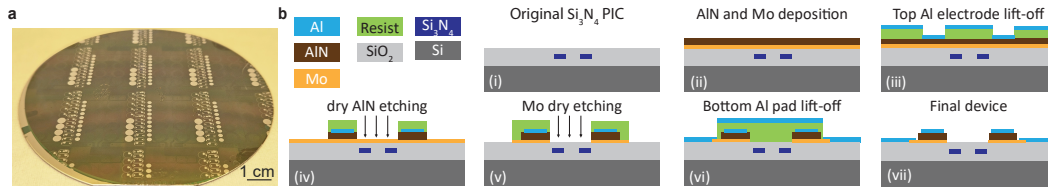


Figure 6.4: Detailed AlN piezoelectric tuner fabrication process. **a**, Photograph of the fabricated 4-inch wafer. **b**, Illustration of the fabrication process. (i) The process starts with the foundry-based Si_3N_4 ultra-low-loss circuit on an 8-inch wafer, followed by chemical-mechanical polishing (CMP) to planarize the top silica cladding. After the wafer is cored to 4-inch wafers, alignment markers are then etched on the silica cladding using dry etch with Al hard masking. (ii) 100 nm of Mo (which lately serves as the bottom electrode) and 1 μm of AlN are deposited at an external foundry (AMSystems). (iii) 100 nm of Al is deposited via e-beam evaporation and lift-off is performed to define the top electrode. (iv) The AlN layer is plasma etched using a combination of Cl_2 and Ar. (v) The AlN layer is plasma etched using a combination of Cl_2 and O_2 . (vi) Additional Al pads connected with the bottom Mo electrodes are fabricated with same process in (iii) to enable wire bonding (since the Mo electrode is usually not able to be ultrasonic wire-bonded). (vii) The wafer is baked at 250 $^\circ\text{C}$ for ~ 50 hours to mitigate the induced additional optical propagation loss during the lithography processes (Guo, Xiang, et al., 2024; X. Ji et al., 2024).

our knowledge (J. Liu et al., 2020; Lihachev et al., 2022).

In constituting the OFD system, the AlN tuners have three advantages: (1) The fabrication is based on monolithic integration with high-fidelity, and at low temperature ($< 450^\circ\text{C}$); (2) The light remains in the Si_3N_4 layer with low propagation loss, and no worry of insertion loss between different waveguides; (3) Reasonably high tuning control bandwidth is presented (MHz level).

Piezoelectric control of the reference laser

The Pound–Drever–Hall (PDH) technique generally requires frequency tuning (quasi-DC) and MHz-rate phase modulation of an optical signal to achieve locking. Integrating these optical components onto a photonic chip reduces operational complexity and facilitates scalable system production (Idjadi and Aflatouni, 2017). Here, we demonstrate a high-performance and CMOS-ready system for PDH locking. The device uses a high- Q Si_3N_4 resonator functionalized with piezoelectric actuation to both frequency tune and phase modulate a hybridly-integrated DFB laser for PDH locking to a high-finesse Fabry–Pérot reference cavity.

The III-V DFB laser is self-injection locked (SIL) to the high- Q Si_3N_4 ring res-

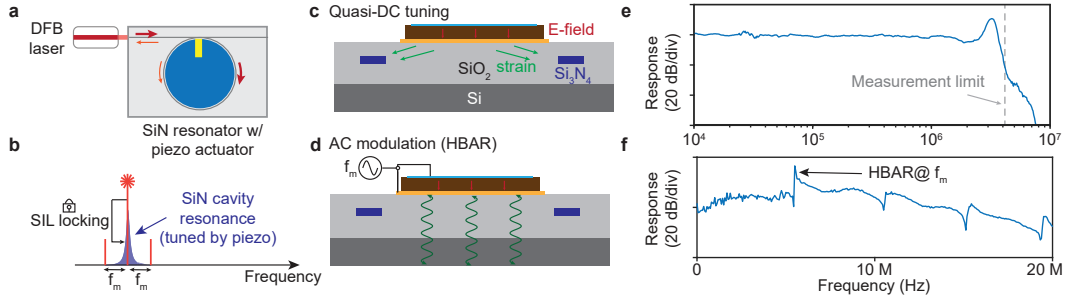


Figure 6.5: Piezoelectric DC tuning and AC modulation of the self-injection locked laser. **a**, Schematic of a III-V DFB laser self-injection locked (SIL) to a high- Q Si_3N_4 resonator with AlN piezoelectric tuner atop. A portion of incident laser light (red arrow) is back-scattered (orange arrow) inside the ring resonator to the laser. **b**, SIL operation stabilizes the laser to the Si_3N_4 ring resonance which is frequency tunable via piezoelectric tuning. Simultaneous AC piezoelectric modulation at f_m creates two frequency modulated sidebands. **c**, Cross section of the chip showing how near-DC piezoelectric tuning modifies the Si_3N_4 ring resonance via mechanical strain. **d**, AC piezoelectric modulation at f_m excites a high-overtone bulk acoustic resonance (HBAR) for optical phase modulation. **e**, Frequency tuning of the SIL laser achieves > 1 MHz response bandwidth. **f**, An HBAR resonance is observed near 5.6 MHz.

onator (Figure 6.5a) (Lihachev et al., 2022). Under SIL operation the laser's output frequency closely tracks a resonant frequency of the ring resonator. Moreover, the laser's frequency noise is reduced (Liang et al., 2010). The piezoelectric tuners made from aluminum nitride (AlN) are monolithically integrated with the Si_3N_4 resonator (Figure 6.5c-d). They provide fast tuning (from DC to > 1 MHz) of the resonator (and in turn the DFB laser) via the photoelastic effect (Figure 6.5b). In addition, the semiconductor chip supports a high-overtone bulk acoustic resonance (HBAR) making possible strong piezoelectric modulation at high resonant frequencies f_m with a CMOS-compatible modulation voltage (Tian, J. Liu, Bin Dong, et al., 2020) (Figure 6.5d). This provides phase modulation at f_m to create the PDH optical sidebands (Figure 6.5b). In Figure 6.5e, the frequency tuning response of the SIL laser under resonator piezoelectric tuning control is characterized and shows > 1 MHz bandwidth. And in Figure 6.5f, an HBAR acoustic resonance at 5.6 MHz is identified for generation of the PDH sideband.

The PDH locking setup is shown in Figure 6.6a with the laser and resonator photographed in Figure 6.6b. The AC modulation for the PDH error signal generation and the DC actuation for PDH locking are implemented in a single AlN actuator. A radio-frequency tone at the HBAR frequency f_m is directed to the AC input of a

bias tee and applied to the piezoelectric tuner. This generates two phase-modulated sidebands separated from the carrier by f_m (as in Figure 6.5b). A frequency tuning signal is simultaneously applied to the AlN chip via the DC port of the bias tee. On account of SIL operation, the frequency of the DFB laser tracks the Si_3N_4 resonator mode as it is tuned by the mechanical strain induced from the piezoelectric actuator.

The output of the laser-chip assembly is coupled to a high-finesse Fabry–Pérot cavity with > 8 billion Q factor. The signal reflected from the Fabry–Pérot cavity is detected by an avalanche photodetector (APD), where it is mixed with the modulation drive signal at f_m . As illustrated in the upper panel of Figure 6.6c, the modulated laser is frequency swept across the Fabry–Pérot cavity mode with a ramp signal applied to the DC tuning port of the AlN actuator. The generated PDH signal is recorded using an oscilloscope, and plotted in the lower panel of Figure 6.6c. The three zero-crossings (dashed red lines) correspond to the right sideband, the carrier, and the left sideband. PDH locking is engaged by replacing the ramp signal with the output of a servo (Figure 6.6a).

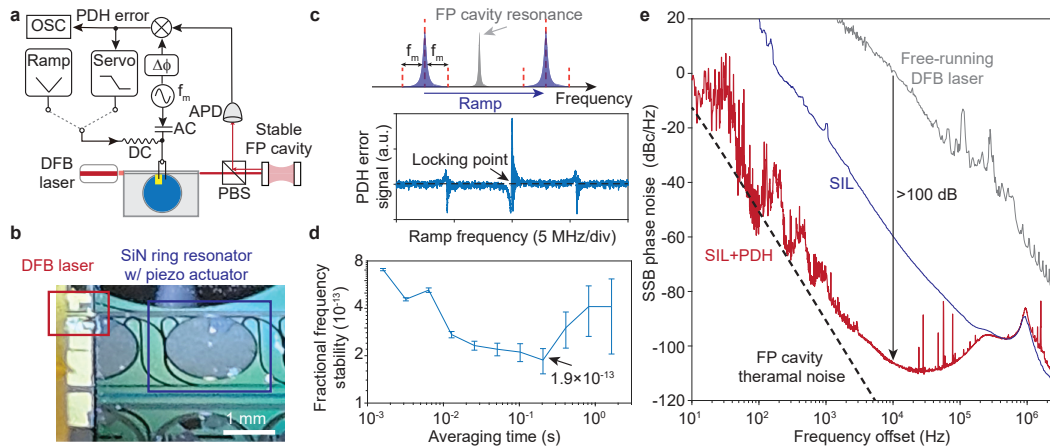


Figure 6.6: PDH locking the SIL laser to an optical reference via integrated piezoelectric tuning and modulation. **a**, Experimental setup. **b**, Photograph showing the SIL laser with AlN piezoelectric control. **c**, Tuning the frequency-modulated SIL laser across a the Fabry–Pérot cavity resonance (illustrated in upper panel) to observe the PDH signal (lower panel). **d**, Allan deviation results. Fractional frequency stability reaches 1.9×10^{-13} at an averaging time of 200 ms. A linear drift of 800 Hz/s has been removed (error bar denotes standard deviation). **e**, Phase noise characterization.

The performance of the system is characterized by beating the PDH-locked laser with another stable reference laser. The beatnote is then studied in time and frequency domains. A fractional frequency stability (Allan deviation) of 1.9×10^{-13} is attained

(Figure 6.6d), which is comparable to a previous result using conventional PDH locking hardware (W. Zhang et al., 2024). Phase noise results are summarized in Figure 6.6e. Phase noise of the locked laser (solid red line) is in line with the thermal noise floor of the reference cavity (dashed black line) at low offset frequencies. For comparison, the SIL laser phase noise without PDH locking (blue), and the phase noise of the free-running DFB laser are plotted (gray). At 10 kHz offset frequency, over 100 dB of phase noise reduction relative to the free-running DFB laser is measured for the PDH-locked SIL laser. Therefore, high-performance PDH locking is achieved in an integrated form, which shows compact size, robustness, and low cost.

Piezoelectric locking of microcomb

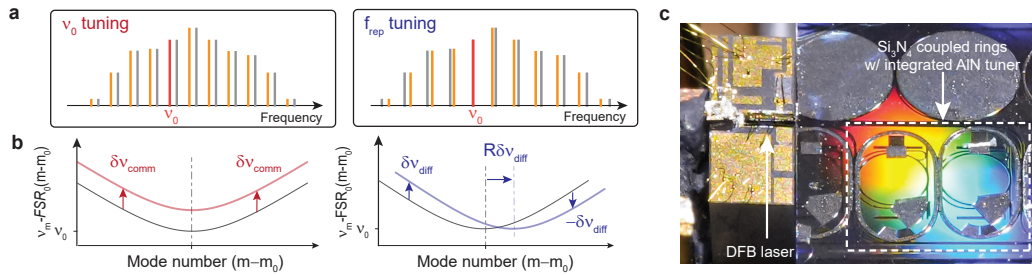


Figure 6.7: Integrated separable tuning of microcomb offset and repetition rate. **a**, Illustration of the two degrees of frequency control required for comb operation: offset frequency on left and repetition rate on right. **b**, Common mode and differential mode tuning control in a vernier-coupled-ring resonator. Illustration of integrated dispersion plotted versus relative mode number ($m - m_0$). The mode number m_0 corresponds to a degeneracy frequency of the rings. Left: common-mode tuning induces a vertical frequency shift of the dispersion curve by δv_{comm} so that the optical resonance $\nu_0 \rightarrow \nu_0 + \delta v_{\text{comm}}$. Right: differential-mode tuning shifts the dispersion curve laterally causing the FSR to tune, but having no effect on ν_0 . This dispersion shift is magnified by the Vernier factor R , enhancing the rate of tuning of the FSR. Integrated dispersion is given by: $\nu_m - FSR_0(m - m_0) = \nu_0 + (D_{2c}/2\pi)(m - m_0)^2/2 + \dots$ where ν_0 , FSR_0 , D_{2c} are mode frequency, FSR, and second-order dispersion (only the resonator coupling contribution) at mode m_0 . **d**, Photograph of the resonator with piezoelectric actuators and self-injection-locked DFB laser pump.

The piezoelectric locked microcomb features improved tuning bandwidth, as well as separable control of offset frequency and repetition rate, using a common/differential-mode frequency-tuning control in coupled-ring resonators (illustrated in Figure 6.7a,b). Resultantly, full frequency stabilization of the microcomb is achieved. To

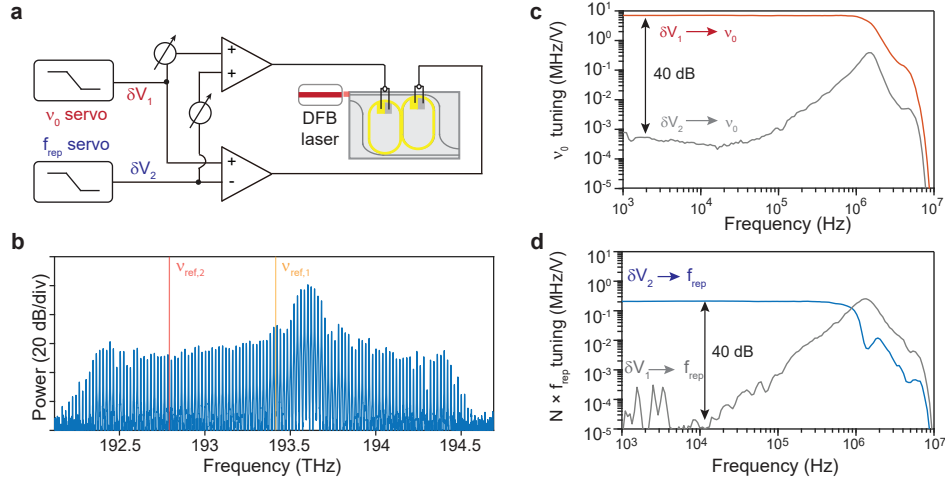


Figure 6.8: Differential and common mode piezoelectric tuning of the coupled ring resonator. **a**, Circuit for generation of control signals from servo voltages δV_1 and δV_2 for common mode and differential mode tuning ν_0 and f_{rep} . **b**, Optical spectrum of the normal dispersion microcomb (blue). Two reference lasers are depicted at frequencies $\nu_{\text{ref},1}$ and $\nu_{\text{ref},2}$. **c**, Measured tuning response for ν_0 when δV_1 (red) and δV_2 (gray) are modulated. The tuning crosstalk is suppressed by > 40 dB. **d**, Measured tuning response for f_{rep} when δV_1 (gray) and δV_2 (blue) are modulated. The tuning crosstalk is suppressed by > 40 dB.

emphasis, the bandwidth is more than 10 times larger than the previous result using DFB laser current modulation (Figure 2.5).

For further details, the free-spectral-range (FSR) of the rings is designed to be slightly different ($\Delta FSR = 70$ MHz with an average $\overline{FSR} = 19.95$ GHz) to create a frequency Vernier in the coupling of resonator modes. This Vernier enables wide-band tuning of the resonator dispersion through the Moiré speed-up effect (Q.-X. Ji, P. Liu, et al., 2024). Furthermore, differentially tuned resonators not only achieve this Moiré-enhanced dispersion tuning, but have negligible offset frequency tuning. This ability of the Moiré speed-up effect to isolate tuning control has not been previously recognized, and it enables separable control of comb offset frequency and repetition rate.

Tuning of optical frequency and FSR at $m = m_0$ (i.e., ν_0 and FSR_0) is accomplished using piezoelectric actuation. The tuning is governed by the following matrix,

$$\begin{pmatrix} \delta \nu_0 \\ \delta FSR_0 \end{pmatrix} = \frac{1}{m_0} \begin{pmatrix} m_0 & 0 \\ 1 & -\Gamma \end{pmatrix} \begin{pmatrix} \delta \nu_{\text{comm}} \\ \delta \nu_{\text{diff}} \end{pmatrix} \quad (6.1)$$

where $\Gamma \equiv (m_0 D_{2c} R) / (2\pi \overline{FSR})$, and where: $m_0 \approx 9670$ and $D_{2c} / 2\pi = 278$ kHz.

The wavelength location of m_0 and the value of \overline{FSR} are determined by dispersion measurement, where $\Gamma = 39$. Moreover, direct measurement of FSR tuning gives $\Gamma = 39 \pm 4$, which compares well with the above value.

Separable tuning control therefore results from the off-diagonal elements in the above matrix being zero or small compared to the diagonal elements. Moreover, as noted below, the presence of the zero in this matrix means that fully independent control is possible (i.e., matrix diagonalized) by simple adjustment of the scale factor in control of common and differential servo signals. Finally, the value of m_0 is broadly tunable (over L, C and S bands) by differential thermal tuning of the rings so that matching of m_0 to a desired operating wavelength is straightforward (Q.-X. Ji, P. Liu, et al., 2024).

Convenient generation of common-mode and differential voltage signals for the piezoelectric actuators is possible using the circuit shown in Figure 6.8a. Servos for control of ν_0 and FSR generate voltages δV_1 and δV_2 , which are coupled to sum and difference circuits and subsequently amplified by ~ 2 times to increase the gain in the servo loop. To test the system, the microcomb is pumped by a commercial DFB laser (Emcore Corporation, with 120 mW output at 1548 nm) under the self-injection-locked operation. The comb has a ~ 20 GHz repetition rate and ~ 2 THz span. Despite the anomalous dispersion provided by resonator coupling, the overall dispersion is slightly normal on account of the waveguide dispersion contribution. The comb spectrum is shown in Figure 6.8b. Operation as a anomalous dispersion comb is also possible by adjusting the frequency Vernier (Yuan et al., 2023).

Microcomb frequency control bandwidth

To test the frequency response of the separable control system, reference lasers at frequencies $\nu_{\text{ref},1}$, $\nu_{\text{ref},2}$ are used as illustrated in Figure 6.8b. These lasers are separately frequency locked to a high-stability Fabry–Pérot cavity (described in the next section). $\delta V_{1,2}$ are then modulated to induce modulation in ν_0 and FSR, which, in turn, modulate the microcomb offset frequency and repetition rate f_{rep} . To measure tuning frequency response, the reference lasers are combined with the comb light and photodetected to provide beat frequency signals with nearby comb teeth. For this measurement, one of the reference laser frequencies ($\nu_{\text{ref},1}$) is close in frequency to a mode crossing point (at m_0) so the corresponding response to modulation (δV_1) reflects mainly offset frequency variation (Figure 6.8c). The other reference laser frequency ($\nu_{\text{ref},2}$) is many comb teeth away from the crossing point.

Its beatnote with a nearby comb tooth will be sensitive to FSR modulation induced by δV_2 . This modulation is also multiplied by the number of comb teeth (N) relative to the crossing mode (Figure 6.8d). To test isolation of f_{rep} when offset frequency is intentionally modulated (gray data in Figure 6.8e) the two beatnotes are electrically mixed to eliminate the optical carrier frequency in the response measurement.

In each case, the independence of the control can also be tested by measuring the cross-talk frequency response to the alternate control voltage. To minimize this cross talk, the ratios of the sum and difference of the voltages in Figure 6.8a can be fine-tuned. Experimentally, the cross-talk is suppressed by >40 dB (Figure 6.8c,d).

Finally, it is noted that the bandwidth (3-dB bandwidth ≈ 1 MHz) in these measurements is limited by cable-induced delays in the experiment. A direct measurement of the pure piezo response (see Figure 6.3c) shows that the intrinsic response ≈ 10 MHz. Tighter integration of the control circuits with the microcomb would enable access to this full control bandwidth. It is also noted that the self-injection locking process introduces a phase delay that can potentially limit bandwidth. Importantly, the bandwidth is more than 10 times larger than the previous result using DFB laser current modulation (Figure 2.5).

Microcomb full frequency stabilization

Full frequency stabilization of the microcomb using the separable control approach is illustrated in Figure 6.9a. The reference lasers (RIO laser at 1550 nm and Toptica laser at 1555 nm) are stabilized to a high- Q Fabry–Pérot cavity by the Pound-Drever-Hall (PDH) locking technique (W. Zhang et al., 2024). The microcomb frequency (ν_0) is locked to the RIO laser ($\nu_{\text{ref},1}$ near the mode crossing point) by feedback to the actuators under common mode tuning. The repetition rate (f_{rep}) is stabilized using the 2P-OFD by feeding back to actuators under differential mode. Division of this span by $N = 31$ transfers the reference cavity stability into the microcomb repetition rate (f_{rep}). The choice of the laser operation frequencies ($\nu_{\text{ref},1}, \nu_{\text{ref},2}$) is currently limited by the available lasers and optical filters.

Characterization of the stabilized ν_0 and f_{rep} is presented in Figure 6.9b-e. The electrical spectra (resolution bandwidth is 10 Hz) of the beatnote between the reference laser ν_1 and comb line ν_0 and the detected microcomb repetition rate are presented in Figures 6.9b-c, respectively. These spectra verify full frequency stabilization of the microcomb to the reference cavity. Further evidence of the full stabilization is provided in Figures 6.9d-e, which give the corresponding phase noise

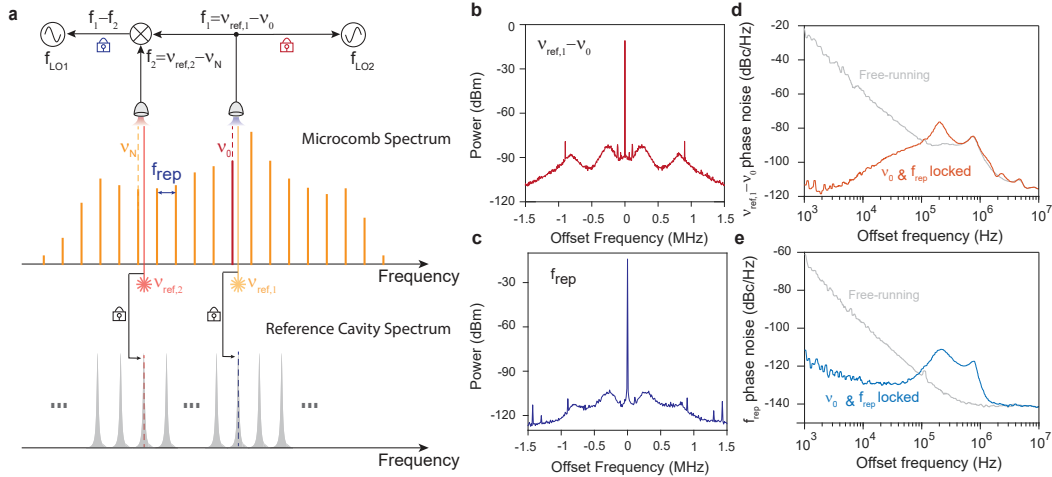


Figure 6.9: Microcomb frequency stabilization. **a**, Illustration of stabilization of f_{rep} and ν_0 . Two lasers (frequencies: $\nu_{\text{ref},1}$ and $\nu_{\text{ref},2}$) are stabilized to two modes of the same Fabry-Pérot cavity (gray spectrum). Comb lines at ν_0 and ν_N are locked to these lasers by first generating photodetector beatnotes ($f_1 = \nu_{\text{ref},1} - \nu_0$, $f_2 = \nu_{\text{ref},2} - \nu_N$). ν_0 is then locked by locking f_1 to the local oscillator at $f_{\text{LO}2}$ by servo control of the common-mode tuning actuator. To lock ν_N , intermediate frequency $f_1 - f_2 = (\nu_{\text{ref},1} - \nu_{\text{ref},2}) - N f_{\text{rep}}$ is produced and locked to $f_{\text{LO}1}$ by servo control of the differential actuator. This also stabilizes the comb repetition rate (f_{rep}) by 2-point optical frequency division of the laser spacing ($\nu_{\text{ref},1} - \nu_{\text{ref},2}$). **b**, The electrical spectrum (RBW 10 Hz) of the stabilized beat note between reference laser 1 and the comb ($f_1 = \nu_{\text{ref},1} - \nu_0$). **c**, The electrical spectrum (RBW 10 Hz) of the stabilized comb repetition rate f_{rep} . **d**, Phase noise spectra of the stabilized beat note between reference laser 1 and the comb when the microcomb is free-running (gray) and frequency-stabilized (red). **e**, Phase noise spectra of the f_{rep} when the microcomb is free-running (gray) and frequency-stabilized (blue).

spectra for the measurements in Figures 6.9b and c. The phase noise spectra for the free-running (gray) and locked (red, blue) microcomb cases are measured. The locking bandwidths for the two phase locking loop are ~ 100 kHz with locking corner frequencies located ~ 200 kHz. The higher corner frequencies (~ 1 MHz) are from the reference laser PDH locks. The locked microcomb exhibits low phase noise levels: at 10 kHz offset frequency, the beatnote $\nu_0 - \nu_{\text{ref},1}$ attains -106 dBc/Hz (optical rate ≈ 193.4 THz), and f_{rep} attains -130 dBc/Hz (carrier frequency ~ 19.95 GHz). By increasing the phase noise division factor, lower phase noise for microwave generation is possible (Q.-X. Ji, W. Zhang, Savchenkov, et al., 2025).

6.4 Conclusion of the thesis

What has been done?

This thesis presents a study of chip-based optical frequency division (OFD) using high- Q integrated photonic devices. Motivated by developing a microcomb that fits into the OFD experiment, the key focus is placed on dispersion engineering using coupled ring resonators. The development of Vernier two-ring (2CR) and three-ring (3CR) architectures enables precise and programmable control over both second- and third-order dispersion. These advances allow for the generation microcombs with wide spectral bandwidth and improved efficiency. Resultantly, a photonic-chip-based OFD system with lowest phase noise for microwave generation among those using integrated photonics, is demonstrated.

The thesis also demonstrates system-level progress toward a compact, robust OFD device. Stable self-injection locking of microcombs to integrated III-V lasers is achieved and characterized. Early efforts to incorporate piezoelectric tuning elements monolithically into the photonic platform have shown success in stabilizing both reference lasers and comb sources. Together, these developments establish a viable path toward scalable, low-SWaP, and fully integrated OFD systems with broad relevance for precision timing, frequency synthesis, and spectroscopy.

What is next?

The photonic chip-based OFD assembly

A fully integrated OFD system on chip remains a compelling vision, though it continues to pose significant engineering challenges. This thesis has demonstrated functional integration of critical subsystems, including high- Q comb generators, reference lasers, and hybrid III-V pumping, yet assembling all required elements onto a single silicon substrate remains elusive. Issues such as thermal crosstalk, heterogeneous material bonding, waveguide routing, and wafer-level process compatibility must be addressed. Intermediate architectures based on hybrid assembly and co-packaging offer practical paths forward. The creation of modular, portable OFD systems that blend performance with manufacturability is expected.

A number of sub-components in the photonic chip-based OFD assembly may also find usage individually. For example, miniaturized stable lasers and frequency comb sources are generally useful for a wide range of applications.

New material platforms?

Every leap of integrated photonics is engined by a new material platform, especially the boosted Q factor for microresonators. The emergence of the low-loss Si_3N_4 was pivotal in enabling microcombs and narrow-linewidth lasers, thus the OFD for this thesis.

Germano-silicate glasses, commonly used in optical fibers, are emerging as candidates for planar integration. Their compatibility with CMOS backends remains a technical hurdle, but advances in low-temperature deposition and hybrid photonic platforms may help bridge that gap (Chen et al., 2024).

MgF_2 and CaF_2 , though not easily integrated with standard lithographic processes, feature the highest Q factors among known microresonator materials. Their exceptional transparency from the ultraviolet to the mid-infrared, along with ultra-low absorption and scattering losses, make them ideal for applications requiring extreme coherence, such as optical atomic clocks and ultra-low-noise microwave generation. As micro-machining, polishing, and bonding techniques continue to evolve, hybrid $\text{MgF}_2/\text{CaF}_2$ on-chip integration may become feasible for specialized high-performance systems. These materials are also gaining attention as potential host media for the ^{229}Th nuclear transition, offering a path toward cavity-enhanced nuclear spectroscopy and new frontiers in precision timekeeping and fundamental physics (Tiedau et al., 2024).

References

- Brydges, Tiff et al. (2023). “Integrated photon-pair source with monolithic piezoelectric frequency tunability.” In: *Physical Review A* 107.5, p. 052602.
- Chen, Hao-Jing et al. (2024). “Germano-silicate ultra-low loss photonic integrated circuits across visible and near-infrared spectrum.” In: *2024 Conference on Lasers and Electro-Optics (CLEO)*. IEEE, pp. 1–2.
- Cheng, Haotian et al. (2023). “A novel approach to interface high- Q Fabry–Pérot resonators with photonic circuits.” In: *APL Photonics* 8.11.
- Dale, Elijah et al. (2014). “Ultra-narrow line tunable semiconductor lasers for coherent LIDAR applications.” In: *Imaging Systems and Applications*. Optica Publishing Group, JTU2C–3.
- Dong, Mark et al. (2022). “High-speed programmable photonic circuits in a cryogenically compatible, visible–near-infrared 200 mm CMOS architecture.” In: *Nature Photonics* 16.1, pp. 59–65.

- Endo, Mamoru and Thomas R. Schibli (2018). “Residual phase noise suppression for Pound-Drever-Hall cavity stabilization with an electro-optic modulator.” In: *OSA Continuum* 1.1, pp. 116–123.
- Groman, William et al. (2024). “Photonic millimeter-wave generation beyond the cavity thermal limit.” In: *Optica* 11.11, pp. 1583–1587.
- Guo, Joel, Charles A. McLemore, et al. (2022). “Chip-based laser with 1-hertz integrated linewidth.” In: *Science Advances* 8.43, eabp9006.
- Guo, Joel, Chao Xiang, et al. (2024). “Investigation of Q degradation in low-loss Si₃N₄ from heterogeneous laser integration.” In: *Optics Letters* 49.16, pp. 4613–4616.
- Idjadi, Mohamad Hossein and Firooz Aflatouni (2017). “Integrated Pound-Drever-Hall laser stabilization system in silicon.” In: *Nature Communications* 8.1, p. 1209.
- Ji, Qing-Xin, Warren Jin, et al. (2023). “Engineered zero-dispersion microcombs using CMOS-ready photonics.” In: *Optica* 10.2, pp. 279–285.
- Ji, Qing-Xin, Peng Liu, et al. (2024). “Multimodality integrated microresonators using the Moiré speedup effect.” In: *Science* 383.6687, pp. 1080–1083.
- Ji, Qing-Xin, Wei Zhang, Anatoliy A. Savchenkov, et al. (2025). “Dispersive-wave-agile optical frequency division.” In: *Nature Photonics*.
- Ji, Qing-Xin, Wei Zhang, Lue Wu, et al. (2024). “Coherent optical-to-microwave link using an integrated microcomb.” In: *IEEE Journal of Selected Topics in Quantum Electronics*.
- Ji, Xinru et al. (2024). “Efficient mass manufacturing of high-density, ultra-low-loss Si₃N₄ photonic integrated circuits.” In: *Optica* 11.10, pp. 1397–1407.
- Jin, Naijun et al. (2022). “Micro-fabricated mirrors with finesse exceeding one million.” In: *Optica* 9.9, pp. 965–970.
- Jin, Warren, Ronald G Polcawich, et al. (2018). “Piezoelectrically tuned silicon nitride ring resonator.” In: *Optics Express* 26.3, pp. 3174–3187.
- Jin, Warren, Qi-Fan Yang, et al. (2021). “Hertz-linewidth semiconductor lasers using CMOS-ready ultra-high-Q microresonators.” In: *Nature Photonics* 15.5, pp. 346–353.
- Kudelin, Igor et al. (2024). “Photonic chip-based low-noise microwave oscillator.” In: *Nature* 627.8004, pp. 534–539.
- Kwon, Dohyeon et al. (2022). “Ultrastable microwave and soliton-pulse generation from fibre-photonic-stabilized microcombs.” In: *Nature Communications* 13.1, p. 381.
- Li, Bohan et al. (2021). “Reaching fiber-laser coherence in integrated photonics.” In: *Optics Letters* 46.20, pp. 5201–5204.

- Liang, Wei et al. (2010). “Whispering-gallery-mode-resonator-based ultranarrow linewidth external-cavity semiconductor laser.” In: *Optics Letters* 35.16, pp. 2822–2824.
- Lihachev, Grigory V. et al. (2022). “Low-noise frequency-agile photonic integrated lasers for coherent ranging.” In: *Nature Communications* 13.1, p. 3522.
- Liu, Junqiu et al. (2020). “Monolithic piezoelectric control of soliton microcombs.” In: *Nature* 583.7816, pp. 385–390.
- Liu, Yang et al. (2022). “A photonic integrated circuit-based erbium-doped amplifier.” In: *Science* 376.6599, pp. 1309–1313.
- Liu, Yifan et al. (2024). “Ultrastable vacuum-gap Fabry–Perot cavities operated in air.” In: *Optica* 11.9, pp. 1205–1211.
- McLemore, Charles A. et al. (2022). “Miniaturizing ultrastable electromagnetic oscillators: Sub-10- 14 frequency instability from a centimeter-scale Fabry–Pérot cavity.” In: *Physical Review Applied* 18.5, p. 054054.
- Newman, Zachary L. et al. (2019). “Architecture for the photonic integration of an optical atomic clock.” In: *Optica* 6.5, pp. 680–685.
- Papp, Scott B. et al. (2014). “Microresonator frequency comb optical clock.” In: *Optica* 1.1, pp. 10–14.
- Savchenkov, Anatoliy A. et al. (2024). “Robust self-injection locking to a non-confocal monolithic Fabry–Perot cavity.” In: *Optics Letters* 49.6, pp. 1520–1523.
- Shen, Boqiang et al. (2020). “Integrated turnkey soliton microcombs.” In: *Nature* 582.7812, pp. 365–369.
- Tian, Hao, Junqiu Liu, Alaina Attanasio, et al. (2024). “Piezoelectric actuation for integrated photonics.” In: *Advances in Optics and Photonics* 16.4, pp. 749–867.
- Tian, Hao, Junqiu Liu, Bin Dong, et al. (2020). “Hybrid integrated photonics using bulk acoustic resonators.” In: *Nature Communications* 11.1, p. 3073.
- Tiedau, Johannes et al. (2024). “Laser excitation of the Th-229 nucleus.” In: *Physical Review Letters* 132.18, p. 182501.
- Wang, Jiawei et al. (2022). “Silicon nitride stress-optic microresonator modulator for optical control applications.” In: *Optics Express* 30.18, pp. 31816–31827.
- Xiang, Chao, Warren Jin, et al. (2023). “3D integration enables ultralow-noise isolator-free lasers in silicon photonics.” In: *Nature* 620.7972, pp. 78–85.
- Xiang, Chao, Junqiu Liu, et al. (2021). “Laser soliton microcombs heterogeneously integrated on silicon.” In: *Science* 373.6550, pp. 99–103.
- Xie, Weiqiang et al. (2019). “Heterogeneous silicon photonics sensing for autonomous cars.” In: *Optics Express* 27.3, pp. 3642–3663.

- Yuan, Zhiquan et al. (2023). “Soliton pulse pairs at multiple colours in normal dispersion microresonators.” In: *Nature Photonics* 17.11, pp. 977–983.
- Zang, Jizhao et al. (2018). “Reduction of amplitude-to-phase conversion in charge-compensated modified untraveling carrier photodiodes.” In: *Journal of Lightwave Technology* 36.22, pp. 5218–5223.
- Zhang, Wei et al. (2024). “Monolithic optical resonator for ultrastable laser and photonic millimeter-wave synthesis.” In: *Communications Physics* 7.1, p. 177.

Appendix A

THEORY OF KERR MICROCOMBS

This chapter presents theoretical frameworks for modeling Kerr soliton microcombs, emphasizing physical understanding and numerical accessibility. We begin with the Lugiato-Lefever equation (LLE), which forms the basis for describing dissipative solitons in microresonators. Its use is illustrated in modeling the spectral properties of microcombs near-zero group velocity dispersion (GVD) (Ji et al., 2023). Next, an eigenmode approach is introduced to study the physics of breather solitons and their excitation spectrum. Finally, we then apply a Lagrangian method to analyze the dynamics of cavity solitons under pulsed optical pumping (J. Li et al., 2022).

A.1 Introduction: The Lugiato-Lefever equation

The Lugiato-Lefever equation (LLE) (Lugiato and Lefever, 1987) is a widely used model for describing nonlinear dynamics in driven Kerr cavities. Its introduction to microresonator frequency combs by Chembo and Menyuk (Chembo and Menyuk, 2013) established a framework for studying temporal soliton formation in chip-scale devices.

The LLE describes the evolution of the intracavity field envelope $E(\theta, T)$, where θ is the azimuthal coordinate around the resonator (from 0 to 2π), and T is the slow time describing evolution over many round trips. The equation is written as:

$$\frac{\partial}{\partial T} E(\theta, T) = \left(-\frac{\kappa}{2} - i\delta\omega + ig |E(\theta, T)|^2 + \sum_{j \geq 2} (-i)^{(j+1)} \frac{D_j}{j!} \frac{\partial^j}{\partial \theta^j}\right) E(\theta, T) + E_{\text{in}}, \quad (\text{A.1})$$

where κ is the cavity linewidth, $\delta\omega = \omega_L - \omega_C$ is the laser-cavity detuning, g is the Kerr nonlinear coefficient, D_j are the dispersion parameters, and $f = \sqrt{\kappa_{\text{ext}} P_{\text{in}} / \hbar \omega_0}$ is the pump input (κ_{ext} is the pump bus waveguide coupling rate, P_{in} is the pump power on the bus waveguide in Watt, \hbar is the reduced Planck constant, $\omega_0/2\pi$ is the pump laser frequency).

By transforming to the fast time variable $t = -\theta/D_1$, the LLE becomes:

$$\frac{\partial}{\partial T} E(t, T) = \left(-\frac{\kappa}{2} - i\delta\omega + ig |E(t, T)|^2 + \sum_{j \geq 2} \left(\frac{i}{D_1}\right)^{(j+1)} \frac{D_j}{j!} \frac{\partial^j}{\partial t^j}\right) E(t, T) + E_{\text{in}}. \quad (\text{A.2})$$

Microcavity symbols Equation A.1	Optical fiber community symbols Equation A.3	Normalized Equation A.4
photon number $ E(\theta, T) ^2$	optical power $ A(t, T) ^2$	$ \psi(x, \tau) ^2$
slow time T	$z = \frac{LD_1}{2\pi}T$	$\tau = \kappa T/2$
cavity azimuthal axis θ	$t = -\frac{\theta}{D_1}$	θ
cavity linewidth κ	$\alpha = \frac{2\pi\kappa}{D_1L}$	1
laser-cavity detuning $\delta\omega$	$\delta k_0 = \frac{2\pi\delta\omega}{D_1L}$	$\Delta = \frac{2\delta\omega}{\kappa}$
Kerr coefficient g	$\gamma = \frac{4\pi^2\hbar\omega_0}{D_1^2L}g$	1
GVD parameter D_2	$\beta_2 = -\frac{D_2T_R}{D_1^2L}$	1
pump input E_{in}	$\frac{1}{L}\sqrt{\theta_c P_{\text{in}}}$	$h = \sqrt{\frac{P_{\text{in}}}{P_{\text{th}}}}$

Table A.1: **Conversion between different forms of LLEs.**

Other two forms of the LLE

Alternative Forms of the LLE

Different research communities often use different forms of the LLE. The second form of the LLE is generally from the fiber soliton community, reads

$$\frac{\partial}{\partial z}A(t, z) = \left(-\frac{\alpha}{2} - i\delta k_0 + i\gamma |A(t, z)|^2 + \sum_{j \geq 2} (i)^{(j+1)} \frac{k_j}{j!} \frac{\partial^j}{\partial t^j}\right)A(t, z) + \frac{1}{L}\sqrt{\theta_c P_{\text{in}}}, \quad (\text{A.3})$$

where $|A(t, z)|^2$ is the circulating power, α is the energy loss rate (in dB/m), γ is the Kerr nonlinear coefficient, β is the dispersion parameter, L is the round trip length, θ_c is the coupling ratio of the bus waveguide, and P_{in} is the bus waveguide pump power.

Finally, the normalized LLE is the easiest one to be manipulated mathematically and in coding,

$$\frac{\partial}{\partial \tau}\psi(x, \tau) = (-1 - i\Delta + i|\psi(x, \tau)|^2 + \sum_{j \geq 2} (-i)^{(j+1)} \frac{d_j}{j!} \frac{\partial^j}{\partial \theta^j})\psi(x, \tau) + h, \quad (\text{A.4})$$

with $d_j = \frac{2D_j}{\kappa}$. Other definition of parameters can be found in Table A.1.

Solitonic solution of the LLE in the anomalous dispersion regime

The most famous and neat solution of the LLE A.2 is the (single) soliton (by neglecting the higher order dispersion terms). It has an approximated ansatz of (Yi et al., 2016b; Guo et al., 2017; X. Li et al., 2018)

$$E(\theta, T) = B_s \text{Sech}\left(\frac{t}{t_s}\right) e^{i\phi_s} + E_b, \quad (\text{A.5})$$

with $B_s^2 = \frac{2\delta\omega}{g}(1 + \frac{5}{4}x)$, $t_s^2 D_1^2 = \frac{D_2}{2\delta\omega}(1 - \frac{1}{2}x)$, $\cos(\phi_s) = \frac{\kappa}{\pi|E_b|}\sqrt{\frac{2}{g\delta\omega}} \approx \frac{\kappa}{\pi f}\sqrt{\frac{2\delta\omega}{g}}$, and E_b is the trivial solution of Equation A.1. x is a correction fact under a finite pumping amplitude, and is denoted by $x^2 = \frac{\pi^2 g |E_b|^2 \delta\omega - 2\kappa^2}{2\delta\omega^2} \approx \frac{\pi^2 g f^2 - 2\kappa^2 \delta\omega}{2\delta\omega^3}$. Beyond which the soliton ceases to exist. This limit reflects the balance required between nonlinearity, detuning, and dissipation to support a stable soliton in the cavity.

Dark pulse solution of the LLE in the normal dispersion regime

In the regime of small but finite dispersion, the dark pulse can be interpreted as a pair of domain walls that connect two distinct stable steady states of the LLE: a high-power background and a low-power intermediate state. These two levels correspond to different CW solutions of the LLE and are separated by a phase slip and localized intensity drop. The spatial profile of the pulse includes canonical oscillatory tails on either side of the intensity dip, reflecting dispersive wave modulation near the domain wall interface (Wang et al., 2022). Such dark pulse states are stable in the normal GVD regime and can form either single-pulse or multi-pulse patterns.

A.2 Solving the LLE with the Split-Step Fourier Method

A widely used numerical approach for solving the LLE is the split-step Fourier method. This method efficiently handles the interplay between nonlinearity and dispersion by separating the linear and nonlinear components of the evolution equation and treating them in different domains. In this approach, the derivatives with respect to the azimuthal coordinate θ are computed in the Fourier domain, while the nonlinear Kerr term is evaluated in the time domain. The temporal evolution (in slow time T) is then carried out iteratively, either until a steady-state solution is reached or to observe transient dynamics such as soliton formation and breathing behavior.

Listing A.1 provides a MATLAB implementation based on the normalized LLE in Equation A.4. The code simulates the formation of bright dissipative Kerr solitons in the anomalous dispersion regime.

```

1 clc; clear
2 %% Parameters definition
3 dt = 1e-3; T_total = 100; M = floor(T_total/dt);
4 t = linspace(0, T_total, M);
5 N = 2048; k = fftshift(-N/2:N/2-1); theta = linspace(-pi, pi, N);
6 h = sqrt(13); d2 = 0.01; d3 = 0;
7 % Initialization
8 E = rand(1, N)*1e-3;

```

```

9 Deltaa_pool = linspace(-5, 20, M);
10 dispersion = d2*k.^2/2 + d3*k.^3/6;
11 Field = zeros(M/100, N); mm = 1;
12 %% LLE numerical
13 for m = 1 : M
14
15     Delta = Deltaa_pool(m);
16
17     E = fft(E);
18     E = exp(-1i*dispersion*dt/2).*E;
19     E = ifft(E);
20     E = exp((-1-1i*Delta+1i*abs(E).^2)*dt).*E + h*dt;
21     E = fft(E);
22     E = exp(-1i*dispersion*dt/2).*E;
23     E = ifft(E);
24     P(m) = sum(abs(E).^2)/N;
25
26     if mod(m, 100) == 0
27         Field(mm, :) = E; mm = mm + 1;
28     end
29
30 end
31 %% Plotting
32 figure
33 plot(theta/pi, abs(E), 'linewidth', 1);
34 xlabel('Azimuthal_angle_\theta_\(\pi)'); ylabel('Intensity_(a.u.)')
    ; box on;
35 figure
36 plot(fftshift(k), 10*log10(abs(fftshift(fft(E))).^2/N^2));
37 xlabel('Mode_number'); xlim([-100 100]); ylabel('Power_(dB)');
38 figure
39 pcolor(theta.', t(1:100:end).', abs(Field).^2); shading interp;
    colorbar; colormap jet;
40 xlabel('Azimuthal_angle_(rad)'); ylabel('Normalized_time');

```

Listing A.1: Solving the LLE with split-step Fourier method.

The split-step Fourier method offers several advantages: it is computationally efficient, conceptually intuitive, and closely mirrors experimental observations of Kerr comb dynamics. Moreover, the method is highly flexible and can be readily extended to include additional physical effects by modifying the LLE to incorporate new terms.

As a representative example, I present below a simulation of a near-zero-GVD microcomb under self-injection locking, following the approach described in Ji et al. (2023).

Modeling of near-zero-GVD microcomb under self-injection locking

The system begins with the LLE as in Equation A.4. Besides, for the self-injection locking, a backward-propagating field E_B should be modeled with the forward field E_F ,

$$\begin{aligned} \frac{\partial}{\partial t} E_F = & (-1 - i\Delta + d_1 \frac{\partial}{\partial \theta} + i \frac{d_2}{2} \frac{\partial^2}{\partial \theta^2} + \frac{d_3}{6} \frac{\partial^3}{\partial \theta^3} + i|E_F|^2 + 2i\overline{|E_B|^2}) E_F \\ & + i g_B \overline{E_B} + h, \end{aligned} \quad (\text{A.6})$$

where E_F is the normalized intra-cavity field, $d_1 = 2\delta\omega_{\text{rep}}/\kappa$ is the normalized repetition rate change, $\Delta = 2\delta\omega/\kappa$ is normalized detuning, $d_2 = 2D_2/\kappa$ is normalized second-order dispersion parameter, $d_3 = 2D_3/\kappa$ is normalized third-order dispersion parameter, g_B is normalized back-scattering parameter, $h = \sqrt{P_{\text{in}}/P_{\text{th}}}$ is the normalized pumping strength, where P_{in} is the pump power and P_{th} is the parametric threshold power. The back-scattered field E_B here is also described by the same equation,

$$\begin{aligned} \frac{\partial}{\partial t} E_B = & (-1 - i\Delta + d_1 \frac{\partial}{\partial \theta} + i \frac{d_2}{2} \frac{\partial^2}{\partial \theta^2} + \frac{d_3}{6} \frac{\partial^3}{\partial \theta^3} + i|E_B|^2 + 2i\overline{|E_F|^2}) E_B \\ & + i g_B \overline{E_F}. \end{aligned} \quad (\text{A.7})$$

In addition, the laser-cavity detuning Δ under the self-injection is described by (Jin et al., 2021)

$$\Delta = \Delta_L + K \text{Im} \left[e^{i\psi} \frac{\overline{E_B}}{h} \right], \quad (\text{A.8})$$

where Δ_L is the normalized laser-cavity detuning without the feedback, K is the feedback strength, and ψ is feedback phase. The MATLAB code is in Listing A.2.

```

1 clc
2 clear
3 %% Parameters
4 kappa = 7.2e6*2*pi;
5 dt = 1e-3; T_total = 100; M = floor(T_total/dt);
6 t = linspace(0, T_total, M);
7 N = 2048; k = fftshift(-N/2:N/2-1); theta = linspace(-pi, pi, N);
8 gB = 0.1; psi = -pi/6; K = 2700; % SIL parameters
9 h = sqrt(13);

```

```

10 d1 = zeros(M, 1); d2 = 13e3*pi^2/kappa^2; d3 = 7e3*pi^2/kappa^2;
11 E = rand(1, N)*1e-3 + sech(theta/pi/1.5);
12 EB = rand(1, N)*1e-3 + sech(theta/pi/1.5);
13 Delta_pool = linspace(10, 10, M);
14 dispersion = d2*k.^2/2 + d3*k.^3/6;
15 Field = zeros(M/100, N);
16 mm = 1;
17 %% LLE numerical
18 for m = 1 : M
19
20     x(m) = (sum(abs(E).^2.*theta))/(sum(abs(E).^2)); d1(m) = x(m);
21
22     Delta_L = Delta_pool(m);
23     Delta = Delta_L + K*imag(exp(1i*psi)*mean(EB)/h);
24     Delta_SIL(m) = Delta;
25
26     E = fft(E);
27     E = exp(1i*(d1(m)*k-dispersion)*dt/2).*E;
28     E = ifft(E);
29     E = exp((-1-1i*Delta+1i*abs(E).^2 + 2*1i*mean(abs(EB).^2))*dt)
        .*E ...
30         + 1i*gB*mean(EB)*dt + h*dt;
31     E = fft(E);
32     E = exp(1i*(d1(m)*k-dispersion)*dt/2).*E;
33     E = ifft(E);
34     P(m) = sum(abs(E).^2)/N;
35
36     EB = fft(EB);
37     EB = exp(1i*(d1(m)*k-dispersion)*dt/2).*EB;
38     EB = ifft(EB);
39     EB = exp((-1-1i*Delta+1i*abs(EB).^2 + 2*1i*mean(abs(E).^2))*dt)
        .*EB ...
40         + 1i*gB*mean(E)*dt;
41     EB = fft(EB);
42     EB = exp(1i*(d1(m)*k-dispersion)*dt/2).*EB;
43     EB = ifft(EB);
44
45     if mod(m, 100) == 0
46         Field(mm, :) = E;
47         mm = mm + 1;
48     end
49
50 end

```

```

51 %% Plotting
52 figure
53 plot(theta/pi, abs(E), 'linewidth', 1);
54 xlabel('Azimuthal_angle_\theta_(\pi)'); ylabel('Intensity_(a.u.)')
55 ;
56 figure
57 plot(fftshift(k), 10*log10(abs(fftshift(fft(E))).^2/N^2));
58 xlabel('Mode_number'); xlim([-50 50]); ylabel('Power_(dB)');
59 figure
60 pcolor(theta.', t(1:100:end).', abs(Field).^2); shading interp;
    colorbar; colormap jet;
    xlabel('Azimuthal_angle_(rad)'); ylabel('Normalized_time');

```

Listing A.2: Solving the LLE using split-step Fourier method, for near-zero-GVD microcomb under SIL.

Wavelength (nm)	$D_2/2\pi$ (kHz)	$\kappa/2\pi$ (MHz)	$g_b/2\pi$ (MHz)	κ_B^{ext}/K
1558.25	13 ± 2	7.2	1.72	0.49
1558.56	-1.5 ± 0.4	7.5	4.67	0.55
1559.22	-33 ± 4	7.3	2.10	0.54
1561.48	-131 ± 16	7.1	2.14	0.60

Table A.2: Summary of simulation parameters, for self-injection locked, near-zero GVD microcomb.

In the simulation of Figure 3.6c-e, the pump power is $P_{\text{in}} \approx 35$ mW ($h \approx \sqrt{13}$), which is estimated by assuming identical facet loss for the two waveguide facets. For pumping at 1561.48 nm (Figure 3.6f), the laser is at its thermal tuning edge (42 degree C), and the on-chip pump power is degraded to an estimated 17 mW.

For the pump wavelengths in Figure 3.6, the dispersion parameters are provided in Table. A.2. The third-order dispersion parameter is fitted to be 7.5 kHz and does not change by much within the measured pumping wavelengths. Other parameters, such as Δ_L and the feedback phase ϕ , are difficult to determine experimentally, and have been adjusted to match the experimental results. The locking strength K is estimated as 2700 (Jin et al., 2021).

In the simulation, the relative feedback phase ψ is adjusted to fit the duty cycle of the temporal waveform, and is -0.10π , 0.20π , -0.42π , 0.0π , respectively, for simulations in Figure 3.6. Also, the steady-state laser cavity detuning $\delta\omega/2\pi$ is simulated to be 18.8 MHz, 19.1 MHz, 21.1 MHz, 19.5 MHz, respectively, for Fig. 2c-f. The steady-state $\delta\omega_{\text{rep}}/2\pi$ is calculated by iterating β_1 in Equation A.6 and

Equation A.7 until there's no drifting in the temporal waveform in the fast frame, and simulated to be 624 kHz, 445 kHz, 283 kHz, -23 kHz, respectively, for Figure 3.6c-f.

A.3 Excitation diagram analysis of the LLE

The excitation diagram analysis of the Lugiato-Lefever Equation (LLE) originates from the Newtonian (or perturbative) approach to solving the LLE (Vladimirov, Tlidi, and Taki, 2021). Although this method is often less numerically stable in practice, it provides valuable insight into the stability landscape of the dynamical system.

We begin with the normalized form of the LLE given in Equation A.4. By decomposing the intracavity field into a continuous-wave (CW) background a_0 and a localized soliton component $A(\theta, t)$, such that $\psi = A + a_0$, a modified evolution equation for the soliton component is obtained:

$$\frac{\partial A}{\partial t} = -(1 + i\Delta)A + id_2 \frac{\partial^2 A}{\partial \theta^2} + i|a_0 + A|^2(a_0 + A) - i|a_0|^2 a_0. \quad (\text{A.9})$$

To analyze the linear stability and excitation spectrum of the system, we define the two-component vector $|\psi\rangle = (A, A^*)^T$ and cast the dynamics in a Heisenberg-like form:

$$i \frac{\partial}{\partial t} |\psi\rangle = \hat{H} |\psi\rangle, \quad (\text{A.10})$$

where the effective Hamiltonian \hat{H} comprises contributions from dispersion, linear loss, and Kerr nonlinearity:

$$\hat{H} = \hat{H}_0 + \hat{H}_{\text{loss}} + \hat{H}_{\text{Kerr}}^{(0)} + \hat{H}_{\text{Kerr}}^{(1)}. \quad (\text{A.11})$$

The individual components are given as follows. The dispersion and detuning term:

$$\hat{H}_0 = \Delta \hat{I} - d_2 \begin{pmatrix} \frac{\partial^2}{\partial \theta^2} & 0 \\ 0 & \frac{\partial^2}{\partial \theta^2} \end{pmatrix}, \quad (\text{A.12})$$

where \hat{I} is the identity operator acting on $|\psi\rangle$. The linear loss term is:

$$\hat{H}_{\text{loss}} = -i\hat{I}. \quad (\text{A.13})$$

The Hermitian (real) part of the Kerr interaction is:

$$\hat{H}_{\text{Kerr}}^{(0)} = - \begin{pmatrix} |A|^2 + Aa_0^* + A^*a_0 + 2|a_0|^2 & 0 \\ 0 & -|A|^2 - Aa_0^* - A^*a_0 - 2|a_0|^2 \end{pmatrix}. \quad (\text{A.14})$$

The non-Hermitian (complex) part of the Kerr interaction is:

$$\hat{H}_{\text{Kerr}}^{(1)} = - \begin{pmatrix} 0 & a_0^2 + Aa_0 \\ -a_0^{*2} - A^* a_0^* & 0 \end{pmatrix}. \quad (\text{A.15})$$

For clarity, we can group the Hermitian and non-Hermitian components as:

$$\hat{H}^{(0)} = \hat{H}_0 + \hat{H}_{\text{Kerr}}^{(0)}, \quad \hat{H}^{(1)} = \hat{H}_{\text{loss}} + \hat{H}_{\text{Kerr}}^{(1)}. \quad (\text{A.16})$$

This formulation enables direct analysis of the excitation spectrum and provides a powerful framework for assessing soliton stability and interaction with perturbations.

Heisenberg equation of the system under perturbation

When the system is perturbed around a stationary solution $|\psi_0\rangle$, the dynamics of the perturbation $|\delta\psi\rangle$ are governed by a linearized evolution equation derived from the Jacobian of the system:

$$i \frac{\partial |\delta\psi\rangle}{\partial t} = \hat{H} |\psi_0\rangle + \hat{J} |\delta\psi\rangle, \quad (\text{A.17})$$

where \hat{H} is the Hamiltonian introduced previously, and \hat{J} is the Jacobian operator composed of the following terms:

$$\hat{J} = \hat{J}_0 + \hat{J}_{\text{loss}} + \hat{J}_{\text{Kerr}}^{(0)} + \hat{J}_{\text{Kerr}}^{(1)}. \quad (\text{A.18})$$

The components of \hat{J} are given by:

$$\hat{J}_0 = \hat{H}_0, \quad \hat{J}_{\text{loss}} = -i\hat{L}, \quad (\text{A.19})$$

$$\hat{J}_{\text{Kerr}}^{(0)} = -2 \begin{pmatrix} |A|^2 + Aa_0^* + A^*a_0 + |a_0|^2 & 0 \\ 0 & -|A|^2 - Aa_0^* - A^*a_0 - |a_0|^2 \end{pmatrix}, \quad (\text{A.20})$$

$$\hat{J}_{\text{Kerr}}^{(1)} = - \begin{pmatrix} 0 & (A + a_0)^2 \\ -(A^* + a_0^*)^2 & 0 \end{pmatrix}. \quad (\text{A.21})$$

To obtain a steady-state solution to Equation A.9 via the Newton-Raphson method, we iteratively update the field using:

$$|\psi_{j+1}\rangle = |\psi_j\rangle - \hat{J}^{-1} \hat{H} |\psi_j\rangle. \quad (\text{A.22})$$

Starting from an approximate single-soliton ansatz, this procedure typically converges to a stable steady-state solution within 100 iterations. The implementation of this method is provided in Listing A.3.

```

1  clc
2  clear
3  %% Initialization
4  N = 1024; k = fftshift(-N/2:N/2-1); theta = linspace(-pi, pi, N);
5  h = 5; D2 = 0.04; Delta = 10;
6  %% Soliton input
7  B = sqrt(2*Delta); phi_tau = 1/(sqrt(2*Delta/D2));
8  a0 = h/(1+1i*Delta);
9  fun = @(E0) (-1-1i*Delta+1i*abs(E0)^2)*E0+h; a0 = fsolve(fun, a0);
10 A = B*sech((theta)/phi_tau)*exp(1i*acos(2/pi/abs(a0)*sqrt(2/Delta)
    ));
11 get_F = @(A) ifft(1i*(-D2*k.^2/2).*fft(A))+ ...
12     (-1-1i*Delta)*A + 1i*abs(A+a0).^2.*(A+a0) - 1i*abs(a0)^2*a0;
13 %% Newton metod iterations
14 for m = 1 : 100
15     L0 = get_matrix_L0(Delta, k, a0, D2);
16     L1 = get_matrix_L1(a0, A);
17     rhs = get_F(A);
18     temp = inv(L0+L1)*[rhs.'; , rhs'];
19     A = A - temp(1:N).';
20 end
21 %% Visualization
22 L0 = get_matrix_L0(Delta, k, a0, D2);
23 L1 = get_matrix_L1(a0, A);
24 figure
25 D = eigs(L0+L1, 100, 'smallestabs');
26 plot(D, '.', 'Markersize', 10);
27 hold on
28 plot([-5, 5], [Delta, Delta], 'r--'); plot([-5, 5], [-Delta, Delta
    ], 'r--');
29 xlabel('Real_part'); ylabel('Imaginary_part');
30 legend('Eigenvalues', 'Detuning')
31 xlim([-5 5]); ylim([-Delta, Delta]*1.5);
32 set(gca, 'TickDir', 'out');
33 title(['Eigenvalues_(single_soliton),_detuning:_', num2str(Delta)
    ]);
34 %% Plot eigenmodes
35 [V, ~] = eigs(L0+L1, 100, 'smallestabs');
36 [~, idx] = mink(abs(imag(D)), 6);
37 s.D = zeros(1, length(idx));
38 s.V = zeros(N, length(idx));
39 for mm = 1 : length(idx)
40     s.D(mm) = D(idx(mm));

```

```

41     s.V(:, mm) = V(1:N, idx(mm));
42     figure
43     plot(theta, real(s.V(:, mm)));
44     xlabel('\theta'); ylabel('Real(eigenmode)');
45     title(['Eigenvalue: ', num2str(D(idx(mm)), '%.2f')]); set(gca,
         'TickDir', 'out');
46 end
47 %% functions
48 function L0 = get_matrix_L0(delta_omega, k, E0, D2)
49     N = length(k);
50     Diff_2 = -conj(dftmtx(N))/N*diag(k.^2)*dftmtx(N);
51     L0_1 = diag(ones(1, N))*(-1-1i*delta_omega+2*1i*abs(E0)^2) + 1
         i*D2/2*Diff_2;
52     L0_2 = diag(ones(1, N))*1i*E0^2;
53     L0 = [L0_1, L0_2; conj(L0_2), conj(L0_1)];
54 end
55 function L1 = get_matrix_L1(E0, e0)
56     L1_1 = 2*1i*conj(E0)*diag(e0) + 2*1i*E0*diag(conj(e0)) + 2*1i*
         diag(abs(e0).^2);
57     L1_2 = 2*1i*E0*diag(e0) + 1i*diag(e0.^2);
58     L1 = [L1_1, L1_2; conj(L1_2), conj(L1_1)];
59 end

```

Listing A.3: Solving the LLE using Newtonian Method.

The excitation diagram

A key feature of the Newtonian method is that the eigenvalues λ of the operator $\hat{L} = -i\hat{J}$ can be numerically computed, enabling linear stability analysis of the steady-state solution. For a stationary solution, the perturbation evolves as

$$\frac{\partial |\delta\psi\rangle}{\partial t} = \hat{L} |\delta\psi\rangle, \quad (\text{A.23})$$

and the eigenvalues of \hat{L} indicate whether the perturbation grows, decays, or remains neutral over time.

As an example, for a stable bright soliton solution (Figure A.1a), the excitation spectrum reveals a ‘neutral mode’ at $\lambda = 0$. This zero eigenvalue reflects the translational symmetry of the soliton within the cavity: the soliton may move freely in the angular coordinate θ without being damped or amplified. In addition, two pairs of complex-conjugate eigenmodes—known as the S and C resonances—appear (Figure A.1b,c), consistent with the results reported in (Guo et al., 2017).

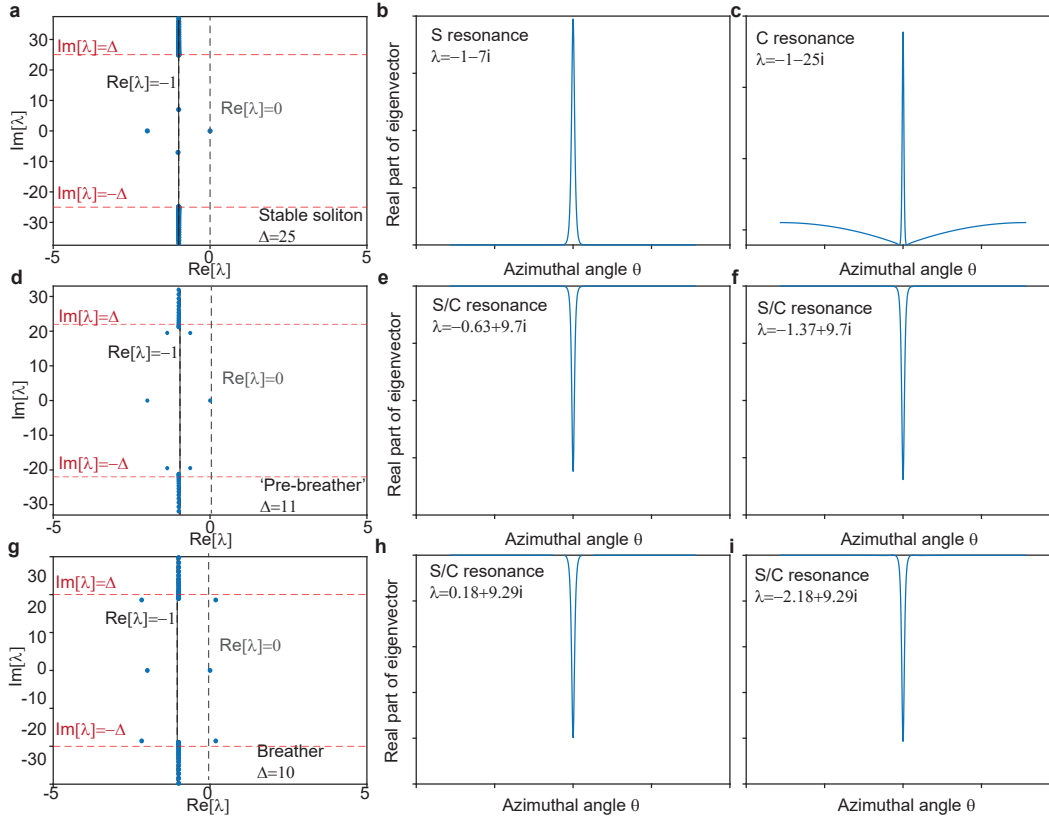


Figure A.1: **Excitation spectrum calculation of a single soliton ($h = 5$).** **a-c**, A stable soliton state ($\Delta = 25$). **d-f**, A ‘pre-breather’ state ($\Delta = 11$). **g-i**, A breather soliton state ($\Delta = 10$).

The ‘pre-breather’ regime and exceptional point behavior

An intriguing outcome of this analysis is the identification of a ‘pre-breather’ regime. The breather soliton is a dynamic solution to the LLE in which the soliton’s shape oscillates periodically in time, typically occurring at small detuning values Δ (Bao et al., 2016; Lucas, Karpov, et al., 2017; M. Yu et al., 2017).

Excitation diagram analysis reveals that the onset of this breathing behavior arises from a non-Hermitian coupling between the S and C resonances. As the system parameters approach a critical point, these two modes coalesce spectrally, forming a non-Hermitian degeneracy known as an **exceptional point** (EP) (Miri and Alu, 2019). This phenomenon is illustrated in Figure A.1d–i.

Importantly, this analysis also demonstrates that the soliton dynamics can be largely described using only a few dominant eigenmodes, rather than requiring full-field simulations. This insight motivates the Lagrangian analysis presented in the following section, where soliton dynamics are projected onto a small set of collective

coordinates associated with these dominant modes under various perturbations.

A.4 Lagrangian formula of pulse pumped soliton

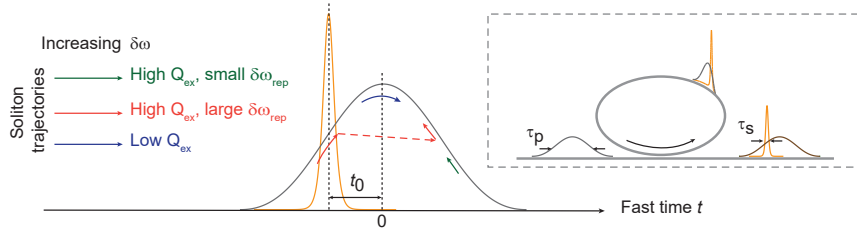


Figure A.2: **Pulse pumped microcavity soliton.** Pulse pumping of a microcavity soliton in the presence of the Raman effect. Main panel: illustration of soliton position relative to the pump pulse under different pump rates and detunings. Inset: A relatively broad pumping pulse (width τ_p) is coupled into a microcavity. A narrower soliton pulse (width τ_s) is generated and trapped by the pump field.

The method of Lagrangian analysis has been used to analysis soliton dynamics in microresonators (Matsko and Maleki, 2013; Guo et al., 2017; Yi et al., 2016b; Lucas, Guo, et al., 2017). In a side project of my PhD, the method was used to analysis the dynamics of a pulse pumped DKS. The analysis was originally used for improving the energy efficiency of soliton microcomb (J. Li et al., 2022); here, the results are included as a showcase of the theoretical tool and associated rich dynamics. The scheme of the pulse pumped soliton is depicted in Figure A.2. Solitons are generated by a periodic pulsed pump instead of a continuous pump (Obrzud, Lecomte, and Herr, 2017).

The analysis begins where the LLE with a pulsed input term followed by the notations in Equation A.2,

$$\begin{aligned} \frac{\partial E(t, T)}{\partial T} = & -\left(\frac{\kappa}{2} + i\delta\omega\right) E(t, T) - i\frac{D_2}{2D_1^2} \frac{\partial^2 E(t, T)}{\partial t^2} - \frac{\delta\omega_{\text{rep}}}{D_1} \frac{\partial E(t, T)}{\partial t} + \sqrt{\kappa_e} E_{\text{in}}(t) \\ & + ig|E(t, T)|^2 E(t, T) - ig\tau_R \frac{\partial |E(t, T)|^2}{\partial t} E(t, T), \end{aligned} \quad (\text{A.24})$$

where g is the Kerr coefficient, and $\tau_R \approx 1.7$ fs is the Raman shock time. $\delta\omega_{\text{rep}}$ is the difference between the pump rate and the cavity FSR .

The intra-cavity field is composed of a Sech-envelope soliton E_s with a background E_b , i.e.,

$$E(t, T) = E_s(t, T) + E_b(t, T), \quad (\text{A.25})$$

where

$$E_s(t, T) = B_s \operatorname{Sech}\left(\frac{t - t_0}{\tau_s}\right) e^{-i\delta\Omega(t-t_0) + i\varphi_s}. \quad (\text{A.26})$$

Here B_s is the soliton amplitude, t_0 is the soliton central position in the rotating pump frame, τ_s is the soliton pulse width, $\delta\Omega$ is the frequency shift of the soliton, and φ_s is the phase of the soliton. Under the weak background approximation ($|E_b|^2 \ll |E_s|^2$), we keep only the leading order of E_b . To verify this approximation, simulations show that $|E_b|^2$ is more than 15 times smaller than $|E_s|^2$ even for the weakest loading conditions (i.e., highest Q_{ex}). By substituting Equation A.25 into Equation A.24, the simplified equation yields

$$\begin{aligned} i\frac{\partial E_s}{\partial T} + i\delta\omega_{\text{rep}}\frac{\partial E_s}{\partial t} - \frac{D_2}{2D_1^2}\frac{\partial^2 E_s}{\partial t^2} + g[|E_s|^2(E_s + 2E_b) + E_s^2 E_b^*] \\ - \delta\omega E_s = -i\frac{\kappa}{2}E_s + ig|E_s|^2 E_s + \tau_R g \frac{\partial |E_s|^2}{\partial t} E_s. \end{aligned} \quad (\text{A.27})$$

Meanwhile, the background E_b is approximated as the trivial solution of the LLE equation.

With Lagrangian density defined as (Yi et al., 2016a; Lucas, Guo, et al., 2017)

$$\begin{aligned} \mathcal{L} = \frac{i}{2}\left(\frac{\partial E_s}{\partial T} E_s^* - \frac{\partial E_s^*}{\partial T} E_s\right) - \frac{i}{2}\delta\omega_{\text{rep}}\left(\frac{\partial E_s}{\partial t} E_s^* - \frac{\partial E_s^*}{\partial t} E_s\right) - \frac{D_2}{2}\frac{\partial E_s}{\partial t}\frac{\partial E_s^*}{\partial t} \\ + \frac{g}{2}(|E_s|^4 + 2|E_s|^2(E_s E_b^* + E_s^* E_b)) - \delta\omega|E_s|^2, \end{aligned} \quad (\text{A.28})$$

and a perturbing term defined as

$$\mathcal{R} = -i\frac{\kappa}{2}E_s + \tau_R g \frac{\partial |E_s|^2}{\partial t} E_s, \quad (\text{A.29})$$

the dynamics are retrieved by

$$\frac{\delta \mathcal{L}}{\delta E_s^*} = \frac{\partial \mathcal{L}}{\partial E_s^*} + \frac{\partial}{\partial T} \frac{\partial \mathcal{L}}{\partial (\partial E_s^* / \partial T)} + \frac{\partial}{\partial t} \frac{\partial \mathcal{L}}{\partial (\partial E_s^* / \partial t)} = \mathcal{R}. \quad (\text{A.30})$$

The overall Lagrangian is thus calculated by $L = \int_{t_0+T_R}^{t_0-T_R} \mathcal{L} dt$ (technically the integral range is replaced by $\pm\infty$), and evaluated to be

$$L = 2B_s^2 \tau_s \left(-\frac{\partial t_0}{\partial T} \delta\Omega + \delta\omega_{\text{rep}} \delta\Omega - \frac{\partial \varphi_s}{\partial T} - \delta\omega - \frac{D_2}{2} \delta\Omega^2 - \frac{D_2}{6\tau_s^2} + \frac{g}{3} B_s^2 \right) + L_b, \quad (\text{A.31})$$

where L_b is the contribution of the background, yielding

$$L_b = \pi g B_s^3 t_0 \operatorname{Re} [E_b^*(T, t_0) e^{i\varphi_s}]. \quad (\text{A.32})$$

With the equation $\frac{\partial L}{\partial q} - \frac{d}{dt} \left(\frac{\partial L}{\partial \dot{q}} \right) = \int (\mathcal{R} \frac{\partial A^*}{\partial q} + \mathcal{R}^* \frac{\partial A}{\partial q}) dt$, we assign q to be B_s , τ_s , t_0 , $\delta\Omega$ and φ_s , accordingly, and the following dynamical equations result:

$$-\frac{\partial t_0}{\partial T} \delta\Omega + \delta\omega_{\text{rep}} \delta\Omega - \frac{\partial \varphi_s}{\partial T} - \delta\omega - \frac{D_2}{2} \delta\Omega^2 - \frac{D_2}{6\tau_s^2} + \frac{2g}{3} B_s^2 + \frac{3\pi g}{4} \text{Re}[E_b^*(T, t_0) e^{i\varphi_s}] = 0, \quad (\text{A.33})$$

$$-\frac{\partial t_0}{\partial T} \delta\Omega + \delta\omega_{\text{rep}} \delta\Omega - \frac{\partial \varphi_s}{\partial T} - \delta\omega - D_2 \delta\Omega^2 - \frac{D_2}{6\tau_s^2} + \frac{g}{3} B_s^2 + \frac{\pi g}{2} \text{Re}[E_b^*(T, t_0) e^{i\varphi_s}] = 0, \quad (\text{A.34})$$

$$\frac{\partial (B_s^2 \tau_s \delta\Omega)}{\partial T} = -\kappa B_s^2 \tau_s \delta\Omega - \frac{8\tau_s g B_s^4}{15\tau_s} - \frac{\pi g B_s^2}{2} \text{Re} \left[\frac{\partial E_b^*}{\partial t_0} e^{i\varphi_s} \right], \quad (\text{A.35})$$

$$D_1 \frac{\partial t_0}{\partial T} - \delta\omega_{\text{rep}} + \frac{D_2}{D_1} \delta\Omega = 0, \quad (\text{A.36})$$

$$\frac{\partial (B_s^2 \tau_s)}{\partial T} = -\kappa B_s^2 \tau_s + \frac{\pi g B_s^3 \tau_s}{2} \text{Im}[E_b^*(T, t_0) e^{i\varphi_s}]. \quad (\text{A.37})$$

For the steady-state case, i.e., setting $\partial/\partial T = 0$ in Equations A.33, A.34, A.36, A.37, the following expressions are derived:

$$B_s^2 \approx \frac{2}{g} \delta\omega \left(1 + \frac{5}{4} \alpha \right), \quad \tau_s^2 \approx \frac{D_2}{2D_1^2} \frac{1}{\delta\omega} \left(1 - \frac{1}{2} \alpha \right), \quad (\text{A.38})$$

$$\delta\Omega = \frac{D_1}{D_2} \delta\omega_{\text{rep}}, \quad (\text{A.39})$$

$$\text{Im}[E_b^*(t_0) e^{i\varphi_s}] = \frac{\kappa}{\pi} \sqrt{\frac{2}{g\delta\omega}}, \quad (\text{A.40})$$

$$\alpha = \frac{\pi g B_s}{2\delta\omega} \text{Re}[E_b^* e^{i\varphi}] = \sqrt{\frac{\pi^2 g |E_b|^2 \delta\omega - 2\kappa^2}{2\delta\omega^2}}. \quad (\text{A.41})$$

It is noted that the rotating frame follows the external pumping pulse, while the cavity *FSR* remains unchanged. Equation (A.39) reveals that the soliton frequency shift is determined by the pump rate under pulse pumping.

To determine the background field, Raman and cavity dispersion are ignored and the following equation is solved,

$$\frac{\partial E}{\partial T} = -\left(\frac{\kappa}{2} + i\delta\omega \right) E + ig|E|^2 E + \sqrt{\kappa_e} E_{\text{in}}(t), \quad (\text{A.42})$$

which yields the solution,

$$E_b = \sqrt{\kappa_e} \frac{E_{\text{in}}(t)}{\kappa/2 + i\delta\omega - i|E_b|^2}. \quad (\text{A.43})$$

With the exception of the soliton stability analysis below the Kerr effect is not included. Ignoring the Kerr effect and for real E_{in} (i.e., minimal or no chirping),

the phase of E_b^* can be seen to be approximately $\pi/2$ for large laser-cavity detuning (i.e., $\delta\omega \gg \kappa$). With this condition, equation (A.37) can be further approximated as,

$$\cos \varphi_s = \frac{\kappa}{\pi |E_b(t_0)|} \sqrt{\frac{2}{g\delta\omega}}. \quad (\text{A.44})$$

Also, since $|\cos \varphi_s| < 1$, equation (A.44) gives an existence limit on the detuning $\delta\omega$,

$$\delta\omega_{\max} \approx \frac{\pi^2 g \kappa_e |E_{\text{in}}(t_0)|^2}{2\kappa^2}. \quad (\text{A.45})$$

Expressing α using the normalized detuning ξ ($\xi = 2\delta\omega Q/\omega_0$) and defining $\xi_0(t_0) \equiv 2\delta\omega_{\max}(t_0)Q/\omega_0$, results in the following expression (X. Li et al., 2018),

$$\alpha \approx \frac{2}{\xi^{3/2}} \sqrt{\xi_0(t_0) - \xi}. \quad (\text{A.46})$$

Also, by substituting the above results into the steady solution of equation (A.35),

$$\delta\omega_{\text{rep}} = \frac{D_2}{D_1} \Omega_{\text{Raman}} - K_L(t_0, \delta\omega), \quad (\text{A.47})$$

where Ω_{Raman} is Raman self-frequency shift (Yi et al., 2016b),

$$\Omega_{\text{Raman}} = -\frac{8\tau_R g B_s^2}{15\kappa\tau_s^2} \approx -\frac{32\tau_R D_1^2 \delta\omega^2}{15\kappa D_2} \left(1 + \frac{7}{4}\alpha\right) \quad (\text{A.48})$$

and where $K_L(t_0, \delta\omega)$ is,

$$K_L(t_0, \delta\omega) = \frac{\pi D_2}{2\kappa D_1} \text{Re} \left[\frac{\partial g B_s E_b^*}{\partial t_0} e^{i\varphi_s} \right] = \frac{\pi D_2 Q}{\omega_0 D_1} \sqrt{\frac{g\delta\omega}{2}} \text{Re} \left[\frac{\partial E_b^*}{\partial t_0} e^{i\varphi_s} \right] \left(1 + \frac{5}{8}\alpha\right). \quad (\text{A.49})$$

This equation determines the soliton position t_0 .

By expressing the background E_b^* as $E_b^* = i|E_b|e^{-i\varphi_b}$, we can further write $\text{Re} \left[\frac{\partial E_b^*}{\partial t_0} e^{i\varphi_s} \right] = -\frac{\partial |E_b|}{\partial t_0} \sin(\varphi_s - \varphi_b) + |E_b| \frac{\partial \varphi_b}{\partial t_0} \cos(\varphi_s - \varphi_b)$. K_L can then be separated into a pump-amplitude-slope contribution (amplitude derivative with respect to t_0) and a pump-chirp contribution (phase derivative with respect to t_0) by letting $K_L \equiv K_a + K_p$ where,

$$K_a \propto -\frac{\partial |E_b|}{\partial t_0} \sqrt{1 - \frac{\xi}{\xi_0(t_0)}}, \quad K_p \propto |E_b| \frac{\partial \varphi_b}{\partial t_0} \sqrt{\frac{\xi}{\xi_0(t_0)}}. \quad (\text{A.50})$$

In terms of their impact on soliton stability, the amplitude contribution pushes the soliton away from the pump amplitude maximum, while the phase contribution pulls the soliton to the pump phase maximum ($\partial \phi_b / \partial t_0 = 0$ and $\partial^2 \phi_b / \partial t_0^2 < 0$) (Jang et al., 2015).

Now consider again Equation A.43. The Kerr effect in this equation induces a chirp in the pump that contributes to K_p . To assess its importance, we solve Equation A.43 taking account of the Kerr term as a perturbation. In this case, E_b^* can be expressed in the pump power as,

$$E_b^* \approx \sqrt{\kappa_e} \frac{E_{in}^*}{\kappa/2 - i\omega} \left(1 + i \frac{g\kappa_e}{\kappa/2 - i\delta\omega} \frac{|E_{in}|^2}{\kappa^2/4 + \delta\omega^2}\right)^{-1}. \quad (\text{A.51})$$

Also, the phase of E_b^* can be approximately expressed by,

$$\text{Arg}[E_b^*] \approx \text{Arg}[E_{in}^*] + \arctan\left(\frac{2\delta\omega}{\kappa}\right) - \frac{g\kappa\kappa_e|E_{in}|^2}{2T_R(\kappa^2/4 + \delta\omega^2)^2}. \quad (\text{A.52})$$

Using these results, two representative $K_L(t_0, \delta\omega)$ are plotted in Figure A.3 for fixed $\delta\omega$. In this case, K_L features an S-like shape, which is similar to previous reports (Hendry et al., 2019) using the neutral mode mapping technique (Maggipinto et al., 2000). Positive (negative) K_L pushes the soliton forward (backward) in the fast time frame so that for these parameters, the soliton is pushed away from the pumping maximum. Here, the S-like shape is weakened as a result of reduction of the K_a contribution to K_L . In this case the soliton can reside at the pump maximum. These differences in behavior can be understood by examining the impact on K_a associated with the term $\sqrt{1 - \xi/\xi_0(t_0)}$. When pumped at a power much higher than the soliton threshold ($\xi_0(t_0) \gg 1$), the soliton cannot be trapped near the pump pulse center; and it lies near the existence boundary. This happens because K_a is larger (i.e., because $\sqrt{1 - \xi/\xi_0(t_0)}$ is closer to unity) except at the existence boundary where $\sqrt{1 - \xi/\xi_0(t_0)}$ goes to 0 (panel a). On the other hand, when pumped with a low power relative to the threshold, as happens with increased cavity loading, the soliton can be trapped at the pump center (panel b), because here the relative importance of K_a is reduced since $\sqrt{1 - \xi/\xi_0(t_0)}$ is closer to zero.

It is noted that when evaluating the maximum possible detuning Equation (A.45), the Kerr contribution is neglected, while in the background phase expression Equation (A.52), the Kerr contribution is kept. This is because the Kerr effect of the background field, i.e., $g|E_b|^2$, is weak compared with the cavity loss rate ($g|E_b|^2 \ll \kappa$) so it is reasonable to neglect it in Equation A.44 where it is not the leading-order term. However, when evaluating the background field phase φ_b , it is the leading-order term and introduces a non-uniform intracavity phase across the circulating pumping pulse. The resulting pulse chirp is an essential contribution to K_p (Equation A.50), and impacts soliton trapping by the pump pulse. Because the Kerr contribution is

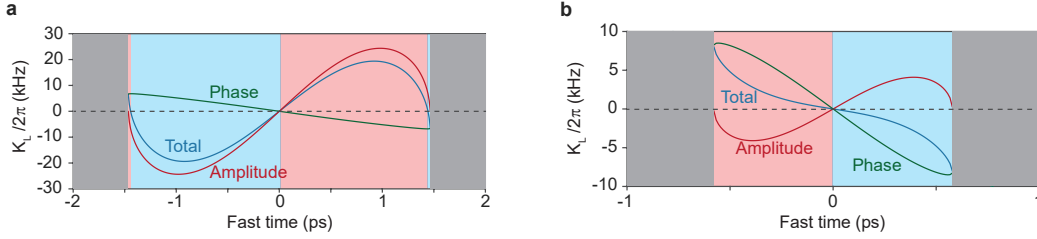


Figure A.3: **Representative locking term $K_L(t_0, \delta\omega)$.** **a**, Nonlinear locking term for $Q_{\text{ex}} = 34$ million. Detuning $\delta\omega/2\pi = 27$ MHz and $\delta\omega_{\text{max}}/2\pi = 59.8$ MHz. Area with positive K_L is shaded in red, while that with negative K_L is shaded with blue. Positive (negative) K_L pushes the soliton forward (backward) in the fast time frame. Phase chirp term (K_p) and amplitude slope term (K_a) contributions of K_L are plotted with green and red, respectively. **b**, K_L is plotted under conditions of stronger over-coupling. The coupling Q_{ex} factor is reduced to 11 million, $\delta\omega/2\pi = 27$ MHz, $\delta\omega_{\text{max}}/2\pi = 28.4$ MHz, while other parameters are the same as in panel a.

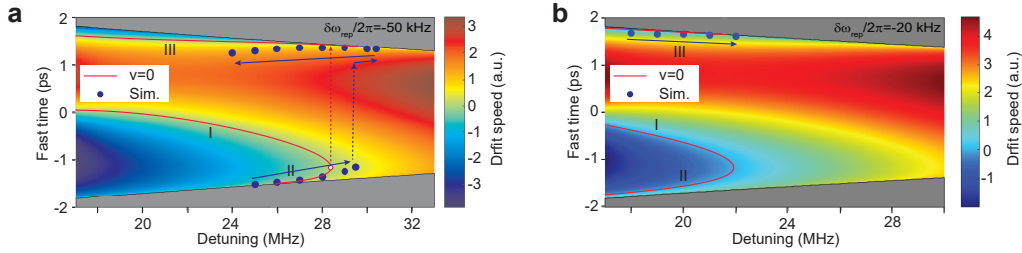


Figure A.4: **Drift speed of the soliton based on the Lagrangian analysis and numerically simulated steady states.** **a**, The pump offset rate is set as $\delta\omega_{\text{rep}} = -50$ kHz. **b**, The pump offset rate is set as $\delta\omega_{\text{rep}} = -20$ kHz. Zero drift speed positions are marked by solid red lines. It is noted that branch II and III are stable trapping positions, while branch I is unstable. The intersections of branch I and II are marked by a circle. Gray shading indicates that no soliton solution exists. The simulated steady-state trapping positions are plotted with blue dots. Tuning direction of the pump laser frequency in the simulation is illustrated with blue arrows.

weak, the soliton is trapped close to the existence boundary in cases where the cavity is not overloaded.

Evolution of soliton trapping position

Equations A.34 and A.35 give the dynamics of the trapping position t_0 :

$$\frac{\partial t_0}{\partial T} = \frac{1}{D_1} \left[\delta\omega_{\text{rep}} - \frac{D_2}{D_1} \Omega_{\text{Raman}} + K_L(t_0, \delta\omega) \right] \equiv v(t_0, \delta\omega), \quad (\text{A.53})$$

where $v(t_0, \delta\omega)$ is the drift speed of the soliton central position in the fast frame, similar to the definition in reference (Hendry et al., 2019). It is noted that negative

$\delta\omega_{\text{rep}}$ contributes a negative component to the drift speed, while the Raman effect contributes a positive component to the drift speed. A steady trapping is achieved when the residual drift is compensated by the nonlinear trapping $K_L(t_0, \delta\omega)$.

Drift speed when $\delta\omega_{\text{rep}}/2\pi = -50$ kHz is plotted in Figure A.4a. Positions with zero drift speed are marked by red solid lines, and divided into three branches I, II and III. From the 2D plot, by including a perturbation on the soliton position t_0 , it can be inferred that a soliton sitting on the branch I is unstable, while II and III provide stable trapping positions.

The 2D drift speed plot also provides insights on evolution of the soliton position upon pump tuning. By sweeping a laser from blue to red detuned, initially, the soliton is generated near $t_0 = 0$, where the Kerr gain reaches its maximum. For Figure A.4a, the combined negative drift effect $v(t_0, \delta\omega) < 0$ (as $\delta\omega_{\text{rep}}$ is very negative) pushes the soliton to branch II where the soliton is stably trapped. As detuning $\delta\omega$ further increases, contribution from the Raman effect increases (see Equation (A.47)) and pushes the soliton upwards. At a certain detuning, the unstable branch I collides with branch II, and is associated with a saddle-node bifurcation. Beyond this point, the drift speed $v(t_0, \delta\omega) > 0$, and the soliton ‘jumps’ to the other stable trapping branch III, which is on the other side of the pump pulse. If detuning is further increased, the soliton hits the existence boundary and disappears. If the detuning $\delta\omega$ is tuned backwards after the ‘jump’, the soliton is still trapped on branch III, and a hysteresis behavior is observed.

Numerically simulated steady soliton positions with the same parameters are also plotted in in Figure A.4a for comparison. The detuning scanning direction is illustrated with blue arrows. As predicted, initially the soliton is trapped at $t_0 < 0$. As detuning increases, the soliton loses its stability, travels to the other side of the pump pulse and eventually disappears. A hysteresis behavior of the trapping position is also observed when the detuning $\delta\omega$ is tuned backwards.

Similarly, 2D drift speed when $\delta\omega_{\text{rep}}/2\pi = -20$ kHz is plotted in Figure A.4b. In this case, the soliton is initially generated near the pump pulse center $t_0 = 0$, where on the contrary $v > 0$ (as the Raman contribution overrides the small negative $\delta\omega_{\text{rep}}$ from the minimum detuning $\delta\omega$ where the soliton is generated), and is then trapped near branch III. As detuning further increases, the soliton encounters the existence boundary and disappears, and no ‘jump’ behavior is observed.

References

- Bao, Chengying et al. (2016). “Observation of Fermi-Pasta-Ulam recurrence induced by breather solitons in an optical microresonator.” In: *Physical Review Letters* 117.16, p. 163901.
- Chembo, Yanne K. and Curtis R. Menyuk (2013). “Spatiotemporal Lugiato-Lefever formalism for Kerr-comb generation in whispering-gallery-mode resonators.” In: *Physical Review A* 87.5, p. 053852.
- Guo, Hairun et al. (2017). “Universal dynamics and deterministic switching of dissipative Kerr solitons in optical microresonators.” In: *Nature Physics* 13.1, pp. 94–102.
- Hendry, Ian et al. (2019). “Impact of desynchronization and drift on soliton-based Kerr frequency combs in the presence of pulsed driving fields.” In: *Physical Review A* 100.2, p. 023829.
- Jang, Jae K. et al. (2015). “Temporal tweezing of light through the trapping and manipulation of temporal cavity solitons.” In: *Nature Communications* 6.
- Ji, Qing-Xin et al. (2023). “Engineered zero-dispersion microcombs using CMOS-ready photonics.” In: *Optica* 10.2, pp. 279–285.
- Jin, Warren et al. (2021). “Hertz-linewidth semiconductor lasers using CMOS-ready ultra-high-Q microresonators.” In: *Nature Photonics* 15.5, pp. 346–353.
- Li, Jiang et al. (2022). “Efficiency of pulse pumped soliton microcombs.” In: *Optica* 9.2, pp. 231–239.
- Li, Xinbai et al. (2018). “Universal isocontours for dissipative Kerr solitons.” In: *Optics Letters* 43.11, pp. 2567–2570.
- Lucas, Erwan, Hairun Guo, et al. (2017). “Detuning-dependent properties and dispersion-induced instabilities of temporal dissipative Kerr solitons in optical microresonators.” In: *Physical Review A* 95.4, p. 043822.
- Lucas, Erwan, Maxim Karpov, et al. (2017). “Breathing dissipative solitons in optical microresonators.” In: *Nature Communications* 8.1, p. 736.
- Lugiato, Luigi A. and René Lefever (1987). “Spatial dissipative structures in passive optical systems.” In: *Physical Review Letters* 58.21, p. 2209.
- Maggipinto, Tommaso et al. (2000). “Cavity solitons in semiconductor microresonators: Existence, stability, and dynamical properties.” In: *Physical Review E* 62.6, p. 8726.
- Matsko, Andrey B. and Lute Maleki (2013). “On timing jitter of mode locked Kerr frequency combs.” In: *Optics Express* 21.23, pp. 28862–28876.
- Miri, Mohammad-Ali and Andrea Alu (2019). “Exceptional points in optics and photonics.” In: *Science* 363.6422, eaar7709.

- Obrzud, Ewelina, Steve Lecomte, and Tobias Herr (2017). “Temporal solitons in microresonators driven by optical pulses.” In: *Nature Photonics* 11.9, p. 600.
- Vladimirov, Andrei G, Mustapha Tlidi, and Majid Taki (2021). “Dissipative soliton interaction in Kerr resonators with high-order dispersion.” In: *Physical Review A* 103.6, p. 063505.
- Wang, Heming et al. (2022). “Self-regulating soliton switching waves in microresonators.” In: *Physical Review A* 106.5, p. 053508.
- Yi, Xu et al. (2016a). “Active capture and stabilization of temporal solitons in microresonators.” In: *Optics Letters* 41.9, pp. 2037–2040.
- (2016b). “Theory and measurement of the soliton self-frequency shift and efficiency in optical microcavities.” In: *Optics Letters* 41.15, pp. 3419–3422.
- Yu, Mengjie et al. (2017). “Breather soliton dynamics in microresonators.” In: *Nature Communications* 8.1, p. 14569.

Appendix B

ADDITIONAL EXPERIMENTAL RESULTS

If a workman wants to do his work well, the tools must be firstly sharpened.

Confucian Analects

B.1 Setup of the self-injection locked microcomb

While the self-injection locked (SIL) microcomb promises turnkey and robust operation due to its unique feedback mechanism (Boqiang Shen et al., 2020), preliminary testing often reveals subtle operational challenges. This section outlines several practical techniques and considerations that can facilitate reliable SIL microcomb generation and characterization during initial experimentation.

Packaging of the DFB laser for self-injection locking

The packaging of the DFB laser for butt-coupled self-injection locking was developed by Leo Wu, based on an original design by Dave Kinghorn (Pro Precision Process & Reliability LLC).

The process begins with the DFB laser die bonded to a copper submount, as supplied by the vendor (e.g., PhotonX Inc.; see Figure B.1a). For effective butt-coupling to the photonic chip, the laser facet should overhang slightly beyond the edge of the submount. A thermistor is co-mounted on the submount for temperature monitoring—this may be pre-integrated by the vendor or added in-house.

The submount is then affixed to a modified butterfly case equipped with a thermoelectric cooler (TEC), as shown in Figure B.1b. The butterfly case is mechanically modified to allow for direct butt-coupling. Alignment must be carefully maintained to prevent tilting of the laser facet relative to the case opening. Wire bonding is used to connect the laser and thermistor to the butterfly package leads, enabling external electrical access.

Once assembled, the butterfly case is secured to an aluminum heat sink for thermal stability (Figure B.1c). A close-up view of the wire bonding layout is shown in

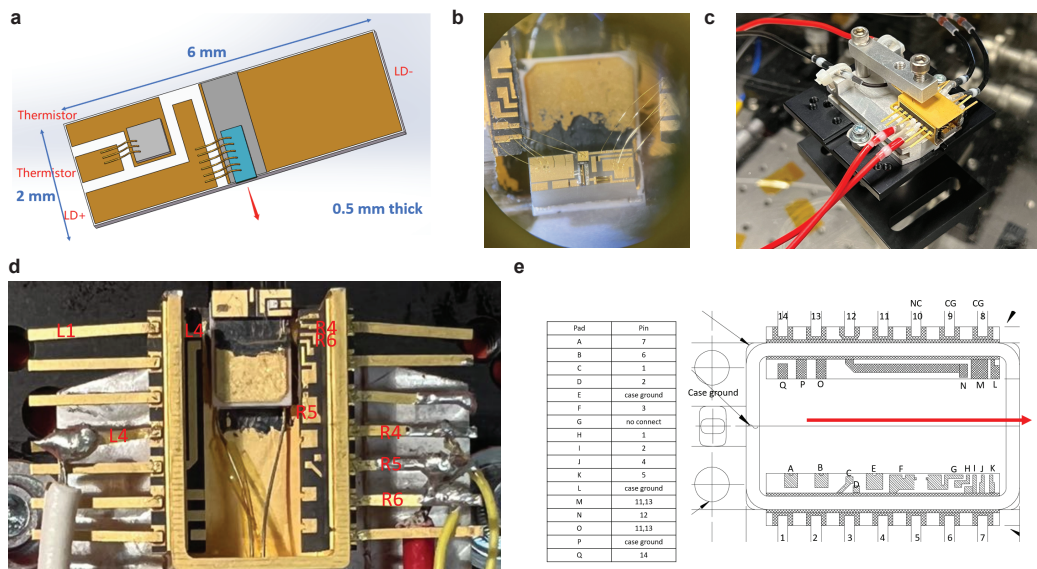


Figure B.1: **Packaging of DFB lasers for self-injection locking.** **a**, Schematic of the DFB laser mounted on a submount with an integrated thermistor. **b**, Photograph of the laser on the submount, attached to a thermoelectric cooler (TEC) and wire-bonded to a butterfly case for electrical interfacing. **c**, Final package: butterfly case mounted to an aluminum heat sink. **d**, Close-up showing the wire bonding within the butterfly case. **e**, Pin diagram of the butterfly package. Materials credit to Leo Wu.

Figure B.1d, and the pin configuration is provided in Figure B.1e.

Robust laser operation requires meticulous attention to both electrical and mechanical integration. Epoxy application must be controlled to avoid obstructing wire bonding pads or the laser aperture. All bonds (both wire and solder) should be mechanically reinforced to prevent damage during handling and transport. Wire tension and connector strain must be properly managed. Furthermore, current-carrying wires should be twisted to suppress electromagnetic pickup, which otherwise may introduce noise features (e.g., a ~ 100 kHz spur) into the RF spectrum.

Assembly of the Si_3N_4 chip with temperature control

The assembly begins with the construction of the temperature-controlled stage, which should be firmly built before mounting the photonic chip. While it is possible to complete this step after wire bonding, doing so risks damaging the bonded wires.

To monitor the chip temperature, a thermistor is inserted into a machined hole in the top copper plate. To improve thermal contact, thermally conductive pad material is mashed and packed around the thermistor head inside the hole. The hole is then

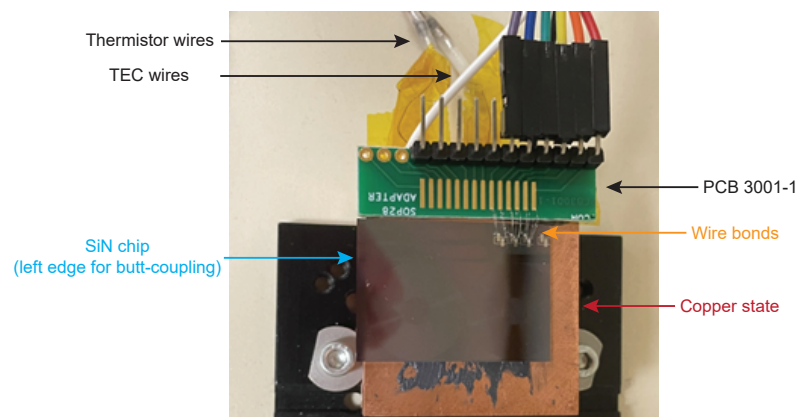


Figure B.2: **Assembly of the Si_3N_4 chip with temperature control.**

sealed with epoxy to fix the thermistor in place. A ceramic TEC or resistive heater is installed between the top and bottom copper plates using thermal conductive epoxy (8329TCS) to ensure efficient heat transfer.

If the chip includes electrically controlled components (e.g., integrated heaters or piezoelectric actuators), a printed circuit board (PCB) must be mounted onto the copper submount beforehand—or concurrently with the chip—so as not to obstruct later bonding steps. The PCB used here is PCB3001-1, cut in half prior to mounting. An array of header pins is soldered to the PCB before wire bonding to simplify subsequent electrical interfacing. To prevent shorting, Kapton tape is applied to the underside of the PCB to isolate exposed pads from the metal submount. The PCB is then affixed to the copper stage using the same thermally conductive adhesive.

The Si_3N_4 photonic chip is mounted onto the same copper submount using the same adhesive. During placement, the chip should be aligned such that its left edge is parallel to the submount edge and overhangs by approximately 1 mm for efficient butt-coupling with the DFB laser. Care should be taken to apply only a thin layer of adhesive beneath the chip; a clean tweezer can be used to gently press the chip during curing to ensure good thermal contact and alignment.

Turn-on Procedure for the Self-Injection Locked Microcomb

Prior to initiating comb generation, additional mechanical stabilization of the system is recommended. Soft electrical wires should be used to route connections from the laser and chip stage while minimizing mechanical stress. These wires should be securely fastened to the optical table to reduce the transmission of mechanical vibrations to both the laser and the chip.

Both the laser and chip temperatures must be stabilized. The laser temperature should be maintained above 20 °C to prevent water condensation. The temperature stability of the laser should be better than 1 mK. The chip stage temperature should be set above room temperature to ease the thermal load on the heat sink.

The next step involves optical alignment. The laser should be positioned within 1 μm of the chip edge to ensure efficient butt-coupling. The fiber lens should be pre-aligned using visible red light. The laser is then powered on and ramped to a moderate current (e.g., 200 mA). Alignment of the distributed feedback (DFB) laser should be optimized by monitoring the transmitted optical power.

Upon completing the alignment procedure, a warm-up period is recommended to allow the system to reach thermal equilibrium; this process may take several hours. Once thermal stability is achieved, the self-injection locking process can be initiated. After measurements are completed, the laser should be retracted from the chip to minimize the risk of mechanical contact when the system is not in use.

B.2 Observation of interband multicolor solitons

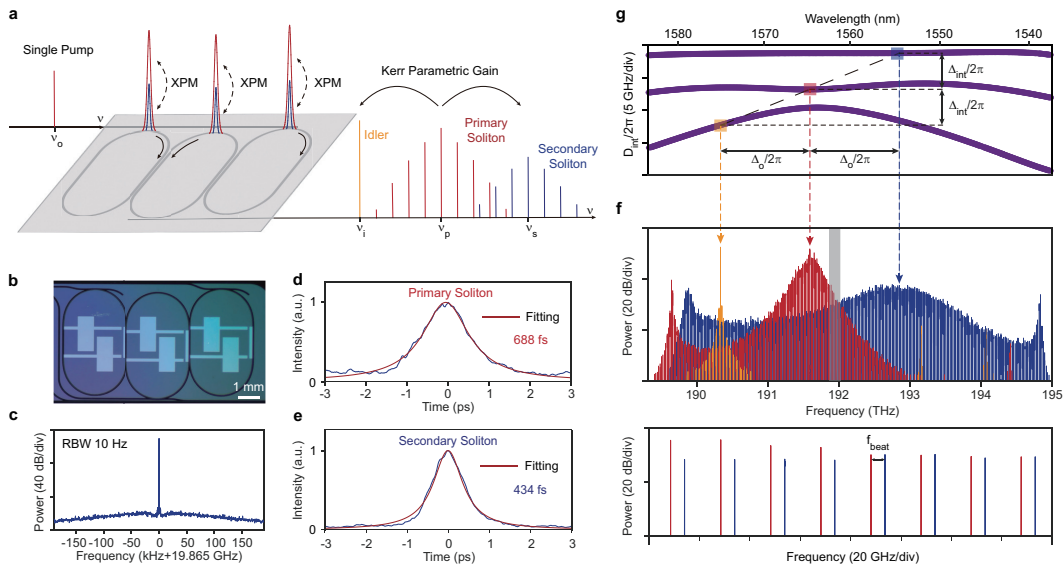


Figure B.3: **Generation of the interband multicolor solitons.** **a**, Conceptual illustration of interband multicolor solitons generation. **b**, Photograph of the three-coupled-ring device used in this study. **c**, RF spectrum of detected pulse train (10 Hz resolution bandwidth). **d,e**, Measured autocorrelation traces (blue) and their Lorentzian fitting curves (red) for the primary and secondary solitons. **f**, Optical spectrum of interband multicolor solitons. The lower panel is a zoom-in view of the gray shaded area in the upper graph. **g**, Corresponding cavity dispersion spectrum.

A new class of complex solitary wave in optical microresonators has been theoretically proposed (Luo, Liang, and Lin, 2016), and referred to as multicolor solitons. It landscapes that dispersive waves (Cherenkov radiations) from a primary soliton coherently pump another soliton (or several other solitons) via Kerr parametric gain at a different optical frequency (or several optical frequencies). The newly generated solitons coincide with the primary soliton in temporal domain, and share the same phase with the primary soliton, thus the process is a coherent extension of the primary soliton optical spectrum to different colors. The occurrence of the phenomenon requires appropriate dispersion condition which is not naturally satisfied in usual optical microresonators. Here, we report the experimental observation of multicolor cavity solitons using a single optical pump. As a modification to the original multicolor solitons proposal (Luo, Liang, and Lin, 2016), the multicolor solitons is generated inter-dispersion-bands, thus do not naturally share the same optical phase. The results are the first experimental demonstration of multicolor solitons in ref. (Luo, Liang, and Lin, 2016) to our knowledge.

The device used in this work is a three-coupled-ring (3CR) ultra-low-loss Si_3N_4 microresonator (Figure B.3a,b) (Yuan et al., 2023; Ji, W. Zhang, et al., 2025). The scheme of interband multicolor solitons generation is illustrated in Figure B.3a. A primary soliton (red) is firstly generated by pumping the microresonator (right ring in Fig.B.3a) with an amplified CW laser at ν_0 . The primary soliton induces Kerr parametric gain and an effective potential well due to cross-phase-modulation (XPM) at its temporal location. The secondary soliton (blue) forms with a threshold behavior, through the double balance between parametric gain and cavity loss, as well as XPM and local anomalous dispersion. An idler sideband (orange) also forms as a result of the four-wave-mixing between the primary and secondary soliton, which cannot yield a soliton due to local normal dispersion in this case.

The fact that the secondary soliton shares the same group velocity (repetition rate) is confirmed by the repetition rate measurement (Figure B.3c). One single high-signal-to-noise ratio (SNR) tone is observed via photodetection. Temporal pulse nature of the two solitons is confirmed by auto-correlation measurement (Figure B.3d,e). The primary soliton features a 688 fs full-width-half-maximum temporal duration, while that of the secondary soliton is 434 fs. High-resolution optical spectrum of the generated multicolor soliton is shown in Figure B.3f. The lines from the primary soliton is colored in red, while that of the secondary soliton (idler) is in blue (orange). As a modification to the multicolor soliton proposed in ref. (Luo,

Liang, and Lin, 2016), carrier-offset frequency of two solitons are not necessarily the same. The lower panel of Figure B.3g is a zoomed-in view of overlapping region between two solitons indicated by grey shade in the upper panel. Two sets of comb lines separated by a frequency of f_{beat} are observed. The results indicate no fixed phase relationship between the primary and secondary soliton is guaranteed.

The generation of multicolor solitons requires a specific dispersion condition. In this case, it is addressed by on-demand electrical tuning of the dispersion (Ji, W. Zhang, et al., 2025). The resonator dispersion spectrum that supports the optical spectrum in Figure B.3f is shown in Figure B.3g. Three hybrid mode families are formed, manifested by three bands in the dispersion spectrum. The primary soliton is pumped at an anomalous dispersion window ($D_{2,p}/2\pi = 374$ kHz) on the middle band near 1565 nm.

To generate the multicolor solitons (secondary soliton), firstly, phase-matching of the Cherenkov radiation is required. Here, interband phase-matching of parametric oscillation is achieved between the three dispersion bands. The parametric process involves two photons from the middle (pumped) band (whose frequency ν_p is near the cavity resonance at frequency $\nu_{p,c}$), and one photon from each of the upper and lower bands (whose frequency ν_s, ν_i is near the corresponding cavity resonance with frequency $\nu_{s,c}$ and $\nu_{i,c}$), respectively, that

$$\nu_{s,c} + \nu_{i,c} \approx 2\nu_{p,c} \quad (\text{B.1})$$

with the integrated dispersion at these modes $D_{\text{int},p}, D_{\text{int},s}, D_{\text{int},i}$ satisfying

$$D_{\text{int},s} + D_{\text{int},i} \approx 2D_{\text{int},p} \quad (\text{B.2})$$

for resonant excitation (phase matching). The phase matching frequency is indicated by the black dashed line in Figure B.3g.

The second requirement for the generation of the multicolor soliton is the group velocity matching of the primary and secondary soliton, to synchronize (and trap) the propagation of the two solitons along the resonator. Experimentally, the *FSRs* of the middle and upper band at $\nu_{p,c}$ and $\nu_{s,c}$ are measured to be near 19.86 GHz with a slight difference of ~ 1 MHz. The upper band simultaneously feature local anomalous dispersion ($D_{2,s}/2\pi = 39$ kHz), suitable for bright soliton mode locking. On the lower dispersion band, normal dispersion around the phase-matched mode does not support soliton formation, ending up in a sharp spectral peak (Cherenkov radiation).

In conclusion, the generation of multicolor cavity solitons using a single optical pump is reported in this work. With proper active inter-soliton phase-locking, the new comb source can realize coherent spectral extension from a single soliton spectrum. Moreover, the frequency spacing between the solitons falls within THz range and is tunable via differential heater tuning, which suggests potential in chip-based terahertz generation.

B.3 Observation of broadband, self-injection locked noisy microcombs near zero-GVD

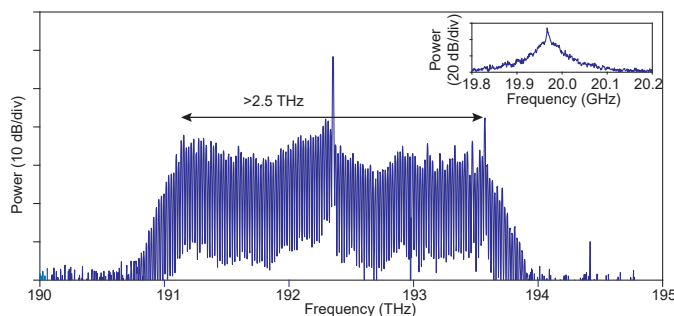


Figure B.4: **Optical spectrum of a broadband, noisy microcomb under laser self-injection locking.** The microcomb state is generated from the same 2CR device in Chapter 3. The optical spectrum spans >2.5 THz, with a noisy RF tone near 20 GHz.

During the testing of the 2CR device for near-zero-GVD microcomb generation, the same device generate an interesting microcomb state (Figure B.4). The frequency spacing between the nearby ‘comb line’ is around 20 GHz (the 2CR FSR), and is stable over time in a certain operation regime (combination of laser current and temperature). The optical coverage is more than two times larger than the coherent dark pulse microcomb generated from the same device (1 THz) (Ji, Jin, et al., 2023), when pumped by the same laser under self-injection locking. The state is believed to be an interplay between the pump DFB multi-mode lasing and Si_3N_4 resonator nonlinearity. The full mechanism is not understood, but may be related to the phenomena observed in (Galiev et al., 2018). Broadband noisy microcomb may find applications in ranging (Lukashchuk et al., 2023; Chen et al., 2023) and random number generation (Bitao Shen et al., 2023). There may also be a chance of changing the state to a coherent microcomb state with similar spectral coverage.

References

- Chen, Ruixuan et al. (2023). “Breaking the temporal and frequency congestion of LiDAR by parallel chaos.” In: *Nature Photonics* 17.4, pp. 306–314.
- Galiev, Ramzil R. et al. (2018). “Spectrum collapse, narrow linewidth, and Bogatov effect in diode lasers locked to high-Q optical microresonators.” In: *Optics Express* 26.23, pp. 30509–30522.
- Ji, Qing-Xin, Warren Jin, et al. (2023). “Engineered zero-dispersion microcombs using CMOS-ready photonics.” In: *Optica* 10.2, pp. 279–285.
- Ji, Qing-Xin, Wei Zhang, et al. (2025). “Dispersive-wave-agile optical frequency division.” In: *Nature Photonics*.
- Lukashchuk, Anton et al. (2023). “Chaotic microcomb-based parallel ranging.” In: *Nature Photonics* 17.9, pp. 814–821.
- Luo, Rui, Hanxiao Liang, and Qiang Lin (2016). “Multicolor cavity soliton.” In: *Optics Express* 24.15, pp. 16777–16787.
- Shen, Bitao et al. (2023). “Harnessing microcomb-based parallel chaos for random number generation and optical decision making.” In: *Nature Communications* 14.1, p. 4590.
- Shen, Boqiang et al. (2020). “Integrated turnkey soliton microcombs.” In: *Nature* 582.7812, pp. 365–369.
- Yuan, Zhiqian et al. (2023). “Soliton pulse pairs at multiple colours in normal dispersion microresonators.” In: *Nature Photonics* 17.11, pp. 977–983.

INDEX

Symbols

2CR, 37

2P-OFD, 16, 21, 92

C

common mode suppression, 21

E

Exceptional Point, 110

F

FP cavity, 7, 17

L

LLE, 99

O

OFD, 9

P

PDH locking, 18

S

Split-Step Fourier method, 101

SWaP, 7

STANDARDS AND MEASUREMENTS OF FREQUENCY STABILITY

B.4 Microwave phase noise

A signal with certain instability can be expressed as

$$V(t) = [V_0 + \varepsilon(t)] \sin [2\pi\nu_0 t + \phi(t)]. \quad (\text{B.3})$$

For the analysis of frequency stability, the instantaneous frequency is denoted by

$$\nu(t) = \nu_0 + \frac{d\phi(t)}{dt}, \quad (\text{B.4})$$

and thus the phase fluctuation $\phi(t)$ is mostly concerned. In the frequency domain, the phase noise is derived by

$$S_\phi(f) = |\mathcal{F}\{\phi(t)\}|^2, \quad (\text{B.5})$$

where $\mathcal{F}\{\dots\}$ denotes the Fourier transformation. This is one of the most used quantity to quantify the phase stability of a microwave signal, and the unit is usually in the log scale, dBc/Hz. Besides, if the signal is multiplied or divided electrically (which is common in electrical synthesizers), from a carrier at the frequency ν_0 to another ν_1 , the phase jitter is also modified to $\phi_1(t) = (\nu_1/\nu_0)\phi(t)$. As a result, for fair stability comparison of phase noise, the phase noise is usually “scaled” to a certain carrier frequency (e.g., 10 GHz), via

$$S_{\phi,10\text{GHz}}(f) = S_\phi(f) - 20 \times \log(\nu_0/10\text{GHz}). \quad (\text{B.6})$$

Another related quantity is the timing jitter. It is related to the phase noise via

$$\text{Jitter}(f) = \frac{S_\phi(f)}{2\pi^2\nu_0^2}, \quad (\text{B.7})$$

where the unit of the timing jitter is in s^2/Hz ; the $S_\phi(f)$ is in the single-sideband definition.

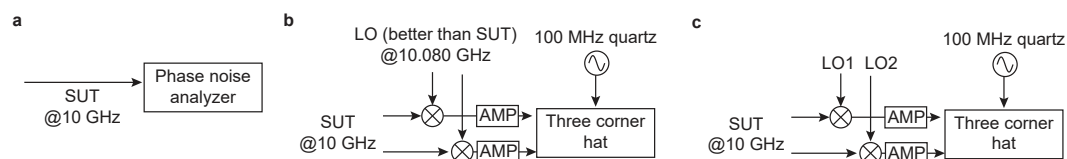


Figure B.5: Microwave phase noise measurement techniques.

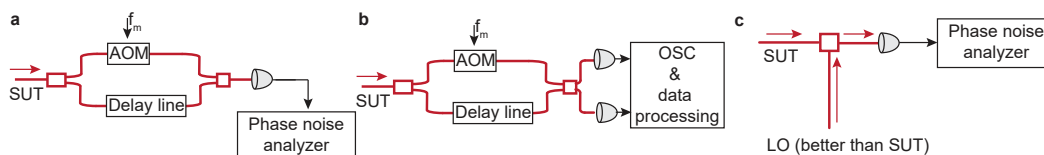


Figure B.6: **Laser noise measurement setups.**

Measurement

For the measuring of low phase noise, the easiest (but not budget-friendly) way is to use a high-performance commercial phase noise analyzer. R&S FSWP is with the highest performance for measurement floor; Keysight offer phase noise analyzer as well. For the practical setup, the signal under test (SUT, for example near 10 GHz) can be directed to the phase noise analyzer's input, as in Figure B.5a.

Another solution is by using a three-cornered hat (sometimes also called a phase meter, e.g., Microchip 53100A). The three-cornered hat has three inputs, and records the relative phases between any of the two signal inputs. If a local oscillator with better phase noise performance than the signal to be tested is present, then the setup in Figure B.5b can be used. In this setup, the local oscillator's output is split and electrically mixed with the SUT. The mixing converts the DUT's frequency to a frequency within the measurement range of the three corner hat, whose frequency is referenced to a 100 MHz quartz oscillator. And the measurement scheme excludes the influence of the extra noise from the mixer and the amplifier.

Finally, if an LO better than the SUT is not available, the measurement can be done based on the setup in Figure B.5c. Two LOs (LO1 and LO2) generates microwaves near SUT, and are mixed with the SUT. Then the common phase noise of the two down-converted signal is extracted via cross-correlation. The measurement time is determined by the worse signal source between LO1 and LO2. It is noted that collapse of the cross-correlation is possible, as in (Nelson, Hati, and Howe, 2014).

B.5 Laser short-term stability

To quantify the stability of a laser, the frequency noise is usually used, and is related to the phase noise by $S_v(f) = f^2 S_\phi(f)$.

Measurement

The easiest way to measure the laser frequency noise spectral is by using the delayed self-heterodyne method (Okoshi, Kikuchi, and Nakayama, 1980). And the method

is recently upgraded thanks to the improvements in oscilloscope and data processing with improvements in the measurement floor (caused by the photo detection process) (Yuan et al., 2022). The setup is depicted in Figure B.6a,b. Especially, the setup in Figure B.6b is optimized for measuring the fundamental linewidth at high offset frequencies.

Another method is to down-convert the laser to a microwave tone, and measuring the microwave phase/frequency noise. This can be done by beating the laser with a more stable local laser oscillator, as in Figure. B.6c. It is generally much more difficult to build the reference laser, but gives a better measurement of the laser noise at low offset frequencies.

Laser linewidth

The intrinsic (fundamental) linewidth is 2π times the the lowest value in the frequency noise plot at high-offset frequencies (usually at MHz-level). It is mostly meaningful for coherent optical communications. The integrated linewidth can be quantified in three ways:

- (1) Direct recording of the laser beatnote versus a more stable reference laser, followed by Fourier transformation.
- (2) Integrating the frequency noise trace by $\int_{\Delta\nu}^{\infty} df S_{\nu}(f)/f^2 = 1/(2\pi)$, where $\Delta\nu$ is the laser linewidth. In practice, the upper bond of the integral can be replaced by a reasonably high cutoff frequency (e.g., 1 MHz).
- (3) The β separation line (Di Domenico, Schilt, and Thomann, 2010).

In principle, all the three methods should give a similar laser linewidth (with a factor of 2 or 3).

Experimental example

Below is an example of laser frequency noise measurement as published in (Ji, Jin, et al., 2023). The measurement compares the laser frequency noise under different microcomb locking states. Frequency noise of the microcomb line is measured with a cross-correlation-based self-heterodyne measurement (Yuan et al., 2022) within the measurement time of 400 ms. Compared with the free running DFB laser (gray), frequency noise of the pump laser is reduced by 30 dB under SIL operation (blue) at 10 kHz offset frequency. An integrated linewidth $\Delta\nu$ of 7.2 kHz is obtained (by using the integral method above). The frequency noise here is still higher than the thermal noise limit given by the dashed gray curve in Fig. B.7 (Kondratiev and Gorodetsky, 2018). Finally, with the microcomb' repetition

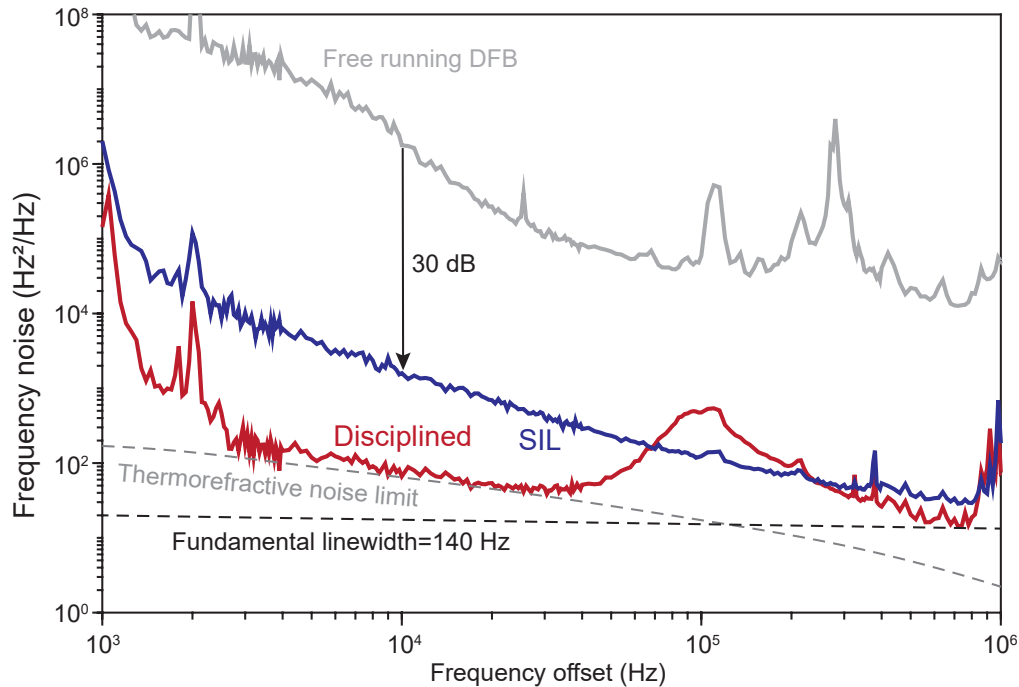


Figure B.7: **Optical frequency noise of the pump laser (comb offset frequency).** Single sideband optical frequency noise of the comb pump frequency. Grey curve gives the free-running (non SIL) measurement, blue curve is for self injection locked (SIL) operation, and the red curve is for repetition rate discipline using an external microwave reference. The thermorefractive noise floor is denoted by the dashed gray line.

rate locked, its optical offset frequency is stabilized. With the same definition as above, the calculated integrated linewidth is 2.1 kHz, which is comparable to an ECDL pumped microcomb (red line) (Lei et al., 2022). In terms of the fundamental linewidth, the dashed black line shows a floor of 20 Hz²/Hz. Thus the intrinsic linewidth is 140 Hz.

B.6 Allan deviation

The Allan deviation is the standard method to quantify the oscillators' long-term stability. Its rigorous mathematical definition can be found in (Riley and Howe, 2008). The concept begins with a repetitive measurement of a quantity x (usually the frequency) versus the real time. Briefly, the Allan deviation $\sigma_x(\tau)$, is obtained by segmenting the data into pieces with a temporal length of τ , and evaluating the mean value. Next, all the obtained mean values are used to calculate the Allan deviation “at the averaging time of τ ”. Finally, by alternating the averaging time τ (usually on a log scale), a trace of $\sigma_x(\tau)$ versus τ can be obtained.

Measurement techniques

Nowadays, the commercial phase noise analyzer and three corner hat offer functions to directly read the Allan deviation. The setup is similar to those in Figure B.5, B.6c. However, the raw frequency data is not available, thus adding ambiguity to the result.

A more tradition (and sometimes reliable) way is to use a frequency counter. In practice, the microwave tone is amplified to >0 dBm, electrically filtered to reject the harmonics, and directed to the frequency counter. The sampling rate of the counter should be properly set, such that the accumulated dead time does not influence the measurement result. This can be confirmed by changing the sampling rate and see if the final Allan deviation agrees between measurements. The technical challenge of this method is the availability of the referencing local oscillator. A signal source with better stability than the SUT is always required.

Experimental example

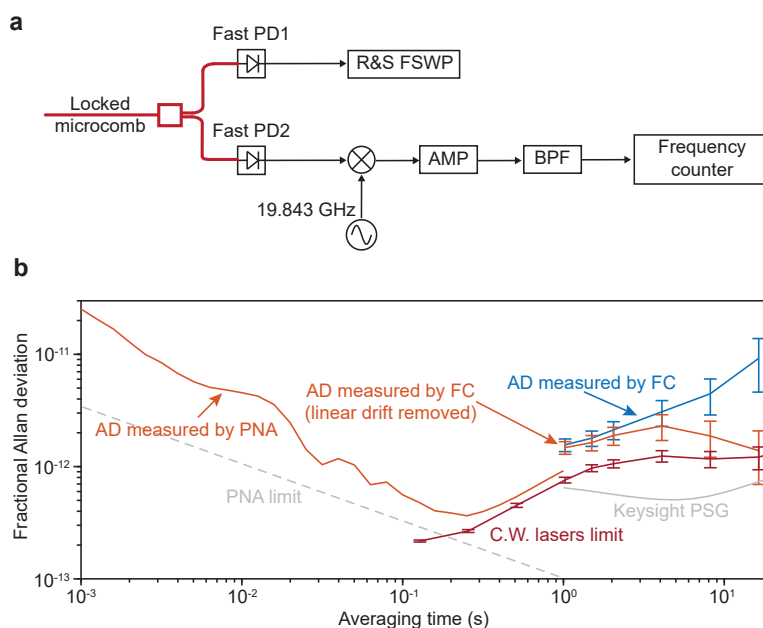


Figure B.8: **Allan deviation measurement.** **a**, Experimental setup. **b**, Summary of the Allan deviation measurement results. Data are presented as mean values, and the error bar denotes standard deviation where the sample number is 6096, 6096 and 1200 for the blue, orange and red traces, respectively.

Here the details of Allan deviation measurement of the results published in (Ji, Zhang, et al., 2025) is presented as an example. In the measurement, the output of the microcomb (after EDFA amplification) is split and detected by two different fast

photodetectors (Figure B.8a). The output of photodetector PD1 (U2T XPDV2320R) is analyzed by an R&S FSWP phase noise analyzer (PNA), which features a low noise floor (dashed gray line in Figure B.8b). This measurement involves performing a cross-correlation in the PNA. The output of PD2 (Thorlabs DXM30AF) is directed to a frequency mixer for down conversion to a 30 MHz tone using a Keysight PSG E8257N as the local reference oscillator. This signal is amplified, filtered by a 27-33 MHz bandpass filter, and sent to a frequency counter (Tektronix FCA3120) whose input signal frequency is <300 MHz. This measurement method is faster than the PNA cross correlation, despite being limited by the noise floor of the Keysight PSG (plotted as the solid gray line in Figure B.8b).

The Allan deviation data presented in Figure 4c in the main text is a combination of the results using the two methods. Specifically, for averaging time <1 s, the Allan deviation of the Keysight PSG is higher than the 2P-OFD stabilized microcomb, and the measurement time of the low-noise PNA is reasonably fast, so Allan deviation is computed using the PNA (red trace in Figure B.8b). On the other hand, for averaging time >1 s the cross correlation time of the PNA is too long. Also, the Allan deviation of the microcomb (as measured by the counter method) is larger than the Keysight PSG, so the Allan deviation for this range of averaging times is measured using the frequency counter. The red trace with error bar in Figure B.8b (error bar is the standard deviation when calculating the Allan deviation) is adjusted in Figure 4c in the main text to remove a linear drift of 0.013 Hz/s. Without the linear drift removal, the Allan deviation is the blue trace in Figure B.8b.

The lower limit of the Allan deviation for longer averaging times is attributed to the two C.W. lasers, which serve as the reference in the 2P-OFD. The inferred noise limit from the two C.W. lasers is plotted as the dark red curve in Figure B.8b. This curve is generated by locking the two C.W. lasers to the FP cavity with frequency separation by one FP cavity FSR (4 GHz), followed by measurement of the Allan deviation of the resulting laser beatnote. In the plot, the Allan deviation is divided by the 2P-OFD frequency span (2 THz) to infer its impact on the microcomb repetition rate under 2P-OFD. This noise limit can possibly be reduced by improvements to system shielding and packaging of the FP cavity subsystem.

References

Di Domenico, Gianni, Stéphane Schilt, and Pierre Thomann (2010). “Simple approach to the relation between laser frequency noise and laser line shape.” In: *Applied Optics* 49.25, pp. 4801–4807.

- Ji, Qing-Xin, Warren Jin, et al. (2023). “Engineered zero-dispersion microcombs using CMOS-ready photonics.” In: *Optica* 10.2, pp. 279–285.
- Ji, Qing-Xin, Wei Zhang, et al. (2025). “Dispersive-wave-agile optical frequency division.” In: *Nature Photonics*.
- Kondratiev, Nikita M. and Mikhail L. Gorodetsky (2018). “Thermorefractive noise in whispering gallery mode microresonators: Analytical results and numerical simulation.” In: *Physics Letters A* 382.33, pp. 2265–2268.
- Lei, Fuchuan et al. (2022). “Optical linewidth of soliton microcombs.” In: *Nature Communications* 13.1, p. 3161.
- Nelson, Craig W., Archita Hati, and David A. Howe (2014). “A collapse of the cross-spectral function in phase noise metrology.” In: *Review of Scientific Instruments* 85.2.
- Okoshi, Takanori, Kazuro Kikuchi, and Akira Nakayama (1980). “Novel method for high resolution measurement of laser output spectrum.” In: *Electronics letters* 16.16, pp. 630–631.
- Riley, William J. and David A. Howe (2008). *Handbook of frequency stability analysis*. Vol. 1065. US Department of Commerce, National Institute of Standards and Technology.
- Yuan, Zhiquan et al. (2022). “Correlated self-heterodyne method for ultra-low-noise laser linewidth measurements.” In: *Optics Express* 30.14, pp. 25147–25161.